62 72111 Copy 588

~~CONFIDENTIAL~~ NASA TM X-287

NASA TM X-287

Declass - CCN - 12/13

TECHNICAL MEMORANDUM
X-287

Hard copy (HC) $3.00
Microfiche (MF) .75

THEORETICAL STABILITY DERIVATIVES FOR THE X-15 RESEARCH AIRPLANE AT SUPERSONIC AND HYPERSONIC SPEEDS INCLUDING A COMPARISON WITH WIND-TUNNEL RESULTS

By Harold J. Walker and Chester H. Wolowicz

Flight Research Center
Edwards, Calif.

DECLASSIFIED: Effective 2-5-65
Authority: F.G. Drobka (ATSS-A)
memo dated 3-25-65: AFSDC-5197

DECLASSIFIED BY AUTHORITY OF NASA
CLASSIFICATION CHANGE NOTICES NO. 14
DATED 4-21-65 ITEM NO. 5

GROUP 4
Downgraded at 3 year intervals; declassified after 12 years

CLASSIFIED DOCUMENT - TITLE UNCLASSIFIED

This material contains information affecting the national defense of the United States within the meaning of the espionage laws, Title 18, U.S.C., Secs. 793 and 794, the transmission or revelation of which in any manner to an unauthorized person is prohibited by law.

NATIONAL AERONAUTICS AND SPACE ADMINISTRATION
WASHINGTON

August 1960

N65-24060 (ACCESSION NUMBER)
116 (PAGES)
1 (THRU)
01 (CODE)
FACILITY FORM 602

1T

DECLASSIFIED

TABLE OF CONTENTS

DECLASSIFIED BY AUTHORITY OF NASA CLASSIFICATION CHANGE NOTICES NO. 44 DATED 4-22-65 ITEM NO. 5

H 1 4 6

0176284

H
1
4
6

DECLASSIFIED

NATIONAL AERONAUTICS AND SPACE ADMINISTRATION

TECHNICAL MEMORANDUM X-287

THEORETICAL STABILITY DERIVATIVES FOR THE X-15 RESEARCH AIRPLANE AT SUPERSONIC AND HYPERSONIC SPEEDS INCLUDING A COMPARISON WITH WIND-TUNNEL RESULTS*

By Harold J. Walker and Chester H. Wolowicz

H
1
4
6

SUMMARY

24060 over

The stability and control derivatives for the X-15 research airplane in power-off flight at supersonic and hypersonic Mach numbers are presented, both as derived from existing theoretical methods and as measured in various wind-tunnel facilities. Calculations are made for Mach numbers within and beyond the estimated flight envelope and for angles of attack from 0° to 25°. The results are compared with experimental data in the Mach number range from 2 to approximately 7 and, for the static derivatives, with the limiting values given by Newtonian theory.

In general, good approximations of the longitudinal and lateral-directional derivatives are obtained when careful attention is given to the shock- and vortex-interference effects between the various airplane components and to the increasing nonlinearity of the aerodynamic coefficients as hypersonic speeds are approached. The characteristics of the lifting surfaces are calculated by the modified hypersonic small-disturbance theory proposed by Van Dyke, and those for the fuselage, by the second-order shock-expansion method. The results of these methods are subsequently employed in conjunction with slender-body and linear theory for calculation of the static and rotary derivatives. The lateral-directional derivatives, although limited to small sideslip angles, are determined for combined sideslip and angle of attack.

The results of the analysis indicate that the X-15 airplane is statically stable in pitch and yaw to Mach numbers well in excess of its design limits, and that the degree of stability increases substantially with increasing angle of attack at hypersonic speeds. The dihedral effect at these speeds, on the other hand, exhibits an unstable trend, and thus indicates a possible dynamic instability at high angles of attack. The calculated longitudinal characteristics are for the most

*Title, Unclassified.

[redacted]

part in close accord with the results from wind-tunnel tests. The lateral and directional characteristics agree well with wind-tunnel data in the lower angle-of-attack range; however, due to an interference of the bow shock wave on the lower vertical tail and other effects not accounted for in the theory, some disagreement is found at high angles of attack.

The results from simple Newtonian theory in general are substantially lower than the trends indicated by the hypersonic small-disturbance and shock-expansion methods.

H
1
4
6

INTRODUCTION

An adequate and reliable ground simulation of the flight characteristics of hypersonic aircraft, in view of the wide range of flight conditions encountered throughout a typical design mission, necessitates a rather comprehensive determination of the aerodynamic characteristics of such vehicles in the early design stages. Wind-tunnel and ballistic-range facilities normally provide the bulk of this information; however, theoretical methods are also employed as a rational basis for design of the vehicle and as a means for extrapolating the known characteristics to untested and unexplored regions. Thus, each complements the other as a new vehicle configuration proceeds from the initial design to the final flight stage.

The X-15 research airplane has been extensively tested in various NASA and other wind-tunnel facilities, employing models which in many cases are nearly exact replicas of the final design configuration (refs. 1 to 4). A substantial amount of derivative data therefore has been assimilated which encompasses most of the overall flight envelope proposed for the X-15 research program. Although the derivative coverage is fairly comprehensive in the subsonic and lower supersonic speed ranges, it is incomplete above a Mach number of 3.5 and does not extend beyond the performance limit estimated to be in the vicinity of 6.5. Theoretical methods, therefore, may be applied to fill the remaining gaps and to extrapolate the present results to Mach numbers beyond 6.5 in order that the characteristics of a vehicle of this type may be studied in an extended speed range. This paper is undertaken to supply, in part, this needed information through application of various available methods of analyses, and to assess the accuracies and limitations of the methods by comparison with the available experimental data.

A brief description of the airplane is given in the following section, and a list of symbols used throughout the analyses is presented in the appendix.

DESCRIPTION OF THE AIRPLANE

The X-15 airplane is a rocket-propelled midwing configuration, employing low-aspect-ratio 5-percent-thick wing and horizontal-tail surfaces as illustrated in figure 1. The horizontal tail is swept back and, in order to provide sufficient clearance from the wing wake at low angles of attack, is mounted at a dihedral angle of -15°. To ensure adequate directional stability throughout the flight envelope, large upper and lower vertical tails with 10° wedge sections are incorporated. The control portion of the lower panel is jettisonable to provide ground clearance during landing. The fuselage is composed of large integral fuel and liquid-oxygen tanks in the midsections which necessitate the addition of external triangular-shaped side fairings to house the various control systems.

Aerodynamic control in pitch and roll is obtained through symmetric and differential variations of the tailplane incidence, and in yaw by rotation of the outboard panels of the upper and lower vertical surfaces. For maneuvering in regions of low dynamic pressure, jet reaction controls are installed in the nose of the fuselage for pitch and yaw control and near both wing tips for roll control.

Table I outlines the geometric characteristics of the airplane.

SCOPE OF THE INVESTIGATION

The airplane disturbances in general are assumed to be small, therefore the longitudinal and lateral-directional modes may be treated independently. In the following presentation the various derivatives are grouped under the two general categories of longitudinal or lateral-directional derivatives. These categories, in turn, are further subdivided into static, rotary, and control derivatives. Calculated results are presented for each derivative, followed by a brief discussion of the significance and accuracy of the results. A rigid airframe is assumed throughout the analysis, and ranges of Mach number from 2 to 12 and angle of attack from 0° to 25° are considered.

The analysis is restricted to power-off flight. Power effects are not necessarily negligible, however, particularly under conditions where the jet exhaust is highly underexpanded and extensive pluming may occur. Some possible effects of jet pluming on airplane stability and control are considered in references 5 and 6.

Results of extensive wind-tunnel tests made with scale models of the X-15 provide the best available criteria for judging the accuracy of

[redacted]

the theoretical methods employed. Comparisons therefore are made in each case with data derived from the following sources:

Mach number	Facility	Reference
1.41 to 2.01	Langley 4- by 4-foot supersonic pressure tunnel	1
1.55 to 3.50	Ames Unitary Plan tunnel	2
2.29 to 4.65	Langley Unitary Plan tunnel	3
6.86	Langley 11-inch hypersonic tunnel	1, 4

Wind-tunnel data for Mach numbers greater than approximately 7 are not available at present. Table II presents details of the models, which in all cases were nearly exact replicas of the final design configuration.

DISCUSSION OF FLOW FIELDS

In the following analysis, frequent reference is made to various interference effects arising from the shock waves and flow fields generated by the various airplane components. Since the airplane stability and controllability are in general markedly affected, a brief introductory description of these effects preceding the detailed derivative analysis will, it is believed, permit a clearer and more orderly presentation. More extensive treatments may be found in references 7 to 11.

Interference at high Mach numbers may arise from a number of sources, among which are the fuselage bow wave (including the canopy and side-fairing shocks), the shock compression and expansion fields from the wing and tail surfaces, the downwash and sidewash induced by the wing, and from the vortices generated by the fuselage. These interference fields are illustrated in sketches (a) and (b) presented on the following page. The shock waves that occur at a Mach number of 6 are also illustrated in figure 2 in the form of shadowgraphs of a small free-flight model tested at the NASA Ames Research Center.

H
1
4
6

[redacted]

DECLASSIFIED

H
1
4
6

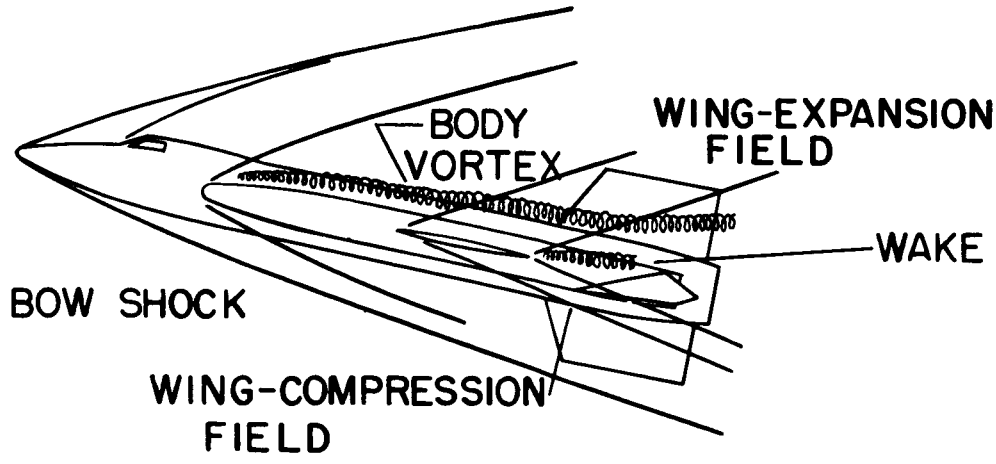

Side view

Sketch (a).

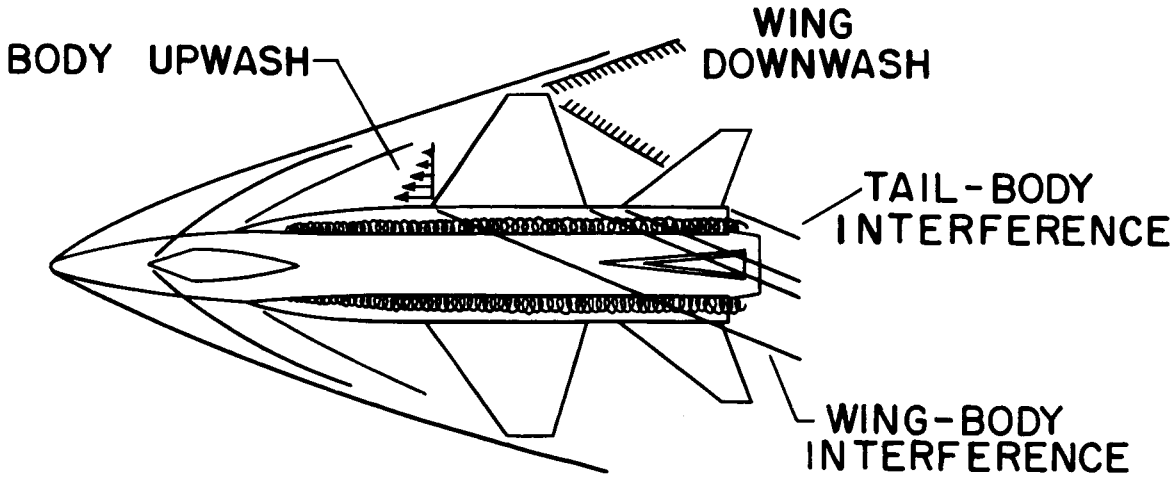

Plan view

Sketch (b).

[redacted]

The order of magnitude of the dynamic-pressure loss from the X-15 bow shock is given in figure 3 in terms of the ratio of downstream to free-stream dynamic pressure. The results shown were calculated with the aid of Schlieren photographs of the bow-wave angles from reference 5 and the shock tables in reference 12, assuming the downstream flow after passage through the shock wave to expand isentropically until the static pressure again reaches the free-stream value. The local Mach number at this point, however, is less than the free-stream value, hence the lift-curve slopes of the downstream surfaces are increased. This increase tends to compensate in part for the loss in dynamic pressure as shown also in figure 3 by the ratio of the product of dynamic pressure and lift-curve slope in the downstream and free-stream regions. This ratio, designated as Q, is applied hereafter as a correction factor for the lifting effectiveness of the tail surfaces at low angles of attack. The bow wave, it is observed, crosses the wing at the higher Mach numbers such that some portions of the wing lie in the region of essentially unexpanded flow immediately behind the shock, as well as in the highly expanded flow at the fuselage juncture. In the vicinity of the shock wave the product $\bar{q}_1\left(C_{L_\alpha}\right)_1$ is considerably greater than the free-stream value, whereas near the body it is less than this value. As a result, the factor Q for the wing varies between values greater and less than unity. The average value is assumed to be unity.

The wing, as shown in the foregoing sketches, generates shock compression and expansion fields which give rise to pronounced changes in local Mach number, dynamic pressure, and downwash, all of which may alter substantially the characteristics of the tail surfaces. The interference of these fields with the horizontal tail is largely avoided on the X-15 by locating the tail surface near the extended wing plane but with sufficient dihedral angle to clear the wake at low angles of attack. Large incidence settings of the horizontal tail, however, will place some sections of the tail within the bounds of these shock fields, and the stabilizer effectiveness will be correspondingly altered depending upon incidence angle, angle of attack, and Mach number (ref. 10). The vertical tails are similarly affected by the changes in local dynamic pressure and Mach number due to both compression from the lower wing surface and expansion from the upper surface. As shown in a subsequent section, these effects are of prime importance in evaluating the directional- and lateral-stability characteristics at high Mach numbers.

Immediately downstream of the wing trailing edge a small region of upwash may be expected at high Mach numbers as a result of the expansion of the flow field from the lower wing surface (refs. 8 and 13). Depending upon Mach number, angle of attack, wing thickness, and proximity of the tail, this local upwash could exert a noticeable effect on the lift of the horizontal tail. In the present application, the large sweep of the tail in relation to the wing and the extreme slenderness of the wing and stabilizer profiles minimize these effects, and significant upwash effects are expected only at high angles of attack in the high Mach number range.

[redacted]

In a lifting attitude, the fuselage generates vortices along its length, similar to those shown in the sketches, which eventually merge into a pair of separated vortex filaments offset from the surface of the fuselage. As pointed out in references 10 and 14, these vortices often induce sizable downwash and sidewash in the region of the tail, depending upon angle of attack and the location of the tail surfaces. Although the point of separation from the body moves toward the nose with increasing angle of attack, the criteria of references 10, 11, and 15 indicate that for low angles of attack this separation point on the X-15 should occur just upstream from the wing leading edges. Shortly thereafter the vortices enter the expansion field from the wing and are bent in the direction of local flow. It is believed, therefore, that the departure of the vortices from the fuselage is well below the tip of the vertical tail at moderate angles of attack (below 15°). With the horizontal tail located in a relatively low position in the positive angle-of-attack range and with the vertical surfaces close to the wing, small departures will exert relatively little influence on either the longitudinal or lateral-directional stability of the X-15. At high angles of attack the effectiveness of the upper vertical tail is so reduced by the wing-expansion field and the horizontal tail so far removed that vortex interference again becomes a negligible factor. A more complete description of this effect is given in a later section. The effects of the body vortices, therefore, are disregarded in the present analysis.

Wing-vortex interference is confined essentially to the regions inside the downstream Mach cones from the tips, the wing leading edges being supersonic in the range of Mach numbers considered. Because of the relative proximity of the wing and horizontal tail, these tip cones for Mach numbers greater than about 4 intercept only minor regions of the horizontal tail near the tips, and hence may be neglected. Below a Mach number of 4, their effect on the local downwash angle at the tail should be taken into account.

Sketches (a) and (b) also indicate regions of mutual interference between adjacent components of the airplane, such as those of lift carryover from the wing and tail surfaces onto the fuselage, and of body-induced upwash across the wing span. The description of these effects is deferred to the subsequent sections.

PRESENTATION OF RESULTS

The longitudinal derivatives are referred to the stability axes shown in figure 4(a) and are presented in the next section in the following order:

[redacted]

The body-axis system in figure 4(b) is used for the lateral-directional derivatives which are presented as follows:

H
1
4
6

ANALYSIS AND DISCUSSION OF LONGITUDINAL DERIVATIVES

The following section presents an analysis and discussion of the lift, pitching moment, longitudinal control, and pitch-damping characteristics both as derived from theory and as measured in the wind-tunnel tests previously described.

Lift Characteristics

The lift for the complete airplane is calculated by the method of reference 16, in which the total lift is considered initially to be the sum of the individual lifts of the exposed wing and horizontal-tail surfaces and of the fuselage, each treated as an isolated body. Incremental lifts are then added which represent corrections for the interferences that arise when the components are placed adjacent to one another in the overall configuration. The interference is reciprocal, consisting of reflection-plane and upwash effects on the wing due to the presence of the fuselage, and of the carryover lift on the fuselage due to the exposed wing and tail panels. Both effects, however, are treated as wing contributions in accordance with the method of reference 16. The forces on the horizontal-tail surfaces at zero incidence (controls fixed) are similarly derived. The method in general has been confirmed experimentally for low and moderate angles of attack at supersonic Mach numbers, but its validity in the hypersonic range has not yet been established. Extension of the method to angles of attack greater than the range of the present study is considered in reference 17.

[redacted]

DECLASSIFIED

The procedure of reference 16 when applied to the X-15 configuration leads to the following relationship for airplane lift coefficient

$$C_L = \frac{S_W}{S} C'_{L_W}\left(K_{WB} + K_{BW}\right) + Q \frac{S_T \cos \Gamma_T}{S} C'_{L_T}\left(K_{TB} + K_{BT}\right)\left(1 - \frac{d\epsilon}{d\alpha}\right) + C_{L_B} \tag{1}$$

The K terms are the interference factors which account for the lift of the wing and the horizontal tail in the presence of the body, K_{WB} and K_{TB}, and for the lift of the body in the presence of the wing and the horizontal tail, K_{BW} and K_{BT}. The characteristics of the individual components are discussed further in the following sections.

Wing.- The flight envelope for the X-15 extends through the transitional range from supersonic to hypersonic speeds, hence a method of calculation suitable to both regimes is desired. The unified supersonic-hypersonic small-disturbance theory proposed by Van Dyke in reference 18 for slender configurations appears to fulfill this need. According to this method, the relationships developed for hypersonic flow about slender shapes in terms of the hypersonic similarity parameter (Mach number × flow-deflection angle) are found to be valid also in the realm of supersonic linear theory if the parameter is simply redefined as $\sqrt{M^2 - 1} \times$ flow-deflection angle. This modification is also discussed in reference 19. For determination of the wing lift characteristics in the present analysis, the small-disturbance pressure coefficients given in reference 20 for compression and expansion are employed but with the similarity parameter modified as stated previously. These coefficients, when compared with the results of shock-expansion theory, are shown in reference 21 in the unmodified form to yield accurate estimates of two-dimensional airfoil lift coefficients at hypersonic speeds for angles of attack up to 25°. When applied to an inclined flat plate, as the wing and tail surfaces are assumed to be in the present analysis, the following result is obtained for the two-dimensional case

$$c_n = (C_p)_{lower} - (C_p)_{upper}$$

$$= \alpha^2 \left\{ \frac{\gamma + 1}{2} + \sqrt{\left(\frac{\gamma + 1}{2}\right)^2 + \frac{4}{H^2}} - \frac{2}{\gamma H^2}\left[\left(1 - \frac{\gamma - 1}{2} H\right)^{\frac{2\gamma}{\gamma - 1}} - 1\right] \right\} \tag{2}$$

where H is the similarity parameter $\left(\sqrt{M^2 - 1}\right)\alpha$. The slope c_{n_α} given by this expression, as α goes to zero, is found to reduce to the familiar

result, $\frac{4}{\sqrt{M^2 - 1}}$, given by linear theory. Although the initial slope is identical to that given by linear theory, the variation of c_n with angle of attack becomes increasingly nonlinear as Mach number is extended to the hypersonic range. This progressive change is illustrated in figure 5 in which γ is assumed to be 1.4. The variation for the limiting case of infinite Mach number reduces to the parabola $c_n = (\gamma + 1)\alpha^2$. The results given by simple Newtonian theory are also included for comparison. It is observed that equation (2) reduces to the Newtonian result when $M \to \infty$ and $\gamma \to 1$; that is, $c_n = 2\alpha^2$. Deviations of γ from the value of 1.4 assumed in the present analysis, however, are believed on the basis of the results of references 12 and 19 to be small.

As a means for conversion from two-dimensional to three-dimensional lift at hypersonic speeds, the following approximation for wing-tip effects, based on linear theory, may be applied

$$C'_N = \frac{C'_{L_\alpha}}{\frac{4}{\sqrt{M^2 - 1}}} c_n \tag{3}$$

In this expression C'_{L_α} is the lift-curve slope from linear theory for the three-dimensional plan form, as given, for example, in reference 22, and c_n is given by equation (2). The lift coefficient for the isolated wing, neglecting the small chordwise forces due to skin friction and wave drag, therefore becomes

$$C'_{L_W} = C'_N \cos \alpha \tag{4}$$

and that for the wing in the presence of the body (based on area S),

$$C_{L_W} = \left(K_{WB} + K_{BW}\right) \frac{C'_{L_\alpha}}{\frac{4}{\sqrt{M^2 - 1}}} c_n \frac{S_W}{S} \cos \alpha \tag{5}$$

Approximate values for the interference terms K_{WB} and K_{BW} in equation (5) are given in reference 16. The lift characteristics predicted by this equation for the X-15 wing are shown in figure 6(a). The Newtonian limit (that is, $M = \infty$, $\gamma = 1$), for which $K_{WB} \to 1$ and $K_{BW} \to 0$, is seen

DECLASSIFIED

to be substantially lower than results given by the hypersonic small-disturbance theory, largely because of the difference in γ.

Horizontal tail.- The lift characteristics of the horizontal tail at zero incidence are calculated by the same procedures described for the wing, but with additional modifications included for dihedral angle (see ref. 23). The fuselage-induced upwash at the tail plane, however, is considered to be negligible due to the proximity of the wing, and the term K_{TB}, corresponding to K_{WB} in equation (5), is therefore unity. The wing downwash parameter $d\epsilon/d\alpha$, as estimated from the charts of reference 24, is found to be negligible beyond a Mach number of approximately 4. The lift curves for the horizontal tail, based on the reference area S and corrected for the dynamic-pressure loss Q from figure 3, are shown in figure 6(b) together with the Newtonian limit.

Fuselage.- Lift from the fuselage as described in reference 25 is derived from both inviscid flow about the body and from viscous cross-flow separation. For the present case the inviscid lift is believed to be better approximated in the overall Mach number range by the second-order shock-expansion theory presented in reference 26, rather than by the slender-body potential theory employed in reference 25.[1] The method of reference 26 is an extension of the generalized shock-expansion method of reference 27 for bodies of revolution at small angles of attack and is believed applicable for Mach numbers intermediate between those of the potential and generalized shock-expansion theories. For application to the noncircular cross sections of the X-15, the results from reference 26 have been multiplied by a factor equal to the ratio of the actual plan-form area to that of an equivalent body of revolution having the same local cross-sectional areas as the present configuration. This approximation for the inviscid effects (neglecting chordwise forces) leads to the relationship

$$\left(C_{L_B}\right)_{\text{inviscid}} = R_\alpha \frac{S_B}{S}\left(C'_{N_\alpha}\right)_B \alpha \cos \alpha \qquad (6)$$

in which $\left(C'_{N_\alpha}\right)_B$ is obtained from reference 26 (appendix C) and

$$R_\alpha = \frac{\text{Total fuselage plan-form area}}{\text{Plan-form area of equivalent body of revolution}}$$

The slopes given by the second-order shock-expansion theory, although derived for vanishingly small angles of attack (streamlines approximately

---

[1]The unified supersonic-hypersonic small-disturbance method described in the preceding section has not yet been extended to slender bodies at an angle of attack in axial flow.

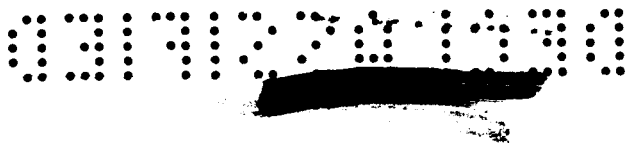

parallel to the body meridian lines), have been extended through the overall angle-of-attack range. References 28 and 29 show that, for slender bodies having elliptic cross sections, the ratio of potential lift for the elliptic body to that for an equivalent circular body is equal to the ratio of major to minor axes. This criterion would lead to values of $\left(C_{L_B}\right)_{\text{inviscid}}$ somewhat higher than those given by equation (6).

The lift due to viscous crossflow is given by the following relationship from reference 30

$$\left(C_{L_B}\right)_{\text{viscous}} = \eta \bar{c}_{d_c} \frac{A_\alpha}{S} \alpha^2 \cos \alpha \qquad (7)$$

The term A_α, the plan-form area of the fuselage, consists in the present case of the forebody area only (vertex to wing leading edge approximately), since the wing and tail, in effect, block the crossflow over the remaining sections. The term η is a correction factor for body-fineness ratio as discussed in reference 30, and $\bar{c}_{d_c}$ is an average crossflow drag coefficient. The latter should be estimated by the procedure suggested in the appendix of reference 31 using the experimental section drag coefficients given in references 30 and 32 to 34. For simplicity in the present analysis, $\bar{c}_{d_c}$ has been assumed to be constant at 1.2 in the overall Mach number and angle-of-attack ranges. Although confirmed experimentally for Mach numbers up to approximately 4 (ref. 29), the validity of the preceding method for hypersonic flows in general has not been established.

Newtonian theory has been applied in a simple, approximate manner by assuming that the X-15 fuselage may be represented from the vertex to a station immediately rearward of the canopy by a circular cone and over the remaining length by a cylinder of constant diamond-shaped cross section similar to that of the combined fuselage and side fairings. The relationships given in reference 13 then lead to the following expression for fuselage lift coefficient

$$C_{L_B} = \left(\frac{S_{NC}}{S} \cos^2 \tau_{NC} \sin 2\alpha + \frac{S_{AB}}{S} 2 \cos^2 \nu \sin^2 \alpha \right) \cos \alpha \qquad (8)$$

The results given by equations (6) to (8) are presented in figure 6(c).

Airplane.- The combined results from equations (1) to (8), representing the lift characteristics for the complete airplane (untrimmed),

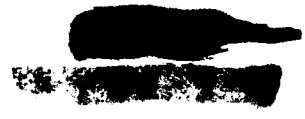

are shown in figure 7 for the Mach number range from 2 to 12 and for the Newtonian limit. The component buildup is further illustrated in figure 8, showing the effect of Mach number on lift-curve slope at several angles of attack. These figures are seen to reflect the increasing nonlinearity which characterizes the transition from supersonic to hypersonic Mach numbers. Thus the lift-curve slope at high angles of attack is seen in figure 8 to diminish relatively little with increasing Mach number as compared to the familiar losses associated with small angles.

The calculated results are compared with wind-tunnel data from references 1 to 3 in figures 9 and 10 for several Mach numbers from 2.01 to 6.86 and for angles of attack from 0° to 25°. Although the wind-tunnel results appear to be slightly underestimated, the general agreement is good. Some of the apparent discrepancy is due to an irregular variation of the zero-lift intercepts among the various data. The Newtonian limits shown in figure 10, due to the absence of the various interference effects among the components and the reduced value of γ, are considerably lower than the trends indicated by the other methods.

Pitching-Moment Characteristics

The pitching-moment characteristics for the airplane are readily determined from the values of lift coefficient presented in figures 6 to 8 and the center-of-pressure charts given in reference 16. The buildup of the moments due to the various components about a center-of-gravity location at 20 percent of the mean aerodynamic chord (based on area S) proceeds as follows:

Wing and horizontal tail.- The moment arm for the lift of the wing in the presence of the body differs in general from that for the lift induced by the wing on the body, with the difference depending primarily on Mach number and fuselage diameter. The moments from the two sources therefore must be determined separately; however, for consistency with the foregoing lift calculations both effects are charged to the wing. The characteristics for the horizontal tail (at zero incidence) are determined in like manner, although the moment arms for the various interference effects, due to the absence of fuselage afterbody, are essentially equal. The following expression for the combined wing and tail in the presence of the fuselage is obtained

$$C_{m_W} + C_{m_T} = \frac{S_W}{S} C_{L_W}\left(K_{WB}\frac{\bar{x}_{WB}}{\bar{c}} + K_{BW}\frac{\bar{x}_{BW}}{\bar{c}}\right) + Q\frac{S_T \cos \Gamma_T}{S} C_{L_T}\left(1 - \frac{d\epsilon}{d\alpha}\right)\left(K_{TB} + K_{BT}\right)\frac{\bar{x}_T}{\bar{c}} \qquad (9)$$

[redacted]

The results given by this equation are presented in figures 11(a) and 11(b) together with the Newtonian limits.

Fuselage.- The center of pressure for the lift due to inviscid flow about the fuselage is calculated by the second-order shock-expansion method presented in appendix C of reference 26, and that due to viscous crossflow, by the procedure described in the appendix of reference 31. The former is found to vary slightly with Mach number and the latter to be essentially constant. The moment coefficient for the fuselage may be expressed as

$$C_{m_B} = \left(C_{L_B} \frac{\bar{x}_B}{\bar{c}}\right)_{\text{inviscid}} + \left(C_{L_B} \frac{\bar{x}_B}{\bar{c}}\right)_{\text{viscous}} \qquad (10)$$

H 1 4 6

and, as shown in figure 11(c), is destabilizing.

Airplane.- Figures 12 and 13 present the stability characteristics for both the tail-on (zero incidence) and tail-off configurations as calculated from equations (9) and (10). The gradual departure from linearity as Mach number is increased from supersonic to hypersonic levels is again evident in these figures. At high angles of attack the stability, like the airplane lift coefficient, declines relatively little with increasing Mach number. These trends are also apparent in the buildup presented in figure 14 for several angles of attack. Newtonian theory, since it underestimates the lift of the wing and horizontal tail (fig. 7), also underestimates the stability as shown in figures 12 and 13.

Figure 9 shows that the theoretical methods are generally in close accord with the experimental data, although the stability contribution from the horizontal tail at a Mach number of 6.86 (fig. 9(e)), appears to be underestimated to some extent. The discrepancy is a possible consequence of the upwash in the expanding flow downstream from the wing trailing edge as described in references 8 and 13 - an effect which has been neglected in the present analyses. Also shown in figure 9 are the lift curves for trimmed level flight based on the foregoing calculated pitching-moment characteristics.

Further comparisons between experiment and theory are presented in figures 15 and 16. These figures indicate that static stability at small positive angles of attack will not become marginal until Mach numbers well in excess of the design limit are reached. As noted previously, the Newtonian limits in figure 15 differ substantially from the apparent trends of the hypersonic small-disturbance and shock-expansion methods.

DECLASSIFIED

Longitudinal-Control Characteristics

The methods of reference 16 enable rapid estimates to be made of the lift variations due to incidence as well as angle of attack for wing-body combinations. When applied to the X-15 stabilizer, the following relationships are obtained for the lift and moment increments due to a change of incidence angle (α = Constant)

$$\Delta C_{L_T} = Q \frac{S_T \cos \Gamma_T}{S}\left(k_{TB} + k_{BT}\right)\Delta C'_{N_T} \cos\left(\alpha + i_T\right) \tag{11}$$

$$\Delta C_{m_T} = Q \frac{S_T \cos \Gamma_T}{S}\left(k_{TB} + k_{BT}\right)\frac{\bar{x}_T}{\bar{c}}\Delta C'_{N_T} \cos i_T \tag{12}$$

The term $\Delta C'_{N_T}$, because of the nonlinear character of the flow, should be determined with the aid of equations (2) and (3) for the combined angles of attack and incidence as measured in a plane perpendicular to the surface. If subscript P is used to designate angles measured in the plane perpendicular to the plane of the tail,[2] then the normal-force increment due to incidence is

$$\Delta C'_{N_T} = \left(C'_N\right)_{\left(\alpha+i_T\right)_P} - \left(C'_N\right)_{\alpha_P} \tag{13}$$

in which

$$\left.\begin{aligned} \left(\alpha + i_T\right)_P &= \tan^{-1}\left[\tan\left(\alpha + i_T\right)\cos \Gamma_T\right] \\ \alpha_P &= \tan^{-1}\left(\tan \alpha \cos \Gamma_T\right) \end{aligned}\right\} \tag{14}$$

The factors k_{TB} and k_{BT} account for the mutual interference between the stabilizer and fuselage for incidence variations in a manner analogous to K_{TB} and K_{BT} for angle-of-attack variations. In trimmed flight, however, α and i_T are normally of opposite sign and the magnitude of the combined angle $\alpha + i_T$ is generally small. Assuming that the terms $\cos\left(\alpha + i_T\right)$ and $\cos i_T$ in equations (11) and (12) are unity and that

---

[2]The incidence of the X-15 stabilizer actually is varied by rotation about an axis in the plane of the surface rather than an axis normal to the vertical plane of symmetry (see fig. 1).

[redacted]

the tangents in equation (14) are equal to the radian values of the angles, the following approximate relationships for small incidence angles are obtained

$$C_{L_{i_T}} = \frac{\partial C_{L_T}}{\partial i_T}$$

$$= \frac{\partial}{\partial i_T}\left[Q \frac{S_T \cos \Gamma_T}{S}\left(k_{TB} + k_{BT}\right)\left(C'N_\alpha\right)_T\left(\alpha + i_T\right)P\right]$$

$$= Q \frac{S_T}{S} \cos^2\Gamma_T\left(k_{TB} + k_{BT}\right)\left(C'N_\alpha\right)_T \qquad (15)$$

$$C_{m_{i_T}} = Q \frac{S_T}{S} \cos^2\Gamma_T\left(k_{TB} + k_{BT}\right)\frac{\bar{x}_T}{\bar{c}}\left(C'N_\alpha\right)_T \qquad (16)$$

In these equations, the calculation of $\left(C'N_\alpha\right)_T$ from equation (2) may be simplified by adoption of the following notation

$$\left(C'N_\alpha\right)_T = \left[\left(C'N_\alpha\right)_T\right]_{\alpha=0} \frac{\left(c_{n_\alpha}\right)_\alpha}{\left(c_{n_\alpha}\right)_{\alpha=0}}$$

$$= \left[\left(C'N_\alpha\right)_T\right]_{\alpha=0}\left[H' + \frac{H'^2 + \frac{1}{2}}{\sqrt{H'^2 + 1}} + \frac{1}{2}\left(1 - 2\frac{\gamma - 1}{\gamma + 1}H'\right)^{\frac{\gamma+1}{\gamma-1}}\right] \qquad (17)$$

where

$$H' = \frac{\gamma + 1}{4}\left(\sqrt{M^2 - 1}\right)\alpha = \frac{\gamma + 1}{4} H$$

The results given by equations (15) to (17) are shown in figure 17 for several combined angles, $\alpha + i_T$. The stabilizer effectiveness, similar to the lift characteristics described earlier, increases substantially with angle of attack at hypersonic speeds. Experimental data for small incidence angles are not available to confirm the trends shown in figure 17.

[redacted]

H 1 4 6

References 3 and 4 present lift and moment data for large incidence angles that may be compared with the moment increments predicted by equation (12). Results for Mach numbers from 2.29 to 6.86 are presented in figure 18 in terms of angle of attack at constant incidence setting (-20° and 15°) and in figure 19 in terms of incidence setting at constant angle of attack (0°). Both figures show fair agreement at the lower Mach numbers. At the higher Mach numbers, however, the stabilizer effectiveness in figure 18, appears to be underestimated at high angles of attack and for negative incidences somewhat overestimated in the lower range. The discrepancy at the high angles of attack is undoubtedly due to the combined influence of dynamic pressure, Mach number, and downwash in the compression field from the lower wing surface briefly described in a preceding section. These shock effects, as discussed in reference 10, occur in varying degree depending upon Mach number, incidence setting, and angle of attack. The large sweep and dihedral angles of the stablizer, however, preclude any relatively simple procedure for estimating these effects.

Further evidence of the various interference effects at large incidence settings is found in the pitching-moment characteristics presented in figure 20 for four test Mach numbers. The comparisons between theory and experiment for a Mach number of 2.29 (fig. 20(a)) show some disagreement primarily in the magnitude of the moment increments at large negative incidences - a probable effect of both the wake from the wing and the large abrupt discontinuity between the fuselage side-fairing and inboard end of the stabilizer. At a Mach number of 2.98 (fig. 20(b)) there is, in addition to the effects of wing wake and fuselage fairing, some evidence of the leading edges of the stabilizer dipping into the compression field from the wing at lift coefficients above 0.4. The immediate result of this interference is a sharp increase in trim lift coefficient and an apparent reduction in airplane stability. This trend becomes more and more pronounced as the Mach number is raised to 4.65 and 6.86 as shown in figures 20(c) and 20(d), respectively.

Damping in Pitch

The buildup procedure of reference 16 is employed also for calculation of the pitching-moment coefficient due to pitching rate about the center of gravity C_{m_q} and to steady vertical acceleration of the center of gravity $C_{m_{\dot{\alpha}}}$. It is assumed that the previously determined interference terms (K factors) for angle-of-attack variations are also applicable to the cases of steady pitching rate and vertical acceleration. The Newtonian limits, which are generally in disagreement with the results from the shock-expansion and small-disturbance theories, are omitted.

[redacted]

[redacted]

Wing.- References 35 and 36 provide charts based on linear theory from which estimates of C_{m_q} and $C_{m_{\dot{\alpha}}}$ for the isolated wing may be obtained. Preliminary inspection of the charts shows that for the assumed center-of-gravity location, the wing damping effects are relatively small. Following the notation used in the lift calculations, the following expressions for C_{m_q} and $C_{m_{\dot{\alpha}}}$ for the wing (including interference) are obtained

$$\left(C_{m_q}\right)_W = \frac{S_W}{S}\left(K_{WB} + K_{BW}\right)\left(\frac{\bar{c}_W}{\bar{c}}\right)^2\left(C'_{m_q}\right)_W \tag{18}$$

$$\left(C_{m_{\dot{\alpha}}}\right)_W = \frac{S_W}{S}\left(K_{WB} + K_{BW}\right)\left(\frac{\bar{c}_W}{\bar{c}}\right)^2\left(C'_{m_{\dot{\alpha}}}\right)_W \tag{19}$$

in which the terms $\left(C'_{m_q}\right)_W$ and $\left(C'_{m_{\dot{\alpha}}}\right)_W$ are obtained from references 35 and 36. It is expected that both quantities would exhibit a nonlinear variation with local angle of attack at hypersonic speeds and should therefore be modified accordingly. In the present analysis the results from linear theory for a given angle of attack were adjusted by the ratio of C_N given by equation (2) to that represented by the product $\left(C_{N_\alpha}\right)_{\alpha=0}\alpha$. The results from equations (18) and (19) are presented in figures 21 and 22 for several angles of attack.

Fuselage.- The damping derivatives for the fuselage may be approximated through application of the relatively simple results derived from slender-body theory in a manner similar to that described in reference 16. It is found that, although slender-body theory alone does not accurately predict the characteristics of nonslender configurations, the ratio of slender-body derivatives may be employed with reasonable accuracy in the following manner

$$\left(C_{m_q}\right)_B = \left(C_{m_\alpha}\right)_B\left(\frac{C_{m_q}}{C_{m_\alpha}}\right)_{\text{slender body}} \tag{20}$$

$$\left(C_{m_{\dot{\alpha}}}\right)_B = \left(C_{m_\alpha}\right)_B\left(\frac{C_{m_{\dot{\alpha}}}}{C_{m_\alpha}}\right)_{\text{slender body}} \tag{21}$$

[redacted]

The static derivative $\left(C_{m_\alpha}\right)_B$ in these expressions has been previously determined by more precise methods (ref. 26). The slender-body ratios may be readily derived from the relationships developed in references 25, 37, and 38, giving

$$\left(\frac{C_{m_q}}{C_{m_\alpha}}\right)_{\text{slender body}} = \frac{-4\left(\frac{L}{\bar{c}}\right)^2 \frac{S_B}{S}\left[\left(1 - \frac{x_o}{L}\right)^2 - \frac{\text{Volume}}{S_B L}\left(\frac{x_o}{L} - \frac{x_c}{L}\right)\right]}{2\left(\frac{L}{\bar{c}}\right)\frac{S_B}{S}\left[\frac{\text{Volume}}{S_B L} - \left(1 - \frac{x_o}{L}\right)\right]} \tag{22}$$

$$\left(\frac{C_{m_{\dot{\alpha}}}}{C_{m_\alpha}}\right)_{\text{slender body}} = \frac{-4\left(\frac{L}{\bar{c}}\right)^2 \frac{S_B}{S}\frac{\text{Volume}}{S_B L}\left(\frac{x_o}{L} - \frac{x_c}{L}\right)}{2\left(\frac{L}{\bar{c}}\right)\frac{S_B}{S}\left[\frac{\text{Volume}}{S_B L} - \left(1 - \frac{x_o}{L}\right)\right]} \tag{23}$$

where x_o/L and x_c/L are the center-of-gravity and area-centroid locations relative to the overall body length, and where the term "volume" designates the actual volume of the fuselage including the side fairings. Figures 21 and 22 show the damping derivatives for the X-15 fuselage as estimated by the previous relationships to be nearly constant in the Mach number range from 2 to 12.

Horizontal tail.- The damping contributions from the horizontal tail are determined by the method of reference 39 from which the following approximate equations are derived

$$\left(C_{m_q}\right)_T = -2Q\,\frac{S_T}{S}\cos^2\Gamma_T\left(C_{L_\alpha}\right)_T\left(K_{TB} + K_{BT}\right)\frac{\bar{x}_T}{\bar{c}}\left[\left(\frac{\bar{x}}{\bar{c}}\right)_T + \overline{\frac{\partial}{\partial z}\left(\frac{\theta_q}{q\bar{c}_W}\right)}\right] \tag{24}$$

$$\left(C_{m_{\dot{\alpha}}}\right)_T = 2Q\,\frac{S_T}{S}\cos^2\Gamma_T\left(C_{L_\alpha}\right)_T\left(K_{TB} + K_{BT}\right)\left(\frac{\bar{x}_T}{\bar{c}}\right)^2\overline{\frac{\partial}{\partial z}\left(\frac{\Omega_\alpha}{\alpha V}\right)} \tag{25}$$

The terms $\overline{\frac{\partial}{\partial z}\left(\frac{\theta_q}{q\bar{c}_W}\right)}$ and $\overline{\frac{\partial}{\partial z}\left(\frac{\Omega_\alpha}{\alpha V}\right)}$ represent the average upwash induced by the wing at the tail location. Both are small, becoming negligible in

[redacted]

the hypersonic range. The tail-plane lift-curve slope is nonlinear, as shown in the preceding sections. Results are presented in figures 21 and 22.

Airplane.- The fuselage is seen in figures 21 and 22 to be the predominant component in the buildup of the airplane damping characteristics, with the tail-damping contribution becoming increasingly significant as angle of attack is increased. The effects of vertical translation are seen in figure 22 to be quite small and may be neglected at Mach numbers above 4. The calculated damping coefficient $\left(C_{m_q} + C'_{m_{\dot{\alpha}}}\right)$ for the airplane with the tail on and off is summarized in figure 23.

Wind-tunnel data from reference 2 are compared with the calculated results at Mach numbers up to 3.5 in figure 24 for both the tail-on and tail-off configurations. The calculated damping with the tail off, for the most part, is less than the experimental result, indicating possibly that the fuselage moments may be underestimated. With the tail on, somewhat better agreement is obtained where the tail incidence is held constant near the zero setting. The large negative incidences employed at the higher angles of attack, it is noted, tend to reduce the overall airplane damping due to the nonlinearity of the tail-plane lift characteristics. Inclusion of these effects in the calculations would reduce the differences noted.

ANALYSIS AND DISCUSSION OF LATERAL-DIRECTIONAL DERIVATIVES

The sideslip and the rotary and control derivatives for yaw and roll are considered in the following section. The principal interference flow fields affecting these derivatives have been briefly described in an earlier section, however more detailed information may be found in references 14, 40, and 41. In general, the procedures, assumptions, and nomenclature employed are similar to those for the longitudinal derivatives. It is assumed, in addition, that the sideslip angles are small and the incidence of the horizontal tail is zero.

The Newtonian limits are determined for the sideslip derivatives only.

Sideslip Derivatives

The procedure of reference 16, when applied to the case of steady sideslip leads to the following basic relationships for the side-force, yawing-moment, and rolling-moment coefficients due to the wing, fuselage, horizontal tail, and the upper and lower segments of the vertical tail

UNCLASSIFIED

$$C_{Y_\beta} = \frac{S_W}{S}\left(\frac{C'Y_\beta}{\alpha}\right)_W \alpha + \frac{\partial}{\partial\beta}\left(C_{Y_B}\right)_{\text{inviscid}} + \frac{\partial}{\partial\beta}\left(C_{Y_B}\right)_{\text{viscous}}$$

$$+ Q\,\frac{S_T \sin \Gamma_T}{S}\left(K_{TB} + K_{BT}\right)\left(1 - \frac{d\epsilon}{d\alpha}\right)\frac{\partial C'N_T}{\partial\beta}$$

$$+ Q_L\,\frac{S_L}{S}\left(K_{LB} + K_{BL}\right)\left(C'N_\alpha\right)_L\left(1 - \frac{d\sigma_L}{d\beta}\right)$$

$$+ Q_U\,\frac{S_U}{S}\left(K_{UB} + K_{BU}\right)\left(C'N_\alpha\right)_U\left(1 - \frac{d\sigma_U}{d\beta}\right) \qquad (26)$$

$$C_{n_\beta} = \frac{S_W}{S}\left(\frac{C'n_\beta}{\alpha}\right)_W \alpha + \left[\frac{\bar{x}_B}{b}\left(C_{Y_\beta}\right)_B\right]_{\text{inviscid}} + \left[\frac{\bar{x}_B}{b}\left(C_{Y_\beta}\right)_B\right]_{\text{viscous}}$$

$$+ \left(\frac{\bar{x}_T}{b}\right)\left(C_{Y_\beta}\right)_T + \left(\frac{\bar{x}_L}{b}\right)\left(C_{Y_\beta}\right)_L + \left(\frac{\bar{x}_U}{b}\right)\left(C_{Y_\beta}\right)_U \qquad (27)$$

$$C_{l_\beta} = \frac{S_W}{S}\left(\frac{C'l_\beta}{\alpha}\right)_W \alpha + \left(C_{l_\beta}\right)_T + \left(C_{l_\beta}\right)_L + \left(C_{l_\beta}\right)_U \qquad (28)$$

These equations are the basic forms from which the sideslip derivatives for the individual components and for the complete airplane are derived in the following subsections. The rolling moments due to the fuselage are negligible and have been omitted from equation (28). As in the earlier analyses, the interference lifts between the fuselage and various lifting surfaces are combined with the lift for the adjacent surface, and, where appropriate, the nonlinear relationships given by equations (2) and (3) are introduced. The results as applied to the X-15 are presented in figures 25 to 29 for angles of attack of 0°, 8°, 16°, and 24°.

Wing.- The terms $\left(\frac{C'Y_\beta}{\alpha}\right)_W$ and $\left(\frac{C'n_\beta}{\alpha}\right)_W$ in equations (26) and (27) originate primarily from edge-suction forces existing along the wing tips. These effects are found from the results of reference 42 to be extremely small in comparison with those due to the fuselage and vertical tail, and, therefore, are neglected. The results of reference 43 indicate that the

term $\left(\frac{C'_{l_\beta}}{\alpha}\right)_W$ for the wing alone is also very small. For the wing in the presence of the body, however, it is demonstrated in reference 44 that a substantial rolling moment will occur due to cross-coupling effects of the sidewash velocities that arise when the wing-body combination is displaced both in sideslip and angle of attack. According to the method of reference 44 as applied to bodies of circular cross section, this moment is given approximately by the relationship

$$\left(C_{l_\beta}\right)_W = -\frac{S_W}{S}\left(C'_{N_\alpha}\right)_W \frac{K_\varphi}{\tan \bar{\epsilon}}\left(\frac{2\bar{y}_W}{b}\right)_\varphi \alpha \tag{29}$$

or

$$\left(C_{l_\beta}\right)_W = -\frac{S_W}{S}\frac{K_\varphi}{\tan \bar{\epsilon}}\left(\frac{2\bar{y}_W}{b}\right)_\varphi C'_{N_W} \tag{30}$$

This equation is applied to the X-15 fuselage by replacing the latter with an equivalent circular cylinder having a cross-sectional area equal to the actual cross-sectional area at the wing-body juncture (including the side fairings). For hypersonic Mach numbers the nonlinear variation of the term C'_{N_W} with angle of attack should not be overlooked. The results from equation (30) are presented in figure 27 which shows the cross-coupling effect to be significant at high angles of attack.

Fuselage.- Equations (6) and (7) for the force coefficients due to inviscid and viscous crossflow, when converted to side force in combined sideslip and angle of attack, transform to the following overall expression

$$C_{Y_B} = R_\varphi \frac{S_B}{S}\left(C'_{N_\alpha}\right)_B \varphi \cos \mu + \eta \bar{c}_{d_c} \frac{A_\varphi}{S} \varphi^2 \cos \mu \tag{31}$$

The term φ is the angle of attack as measured in the plane containing the free-stream-velocity vector and the body axis, and μ is the angle between this plane and the X-Y plane in figure 4(b). The term R_φ corresponds to R_α in equation (6) and varies from 1.4 for displacements in pitch ($\beta = 0$) to approximately 0.9 for displacements in yaw ($\alpha = 0$). Correspondingly, the term A_φ (the counterpart of A_α) varies from 0.60 to 0.485. It can be shown that

$$\cos \mu = \frac{\sin \beta}{\sin \varphi} \approx \frac{\beta}{\varphi} \tag{32}$$

such that the derivative $\left(C_{Y_\beta}\right)_B$ may be approximated as

$$\left(C_{Y_\beta}\right)_B = \frac{\partial C_{Y_B}}{\partial \beta}$$

$$= R_\varphi \frac{S_B}{S}\left(C'_{N_\alpha}\right)_B + \eta \bar{c}_{d_c} \frac{A_\varphi}{S} \varphi \qquad (33)$$

assuming the terms R_φ, $\left(C_{N_\alpha}\right)_B$, η, $\bar{c}_{d_c}$, and A_φ to be constant. The angle φ is related to α and β by the equation

$$\sin \varphi = \sqrt{\sin^2\alpha + \sin^2\beta - \sin^2\alpha \sin^2\beta} \qquad (34)$$

which, for relatively small angles, simplifies to the form

$$\varphi \approx \sqrt{\alpha^2 + \beta^2} \qquad (35)$$

The resultant values for the various factors assumed to be constant in equation (33) may be determined for combined α and β by resolving the known magnitudes for $\alpha = 0$ and $\beta = 0$ into components proportional to $\frac{\alpha}{\sqrt{\alpha^2 + \beta^2}}$ and $\frac{\beta}{\sqrt{\alpha^2 + \beta^2}}$. This procedure is not exact, however, since the resultant-force vector, as pointed out in reference 14, does not necessarily lie in the plane containing the velocity vector and the body axis. The various coefficients for the inviscid and viscous crossflow terms are determined by the methods discussed previously in the longitudinal analysis. In the calculation of $\left(C_{N_\alpha}\right)_B$ for sideslip alone ($\alpha = 0^\circ$), however, the X-15 fuselage and canopy have been approximated by a cone-cylinder combination rather than an ogive and cylinder, as assumed previously for angle of attack.

The yawing-moment derivative for the fuselage at combined angles of attack and sideslip may then be obtained from the relationship

$$\left(C_{n_\beta}\right)_B = \left[\left(C_{Y_\beta}\right)_B \frac{\bar{x}_B}{b}\right]_{\text{inviscid}} + \left[\left(C_{Y_\beta}\right)_B \frac{\bar{x}_B}{b}\right]_{\text{viscous}} \qquad (36)$$

in which the moment arm for the viscous crossflow should be determined with due consideration given to the downstream location of the initial

point of crossflow separation along the body axis as discussed in reference 31. The wing, it is noted, has little or no blanketing effect on the crossflow in sideslip.

The side-force and yawing-moment derivatives for the X-15 fuselage are shown in figures 25 and 26. The effect of Mach number is small, but an increase in angle of attack is accompanied by a gradual increase of both derivatives.

The Newtonian limits are derived from the results of reference 13 in the manner described previously for the longitudinal characteristics (eq. (8)). The following equation is obtained for the nose cone and cylindrical afterbody sections

$$\left(C_{Y_\beta}\right)_B = 2\,\frac{S_{NC}}{S}\cos^2\tau_{NC}\cos\alpha + 2\,\frac{S_{AB}}{S}\,\alpha\cos\nu \qquad (37)$$

in which S_{AB} is the side area of the afterbody section. The results from equation (37) are presented in figures 25 and 26.

Horizontal tail.- The side force from the horizontal tail arises solely from dihedral angle, and in derivative form is given by

$$\left(C_{Y_\beta}\right)_T = Q\,\frac{S_T \sin\Gamma_T}{S}\left(K_{TB} + K_{BT}\right)\frac{\partial}{\partial\beta}\left(C'_{N_T}\right)\left(1 - \frac{d\epsilon}{d\alpha}\right) \qquad (38)$$

The term C'_{N_T} is proportional to an effective angle of attack α_e of the tail defined as follows for the combined angles of attack and sideslip (ref. 45, appendix B)

$$\alpha_e = \tan^{-1}\left(\tan\alpha\cos\beta - \frac{\sin\beta\tan\Gamma_T}{\cos\alpha}\right) \qquad (39)$$

For small angles of sideslip

$$\frac{\partial\alpha_e}{\partial\beta} \approx -\tan\Gamma_T\cos\alpha \qquad (40)$$

and equation (38) becomes

$$\left(C_{Y_\beta}\right)_T = -Q\,\frac{S_T \sin\Gamma_T}{S}\left(K_{TB} + K_{BT}\right)\tan\Gamma_T\cos\alpha\left(C'_{N_\alpha}\right)_T\left(1 - \frac{d\epsilon}{d\alpha}\right) \qquad (41)$$

UNCLASSIFIED

where $\left(C'N_\alpha\right)_T$ is given by equation (17). The upwash effect due to fuselage crossflow is assumed to be negligible at the tail, hence the term K_{TB} becomes unity. Furthermore, the fuselage may be regarded as having zero dihedral angle, and thus the term K_{BT} is zero.

The yawing-moment derivative for the horizontal tail is readily obtained as

$$\left(C_{n_\beta}\right)_T = -\left(\frac{\bar{x}_T}{\bar{c}}\right)\frac{\bar{c}}{b}\left(C_{Y_\beta}\right)_T \tag{42}$$

where $\bar{x}_T$ has been determined previously (see eq. (9)).

The sidewash cross-coupling effects mentioned previously in regard to the wing-body rolling moments are assumed to occur also in the vicinity of the fuselage and the horizontal- and vertical-tail surfaces. Following the method of reference 44, the rolling-moment derivative for the horizontal tail becomes

$$\left(C_{l_\beta}\right)_T = -Q\,\frac{S_T}{S}\,K_{TB}\left(\frac{2\bar{y}_T}{b}\right)_\alpha \frac{\partial C'N_T}{\partial\beta} - Q\,\frac{S_T}{S}\,\frac{K_\varphi}{\tan\epsilon}\left(\frac{2\bar{y}_T}{b}\right)_\varphi C'N_T \tag{43}$$

For small sideslip angles, the expression

$$\left(C_{l_\beta}\right)_T = Q\,\frac{S_T}{S}\,K_{TB}\left(\frac{2\bar{y}_T}{b}\right)_\alpha\left(C'N_\alpha\right)_T \tan\Gamma_T\cos\alpha - Q\,\frac{S_T}{S}\,\frac{K_\varphi}{\tan\epsilon}\left(\frac{2\bar{y}_T}{b}\right)_\varphi C'N_T \tag{44}$$

is obtained with the aid of equation (40).

The contributions of the horizontal tail to the overall sideslip derivatives are generally quite small, as can be seen in figures 25 to 27.

The simple Newtonian approximations for the tail-plane derivatives are given by

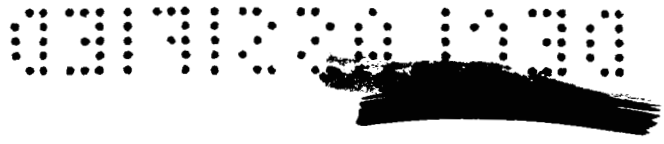

$$
\left.
\begin{aligned}
C_{Y_T} &= \frac{S_T \sin \Gamma_T}{S}\left(2 \sin^2 \alpha_e\right) \\
\left(C_{Y_\beta}\right)_T &= \frac{\partial}{\partial \beta}\left(C_{Y_T}\right) \\
&= \frac{S_T \sin \Gamma_T}{S}\, 4 \sin \alpha_e \frac{\partial \alpha_e}{\partial \beta} \\
&\approx -4 \frac{S_T}{S} \sin^2 \Gamma_T \alpha \\
\left(C_{n_\beta}\right)_T &\approx 4\left(\frac{\bar{x}_T}{b}\right)\frac{S_T}{S} \sin^2 \Gamma_T \alpha \\
\left(C_{l_\beta}\right)_T &\approx 4\left(\frac{\bar{y}_T}{b}\right)\frac{S_T}{S} \sin^2 \Gamma_T \alpha
\end{aligned}
\right\} \qquad (45)
$$

Figures 25 to 27 show that the Newtonian results for the horizontal tail are not significant.

Vertical tail.- For improved stability at high Mach numbers, 10° wedge-type sections were chosen for both the upper and lower tail surfaces. The normal-force coefficients for these surfaces may be determined first by applying the results of linear theory (ref. 22), assuming the surfaces to be flat plates, and then by correcting the flat-plate values by the ratio of the lift-curve slopes for the wedge and flat plate given in reference 46. The terms $\left(C_{N_\alpha}\right)_L$ and $\left(C_{N_\alpha}\right)_U$ in equation (26) are considered to have been modified in this manner. The interference coefficients of reference 16 are introduced, but the hypersonic nonlinear effects are neglected for small sideslip angles. As noted in the description of the interference flow fields, the effect of the displacements of the wing and fuselage vortices relative to the tail surfaces is believed to be slight at small sideslip angles; consequently, the term $d\sigma/d\beta$ in equation (26) will be neglected. The side-force derivative for the vertical tails therefore becomes

$$
\left(C_{Y_\beta}\right)_L + \left(C_{Y_\beta}\right)_U = Q_L \frac{S_L}{S}\left(K_{LB} + K_{BL}\right)\left(C'_{N_\alpha}\right)_L + Q_U \frac{S_U}{S}\left(K_{UB} + K_{BU}\right)\left(C'_{N_\alpha}\right)_U \qquad (46)
$$

DECLASSIFIED

In general, the various terms in equation (46) for the upper and lower surfaces differ. Particularly noteworthy are the large differences in Q that occur with increasing angle of attack. For small angles, the magnitudes shown in figure 3 may be applied equally to both surfaces. At moderate and high angles of attack, however, the upper tail is largely contained within the shock-expansion field from the upper wing and body surfaces and the lower tail within the compression field from the lower surfaces. Consequently, Q for the upper tail diminishes while that for the lower tail increases rapidly as shown in figure 28. The variations of Q shown in this figure were estimated from the charts of reference 12 for supersonic flow past wedges and for Prandtl-Meyer expansions.

The yawing-moment characteristics for the vertical tail are readily found from equation (46) and the previously determined moment arms.

Rolling moments from the vertical tail are generated by differences in geometry and dynamic pressure between the upper and lower surfaces as well as by the previously mentioned cross coupling of sidewash velocities for the fuselage-tail combination. The following relationships from reference 44 are used for calculation of their combined effect

$$\left.\begin{aligned}\left(C_{l_\beta}\right)_L &= -Q_L \frac{S_L}{S}\left[K_{LB}\left(\frac{2\bar{y}_L}{b}\right)_\alpha - \frac{K_\varphi}{\tan\epsilon}\left(\frac{2\bar{y}_L}{b}\right)_{\varphi}^{\alpha}\right]\left(C'_{N_\alpha}\right)_L \\ \left(C_{l_\beta}\right)_U &= Q_U \frac{S_U}{S}\left[K_{UB}\left(\frac{2\bar{y}_U}{b}\right)_\alpha + \frac{K_\varphi}{\tan\epsilon}\left(\frac{2\bar{y}_U}{b}\right)_{\varphi}^{\alpha}\right]\left(C'_{N_\alpha}\right)_U\end{aligned}\right\} \tag{47}$$

Values for the coefficients K_{LB}, K_{UB}, and K_φ and for the moment arms $\left(\frac{2\bar{y}_{L,U}}{b}\right)_\alpha$ and $\left(\frac{2\bar{y}_{L,U}}{b}\right)_\varphi$ are determined from the charts given in reference 44.

Newtonian theory provides the following simple expressions for the vertical-tail characteristics, assuming the sideslip angles to be less than the semivertex angle of the wedge profiles ($\tau_v = 5^\circ$)

$$\left.\begin{aligned}
\left(C_{Y_\beta}\right)_L &= -8\,\frac{S_L}{S}\,\tau_v \\
\left(C_{n_\beta}\right)_L &= 8\,\frac{S_L}{S}\,\tau_v\,\frac{\bar{x}_L}{b} \\
\left(C_{l_\beta}\right)_L + \left(C_{l_\beta}\right)_U &= 8\tau_v\left(-\frac{\bar{z}_L}{b}\,\frac{S_L}{S} + \frac{\bar{z}_U}{b}\,\frac{S_U}{S}\right)
\end{aligned}\right\} \tag{48}$$

Figures 25 to 27 illustrate the dominating effect that the vertical tails have on the sideslip characteristics of the X-15. Particularly remarkable are the rapid gain in effectiveness of the lower surface and the loss in effectiveness of the upper surface as angle of attack is increased. As a result, the directional stability at hypersonic speeds remains at a high level, and the net contribution of the vertical tails to the dihedral effect changes from negative to positive magnitudes as angle of attack is increased. Newtonian theory, as shown in the figures, does not predict these characteristics.

Airplane.- The sideslip characteristics for the airplane at angles of attack of 0°, 8°, 16°, and 24°, as built up from the foregoing component effects, are presented in figure 29 for both the vertical tail on and off. The airplane, it is noted, is predicted to be directionally stable well in excess of its estimated limit speed, but the calculated dihedral effect C_{l_β}, due to the pronounced asymmetry in effectiveness of the upper and lower vertical tails, changes rapidly from near zero to relatively large positive magnitudes as angle of attack is increased. This positive trend in C_{l_β} is generally undesirable from the standpoint of the Dutch roll stability due, as discussed in reference 47, to its indirect effect of reducing the directional stability of the airplane as angle of attack is increased. Thus, from a simplified analysis of the lateral-directional equations of motion the effective directional-stability parameter

$$C_{n_\beta}{}^* = C_{n_\beta} - \alpha\,\frac{I_X}{I_Z}\,C_{l_\beta} \tag{49}$$

is evolved which shows that instability in Dutch roll is promoted by a positive trend in C_{l_β} at high angles of attack. It is also noteworthy that the interference of the wing and fuselage vortices on the stability contribution from the upper vertical tail at positive angles of attack, due to the loss in effectiveness of the surface, is of little consequence as hypersonic speeds are attained.

Figures 30 to 32 present a comparison of the calculated sideslip derivatives with those obtained in the wind-tunnel tests of references 1 to 4. Generally fair agreement is noted in these figures for the vertical-tail-off results, however the vertical-tail contribution (difference between the tail-on and tail-off values) appears to have been overestimated at the higher angles of attack for Mach numbers of 2.01, 4.68, and 6.86. The discrepancies at a Mach number of 2.01 are believed to be associated with detachment of the wing leading-edge shock waves as high angles of attack are approached (see fig. 4 of ref. 12). With shock detachment a substantial weakening of the wing compression field, and hence also the tail contributions, would be expected to occur, although little can be predicted by present methods of the mixed-flow characteristics downstream from detached shocks (see ref. 48). The discrepancies at the two highest Mach numbers result in part from the extension of the lower vertical surface through the wing-fuselage compression field into the reduced dynamic pressure of the free stream at the higher angles of attack - an effect not taken into account in the foregoing calculations. The improvements gained by inclusion of this effect are illustrated in figure 33. Since methods for predicting the position and shape of wing-body shock fields at high angles of attack appear to be unavailable at this time, the proportions of the lower surface within and beyond the compression field were estimated from schlieren photographs obtained from references 3 and 4 and unpublished sources. The directional stability as a result of this change is somewhat reduced at the higher angles of attack, but the dihedral effect is also less unstable. The general agreement between theory and experiment, although improved in some areas, is still not completely satisfactory, indicating that other effects not accounted for are present.

It should be observed also that large negative incidence settings of the horizontal tail in which the leading edges penetrate the wing compression field will, due to the expanding flow around the leading edge, cause noticeable reductions in effectiveness of the lower vertical surface at high angles of attack. Although the complex geometry of the X-15 precludes any ready calculation of this interference effect, it would be expected that the dynamic directional stability of the airplane (eq. (49)) may be improved when it is trimmed for level flight at high angles of attack. This possible improvement, which would arise primarily from the reduced unstable trend in C_{l_β}, is indicated in the results of preliminary wind-tunnel tests at high angles of attack.

The results from Newtonian theory, as shown in figure 29, do not in general agree with the limiting values approached by the other methods at high Mach numbers. The Newtonian approximation therefore, since it appears to be generally inadequate for the static derivatives, is omitted from the remaining analyses of the rotary and control derivatives.

[redacted]

[redacted]

Derivatives Due to Yawing

The derivations of the side-force, yawing-moment, and rolling-moment coefficients due to steady yawing rate follow closely those due to sideslip in the preceding section, and equations (26) to (28) comprise the basic relationships from which the airplane yawing derivatives may be deduced. As before, the fuselage rolling moments are insignificant and are therefore disregarded. Results are presented in figures 34 to 39.

Wing.- Wing effects due to yawing are caused by suction forces along the subsonic edges and by spanwise variations of velocity and Mach number. Estimates of these effects are presented in reference 42, which indicates that the wing force and moment coefficients in the present application are quite small compared to those due to the fuselage and vertical-tail surfaces. The derivatives $\left(\frac{C_{Y_r}}{\alpha}\right)_W$ and $\left(\frac{C_{n_r}}{\alpha}\right)_W$ therefore are neglected. The rolling-moment derivative $\left(\frac{C_{l_r}}{\alpha}\right)_W$, has been retained as shown in figure 36. The lateral-acceleration derivatives ($\dot{\beta}$ terms) for the wing are also found to be negligible (ref. 49).

Fuselage.- Slender-body theory is used to estimate the side-force and yawing-moment coefficients due to yawing in the manner described earlier in the pitch-damping calculations, that is

$$\left.\begin{aligned}
\left(C_{Y_r}\right)_B &= \left(C_{Y_\beta}\right)_B\left(\frac{C_{Y_r}}{C_{Y_\beta}}\right)_{\text{slender body}} \\
\left(C_{n_r}\right)_B &= \left(C_{n_\beta}\right)_B\left(\frac{C_{n_r}}{C_{n_\beta}}\right)_{\text{slender body}} \\
\left(C_{Y_{\dot\beta}}\right)_B &= \left(C_{Y_\beta}\right)_B\left(\frac{C_{Y_{\dot\beta}}}{C_{Y_\beta}}\right)_{\text{slender body}} \\
\left(C_{n_{\dot\beta}}\right)_B &= \left(C_{n_\beta}\right)_B\left(\frac{C_{n_{\dot\beta}}}{C_{n_\beta}}\right)_{\text{slender body}}
\end{aligned}\right\} \qquad (50)$$

where $\left(C_{Y_\beta}\right)_B$ and $\left(C_{n_\beta}\right)_B$ are given by equations (33) and (36), respectively. The various slender-body terms are derived from the results of references 37 and 25, giving (see also eqs. (22) and (23))

[redacted]

DECLASSIFIED

$$\left.\begin{aligned}
\left(\frac{C_{Y_r}}{C_{Y_\beta}}\right)_{\text{slender body}} &= \frac{-4\,\frac{L}{b}\,\frac{S_B}{S}\left(1 - \frac{x_o}{L}\right)}{-2\,\frac{S_B}{S}} \\
\left(\frac{C_{n_r}}{C_{n_\beta}}\right)_{\text{slender body}} &= -\left(\frac{\bar{c}}{b}\right)\left(\frac{C_{m_q}}{C_{m_\alpha}}\right)_{\text{slender body}} \\
\left(\frac{C_{Y_{\dot\beta}}}{C_{Y_\beta}}\right)_{\text{slender body}} &= \frac{4\,\frac{\text{Volume}}{Sb}}{-2\,\frac{S_B}{S}} \\
\left(\frac{C_{n_{\dot\beta}}}{C_{n_\beta}}\right)_{\text{slender body}} &= \left(\frac{\bar{c}}{b}\right)\left(\frac{C_{m_{\dot\alpha}}}{C_{m_\alpha}}\right)_{\text{slender body}}
\end{aligned}\right\} \qquad (51)$$

The results from equations (50) and (51) are presented in figures 34 and 35. The derivative $\left(C_{n_{\dot\beta}}\right)_B$, like $\left(C_{m_{\dot\alpha}}\right)_B$, is noted in figure 35 to be small.

Horizontal and vertical tails.- The yawing derivatives for the tail surfaces may be approximated by the relatively simple approach proposed in reference 9, in which the yawing derivatives are related directly to those for sideslip in the following way

$$C_{Y_r} = -\frac{\partial C_Y}{\partial \beta}\,\frac{\partial \beta}{\partial\left(\frac{rb}{2V}\right)} = -C_{Y_\beta}\,\frac{\partial \beta}{\partial\left(\frac{rb}{2V}\right)} \qquad (52)$$

Assuming the yaw angles to be small, β may be expressed as $2\,\frac{\bar{x}}{b}\left(\frac{rb}{2V}\right)$, whence

$$\frac{\partial \beta}{\partial\left(\frac{rb}{2V}\right)} = 2\,\frac{\bar{x}}{b}$$

and

[redacted]

[redacted]

$$\left.\begin{aligned}
\left(C_{Y_r}\right)_{T,L,U} &= -2\,\frac{\bar{x}_{T,L,U}}{b}\left(C_{Y_\beta}\right)_{T,L,U} \\
\left(C_{n_r}\right)_{T,L,U} &= -2\,\frac{\bar{x}_{T,L,U}}{b}\left(C_{n_\beta}\right)_{T,L,U} \\
\left(C_{l_r}\right)_{T,L,U} &= -2\,\frac{\bar{x}_{T,L,U}}{b}\left(C_{l_\beta}\right)_{T,L,U}
\end{aligned}\right\} \qquad (53)$$

where the dimension $\bar{x}$ is the moment arm of either the horizontal or vertical tail. Figures 34 to 36 show that the magnitudes of these quantities are negligible for the horizontal tail and for the upper vertical tail at high angles of attack. The lower vertical tail, on the other hand, exhibits substantial damping effects.

The effect of sidewash lag at the vertical tail is analyzed in reference 50, in which it is shown that the $\dot{\beta}$ derivatives are related to the rate of change of sidewash angle with angle of sideslip as follows

$$\left.\begin{aligned}
C_{Y_{\dot{\beta}}} &= -2\left(\frac{\bar{x}_{L,U}}{b}\right)\left(C_{Y_\beta}\right)_{L,U}\frac{\partial\sigma_{L,U}}{\partial\beta} \\
C_{n_{\dot{\beta}}} &= 2\left(\frac{\bar{x}_{L,U}}{b}\right)^2\left(C_{Y_\beta}\right)_{L,U}\frac{\partial\sigma_{L,U}}{\partial\beta}
\end{aligned}\right\} \qquad (54)$$

The sidewash variations at the tail, however, are not significant, and the $\dot{\beta}$ derivatives therefore have been dropped.

Airplane.- The calculated damping-in-yaw characteristics for the airplane are summarized in figure 37, in which the general level of damping is observed to increase with increasing angle of attack. The asymmetry in loading on the vertical surfaces introduces negative rolling moments which also increase with angle of attack. These trends are compared with the results from wind-tunnel tests (ref. 2) in figures 38 and 39. The predicted levels of yaw damping $\left(C_{n_r} - C_{n_{\dot{\beta}}}\right)$ appear to be in good agreement with the test results except, perhaps, in the higher angle-of-attack range at the lower Mach numbers. The rolling derivatives $\left(C_{l_r} - C_{l_{\dot{\beta}}}\right)$, on the other hand, do not agree in either magnitude or trend except near zero angle of attack, although some improvement would be gained if the partial emergence of the lower vertical tail from the

[redacted]

wing-body compression field were taken into account as previously discussed in relation to the airplane dihedral effect.

Derivatives Due to Rolling

The airplane force and moment coefficients due to steady rolling velocity, as determined by summing the various component and interference characteristics, are presented in figures 40 to 45. The fuselage, when considered as an isolated body, is assumed to have zero loading; however, in relation to the adjacent components its presence must be taken into account. The basic relationships for steady rolling are

$$C_{Y_p} = \left(\frac{C_{Y_p}}{\alpha}\right)_W \alpha + \left(C_{Y_p}\right)_T + \left(C_{Y_p}\right)_{L,U} \tag{55}$$

$$C_{n_p} = \left(\frac{C_{n_p}}{\alpha}\right)_W \alpha + \left(C_{n_p}\right)_T + \left(C_{n_p}\right)_{L,U} \tag{56}$$

$$C_{l_p} = \left(C_{l_p}\right)_W + \left(C_{l_p}\right)_T + \left(C_{l_p}\right)_{L,U} \tag{57}$$

Wing.- Side forces and yawing moments on a wing with supersonic leading edges are generated solely by tip suction forces as noted in reference 51. For high taper this effect is generally small but may become noticeable at high angles of attack. The terms $\left(\frac{C_{Y_p}}{\alpha}\right)_W$ and $\left(\frac{C_{n_p}}{\alpha}\right)_W$ for the X-15 wing in equations (55) and (56), as determined from the results of reference 51, are shown in figures 40 and 41 to be quite significant at high angles of attack.

The damping in roll for the wing is the predominant derivative in this group. Its magnitude may be readily determined from the results of linear theory in reference 22, but should be corrected for wing-body interference and for the nonlinear variations with angle of attack at hypersonic speeds. The slender-body results of reference 52 may be applied as a correction for wing-body interference, and equation (17) as an adjustment for nonlinearity. Then

$$\left(C_{l_p}\right)_W = \frac{\left(c_{n_\alpha}\right)_\alpha}{\left(c_{n_\alpha}\right)_{\alpha=0}} \left(C'_{l_p}\right)_W \left[\frac{\left(C_{l_p}\right)_{WB}}{\left(C_{l_p}\right)_W}\right]_{\text{slender body}} \tag{58}$$

[redacted]

where $\left(C'_{l_p}\right)_W$ is obtained from reference 22. (See also ref. 53 for wing-body combinations.)

Figure 42 shows that the damping in roll for the wing, as predicted by equation (58), should increase substantially with angle of attack at high Mach numbers.

Horizontal tail.- The geometric dihedral, as well as tip suction forces, introduces small side forces and yawing moments due to rolling of the horizontal tail. Their magnitudes, however, are reduced somewhat by the downwash from the wing as described in reference 9. When corrected for downwash effects, the coefficient for the side force due to tip suction, a rather small effect compared with that due to dihedral, may be approximated as

$$\left[\left(C_{Y_p}\right)_T\right]_{\text{tip suction}} = Q\,\frac{S_T \cos \Gamma_T}{S}\left(\frac{b_T}{b}\right)\left[1 - \frac{\left(\frac{w}{V}\right)_{av}}{\frac{pb}{2V}}\right]\left(\frac{C_{Y_p}}{\alpha}\right)_T\left(\alpha \cos \Gamma_T\right) \quad (59)$$

wherein values for $\left(\frac{C_{Y_p}}{\alpha}\right)_T$ may be obtained from reference 51. A rough estimate of the downwash parameter $\left(\frac{w}{V}\right)_{av}\Big/\frac{pb}{2V}$ may be deduced from the results for a similar configuration in reference 9. The side-force coefficient resulting from dihedral is proportional to the loading on the tail due to roll, and may be calculated with sufficient accuracy by the expression

$$\left[\left(C_{Y_p}\right)_T\right]_{\text{dihedral}} = Q\,\frac{S_T \sin \Gamma_T}{S}\left(\frac{b_T}{b}\right)\left[\frac{di_T}{d\left(\frac{pb}{2V}\right)} - \frac{\left(\frac{w}{V}\right)_{av}}{\left(\frac{pb}{2V}\right)}\right]\left(C_{N_\alpha}\right)_T\left[\frac{\left(C_{l_p}\right)_{WB}}{\left(C_{l_p}\right)_W}\right]_{\text{slender body}} \quad (60)$$

Interference between the fuselage and tail is taken into account by introducing the slender-body term from reference 52 for cruciform tail surfaces. The term $di_T\Big/d\left(\frac{pb}{2V}\right)$ may be calculated with the aid of strip theory, as suggested in references 54 and 55, that is,

$$\frac{di_T}{d\left(\frac{pb}{2V}\right)} = \frac{57.3}{2}\frac{1 + 3\lambda_T}{1 + 2\lambda_T} \tag{61}$$

and $\left(C_{N_\alpha}\right)_T$ is given by equation (17).

The corresponding yawing-moment coefficients are obtained by multiplying the results from equations (59) and (60) by the moment arm $\bar{x}_T/b$. The side-force and yawing-moment results are shown in figures 40 and 41.

The roll damping due to the horizontal tail is calculated in the same manner as the wing damping (eq. (58)), but must be additionally corrected for wing downwash effects. Thus

$$\left(C_{l_p}\right)_T = Q\frac{S'_T}{S}\left(\frac{b_T}{b}\right)^2\frac{\left(c_{n_\alpha}\right)_\alpha}{\left(c_{n_\alpha}\right)_{\alpha=0}}\left[1 - \frac{\left(\frac{w}{V}\right)_{av}}{\left(\frac{pb}{2V}\right)}\right]\left(C'_{l_p}\right)_T\left[\frac{\left(C_{l_p}\right)_{TB}}{\left(C_{l_p}\right)_T}\right]_{\text{slender body}} \tag{62}$$

where $\left(C'_{l_p}\right)_T$ is obtained from reference 22. The area S'_T in this equation is the total area including the portion enclosed within the fuselage, and the slender-body terms are for cruciform configurations (ref. 52). As shown in figure 42 the tail-plane damping is relatively small.

Vertical tail.- The side-force coefficients due to rolling of the upper and lower vertical tails are of opposite sign and may be determined by expressions similar to equation (60), that is,

$$\left.\begin{aligned}\left(C_{Y_p}\right)_L &= -Q_L\frac{V_\infty}{V_L}\frac{S_L}{S}\frac{b_L}{b}\left[\frac{di}{d\left(\frac{pb}{2V}\right)} - \frac{\left(\frac{v}{V}\right)_{av}}{\left(\frac{pb}{2V}\right)}\right]_L\left(C'_{N_\alpha}\right)_L\left[\frac{\left(C_{l_p}\right)_{LB}}{\left(C_{l_p}\right)_L}\right]_{\text{slender body}}\\ \left(C_{Y_p}\right)_U &= Q_U\frac{V_\infty}{V_U}\frac{S_U}{S}\frac{b_U}{b}\left[\frac{di}{d\left(\frac{pb}{2V}\right)} - \frac{\left(\frac{v}{V}\right)_{av}}{\left(\frac{pb}{2V}\right)}\right]_U\left(C'_{N_\alpha}\right)_U\left[\frac{\left(C_{l_p}\right)_{UB}}{\left(C_{l_p}\right)_U}\right]_{\text{slender body}}\end{aligned}\right\} \tag{63}$$

[redacted]

The sidewash parameter $\frac{\left(\frac{v}{V}\right)_{av}}{pb/2V}$, similar to the downwash parameter for the horizontal tail, has been determined for a similar configuration in reference 9. (For subsonic leading edges see ref. 56.) The factor V_∞/V is introduced because of the relatively large variations in local-stream velocity that occur at the higher angles of attack. This factor may be readily estimated from the charts of reference 12. Although the two surfaces tend to nullify one another at low angles of attack, their effects become highly unsymmetrical as the higher angles are approached, as shown in figures 40 and 41. The corresponding yawing-moment coefficients are easily obtained from the previously determined moment arms $\frac{\bar{x}_{L,U}}{b}$.

Equation (62) may be readily adapted to calculation of the damping-moment derivatives for the vertical surfaces. The downwash parameter should be replaced by that for sidewash, and the velocity ratio V_∞/V may be introduced for greater accuracy. The vertical-tail damping, however, is not consequential, as shown in figure 42.

Airplane.- The predicted rolling derivatives C_{Y_p} and C_{n_p} for the airplane are given in figure 43, in which the magnitudes of both derivatives are shown in general to be insignificant at low angles of attack, but to grow rapidly with increasing angle of attack. The theoretical damping in roll is also seen in the same figure to increase substantially with angle of attack. For Mach numbers up to 3.5 these trends are confirmed experimentally to some extent as shown in figures 44 and 45, but the agreement is qualitative at best. The wide scatter in the data, notably in the tail-off results, leaves the comparison somewhat in doubt as to which source, experiment or theory, is the more accurate.

Lateral-Directional Control Derivatives

For aerodynamic directional control the X-15 is equipped with all-movable tip-control surfaces which basically comprise the outer segments of the upper and lower vertical stabilizers. The surface deflections are limited to $\pm 7\frac{1}{2}^\circ$. Lateral control, provided through differential incidence of the horizontal stabilizers, has an angular range of $\pm 7\frac{1}{2}^\circ$ for each panel except at settings near limiting values of stabilizer deflection where the differential incidence available decreases. The two systems are aerodynamically coupled in the sense that directional control also induces lateral moments, and vice versa. The effectiveness

of each type of control and the cross-coupling moments may be readily determined from the results of the preceding analyses.

Directional control.- The side force due to tip-control deflection may be estimated in a relatively simple manner by an extension of the methods of reference 16. The tip control and adjacent stabilizer-body combination may, as an approximation, be regarded as a wing and body combination, thereby permitting ready use of the charts of reference 16 for determination of the mutual interference effects due to incidence. This procedure leads to the expressions

$$\left.\begin{aligned}\left(C_{Y_{\delta_R}}\right)_L &= Q_L \frac{S_{R_l}}{S}\left(k_{R_lB} + k_{BR_l}\right)\left(C'N_\alpha\right)_{R_l} \\ \left(C_{Y_{\delta_R}}\right)_U &= Q_U \frac{S_{R_u}}{S}\left(k_{R_uB} + k_{BR_u}\right)\left(C'N_\alpha\right)_{R_u}\end{aligned}\right\} \tag{64}$$

in which the various k terms are analogous to the interference factors contained in equation (11) for the horizontal-stabilizer effectiveness. As discussed earlier, $\left(C'N_\alpha\right)_{R_u}$ and $\left(C'N_\alpha\right)_{R_l}$ may be determined from the results of linear theory in reference 22 corrected for the effects of the wedge-type profiles as recommended in reference 46. The dynamic-pressure terms Q_L and Q_U are given in figure 28. The corresponding yawing-moment coefficients are then found by multiplying equation (64) by the appropriate control moment arms $(\bar{x}/b)$.

Rolling moments due to tip-control deflections arise from differences both in geometry and in dynamic pressure Q at high angles of attack. Their magnitudes are proportional to the distances from the axis of rotation to the lateral centers of pressure which, in the present analysis, are assumed to be the centroids of the control-surface areas. It follows that

$$\left(C_{l_{\delta_R}}\right) = \left(C_{Y_{\delta_R}}\right)_L\left(\frac{\bar{z}_{R_l}}{b}\right) - \left(C_{Y_{\delta_R}}\right)_U\left(\frac{\bar{z}_{R_u}}{b}\right) \tag{65}$$

The directional-control derivatives predicted by equations (64) and (65) for the upper and lower surfaces acting both independently and in combination are presented in figures 46 and 47. Figure 46 shows again the relative influence of the previously described shock-expansion and compression fields from the wing on the relative effectiveness of the

[redacted]

two surfaces. The net results shown in figure 47 indicate a relatively high level of controllability for the anticipated flight profiles of the airplane, but also a substantial cross-coupling effect at high angles of attack.

The results of theory and experiment are compared in figure 48 in which generally fair agreement is indicated, although some improvement at the higher angles of attack and Mach numbers would be expected if the emersion of the lower control surface from the wing-body compression field were taken into account (see earlier discussion of dihedral effect).

Lateral control.- The lateral-control derivatives stem directly from the relationships developed for the pitch-control effectiveness. Referring to equation (15) and noting that each panel is deflected one-half of the total differential deflection, the following relationships are obtained

$$C_{l_{i'_T}} = \frac{1}{2} \frac{C_{L_{i_T}}}{\cos \Gamma_T} \frac{h}{b} \tag{66}$$

$$C_{Y_{i'_T}} = \frac{1}{2} \tan \Gamma_T C_{L_{i_T}} \tag{67}$$

$$C_{n_{i'_T}} = -\left(\frac{\bar{x}_T}{b}\right) C_{Y_{i'_T}} \tag{68}$$

The lateral centers of pressure are assumed to be located at the area centroids of the exposed panels, and the moment arm h is determined on this basis.

The calculated lateral-control derivatives are given in figure 49 which, as anticipated from the results of the earlier longitudinal-control analysis, shows an increasing degree of control effectiveness with increasing angle of attack. A noticeable cross-coupling effect is found also for this control. Figure 50 shows that in some cases theory and experiment for undetermined reasons do not agree well at high angles of attack.

CONCLUDING REMARKS

In the foregoing analytical study a number of available theoretical methods were employed for calculation of the longitudinal and lateral-directional stability and control derivatives for the X-15 airplane at

[redacted]

Mach numbers ranging from 2 to 12 and angles of attack as high as 25°. The analytical results were compared with existing wind-tunnel data for Mach numbers between 2 and 7, and thus enabled an overall assessment to be made of the accuracy and applicability of the methods used. The analysis as a whole provided valuable insights into the significance of the various shock-interference phenomena affecting the airplane as hypersonic speeds are approached, and to the relative importance of the individual airplane components in systematic buildups of the overall derivative characteristics. In addition, the analysis was extended to speeds well beyond the estimated limit for the X-15 so the derivatives for more advanced versions of this type vehicle could be examined.

In general, satisfactory agreement with wind-tunnel results was obtained. Notable exceptions, however, were found in the stabilizer effectiveness and several of the lateral-directional characteristics at high angles of attack where shock interference on the horizontal and vertical tails could not be readily calculated.

Particularly noteworthy for the X-15 configuration are the increases in longitudinal and directional static stability as angle of attack is increased at hypersonic speeds. These characteristics, however, are accompanied by an unstable trend in dihedral effect. Pronounced cross coupling of the directional- and lateral-control moments are also noted at high angles of attack and Mach numbers. In general, the calculations indicate that both stability and controllability are maintained well beyond the estimated limit speed.

The limiting values predicted by Newtonian theory for the static derivatives are found in general to be lower than the trends shown by the unified supersonic-hypersonic small-disturbance theory, shock-expansion theory, and other methods employed in the analysis.

Flight Research Center,
National Aeronautics and Space Administration,
Edwards, Calif., March 1, 1960.

[redacted]

[redacted]

APPENDIX

LIST OF SYMBOLS

In the following list of symbols, the aerodynamic coefficients, when used without a superscript, are based on the dimensions of the wing with leading and trailing edges extended to the plane of symmetry of the airplane, and, when primed, on the dimensions of the isolated surface or body.

A_α — plan-form area of fuselage forebody from vertex to wing leading edges

A_φ — projected area of fuselage on plane normal to crossflow at combined α and β for portions of fuselage affected by crossflow

b — overall span (refers to wing without subscript)

C_D — drag coefficient, $\frac{\text{Drag}}{\bar{q}_\infty S}$

C_L — lift coefficient, $\frac{\text{Lift}}{\bar{q}_\infty S}$

$C_{L_{i_T}} = \frac{\partial C_L}{\partial i_T}$

$C_{L_\alpha} = \frac{\partial C_L}{\partial \alpha}$

$\left(C_{L_\alpha}\right)_l$ — lift-curve slope in downstream flow based on local Mach number

$\left(C_{L_\alpha}\right)_\infty$ — lift-curve slope in free-stream flow

C_l — rolling-moment coefficient, $\frac{\text{Rolling moment}}{\bar{q}_\infty S b}$

$C_{l_{i'_T}} = \frac{\partial C_l}{\partial i'_T}$

[redacted]

$$C_{l_p} = \frac{\partial C_l}{\partial\left(\frac{pb}{2V}\right)}$$

$$C_{l_r} = \frac{\partial C_l}{\partial\left(\frac{rb}{2V}\right)}$$

$$C_{l_\beta} = \frac{\partial C_l}{\partial \beta}$$

$$C_{l_{\dot{\beta}}} = \frac{\partial C_l}{\partial\left(\frac{\dot{\beta}b}{2V}\right)}$$

$$C_{l_{\delta_R}} = \frac{\partial C_l}{\partial \delta_R}$$

C_m pitching-moment coefficient, $\frac{\text{Pitching moment}}{\bar{q}_\infty S\bar{c}}$

$$C_{m_{C_L}} = \frac{C_{m_\alpha}}{C_{L_\alpha}}$$

$$C_{m_{i_T}} = \frac{\partial C_m}{\partial i_T}$$

$$C_{m_q} = \frac{\partial C_m}{\partial\left(\frac{q\bar{c}}{2V}\right)}$$

$$C_{m_\alpha} = \frac{\partial C_m}{\partial \alpha}$$

$$C_{m_{\dot{\alpha}}} = \frac{\partial C_m}{\partial\left(\frac{\dot{\alpha}\bar{c}}{2V}\right)}$$

[redacted]

C'_N normal-force coefficient, $\frac{\text{Normal force}}{\bar{q}_\infty S}$

$C_{N_\alpha} = \frac{\partial C_N}{\partial \alpha}$

C_n yawing-moment coefficient, $\frac{\text{Yawing moment}}{\bar{q}_\infty Sb}$

$C_{n_{i'_T}} = \frac{\partial C_n}{\partial i'_T}$

$C_{n_p} = \frac{\partial C_n}{\partial \left(\frac{pb}{2V}\right)}$

$C_{n_r} = \frac{\partial C_n}{\partial \left(\frac{rb}{2V}\right)}$

$C_{n_\beta} = \frac{\partial C_n}{\partial \beta}$

$C_{n_\beta}{}^*$ effective directional-stability parameter (eq. (49))

$C_{n_{\dot{\beta}}} = \frac{\partial C_y}{\partial \left(\frac{\dot{\beta}b}{2V}\right)}$

$C_{n_{\delta_R}} = \frac{\partial C_n}{\partial \delta_R}$

c_n normal-force coefficient for two-dimensional flat plate

$c_{n_\alpha} = \frac{\partial c_n}{\partial \alpha}$

C_p pressure coefficient,
$\frac{\text{Local pressure - Free-stream static pressure}}{\bar{q}_\infty}$

[redacted]

H
1
4
6

C_Y side-force coefficient, $\frac{\text{Side force}}{\bar{q}_\infty S}$

$C_{Y_{i'_T}} = \frac{\partial C_Y}{\partial i'_T}$

$C_{Y_p} = \frac{\partial C_Y}{\partial\left(\frac{pb}{2V}\right)}$

$C_{Y_r} = \frac{\partial C_Y}{\partial\left(\frac{rb}{2V}\right)}$

$C_{Y_\beta} = \frac{\partial C_Y}{\partial \beta}$

$C_{Y_{\dot{\beta}}} = \frac{\partial C_Y}{\partial\left(\frac{\dot{\beta}b}{2V}\right)}$

$C_{Y_{\delta_R}} = \frac{\partial C_Y}{\partial \delta_R}$

H 1 4 6

$\bar{c}$ mean aerodynamic chord (refers to reference area S when used without subscript)

$\bar{c}_{d_c}$ average crossflow drag coefficient for fuselage as calculated by method of reference 31

H similarity parameter, $\left(M^2 - 1\right)^{1/2}\alpha$

H' $\frac{\gamma + 1}{4}\left(M^2 - 1\right)^{1/2}\alpha$ or $\frac{\gamma + 1}{4}$ H

h moment arm from fuselage center line to center of pressure of horizontal tail measured in plane of tail

I_X moment of inertia about X-axis, slug-ft^2 (fig. 4(b))

[redacted]

I_Z moment of inertia about Z-axis, slug-ft^2 (fig. 4(b))

i angle of incidence

i_T incidence of horizontal tail measured in plane of symmetry relative to fuselage center line, positive for upward rotation of leading edge

i'_T differential incidence of horizontal-tail panels

K ratio of lift due to angle of attack of a component in presence of an adjacent component to lift of isolated wing or tail surface (see ref. 16 and subscripts)

K_φ factor representing coupling of sidewash velocities due to α and β (see ref. 44)

k ratio of lift due to angle of incidence of a component in presence of an adjacent component to lift of isolated wing or tail surface

L overall length of fuselage

M Mach number

p rate of roll

$$Q = \frac{\bar{q}_1 \left(C_{L_\alpha}\right)_1}{\bar{q}_\infty \left(C_{L_\alpha}\right)_\infty}$$

q pitching rate

$\bar{q}_\infty$ free-stream dynamic pressure, $\frac{1}{2}\rho_\infty V_\infty^2$

$\bar{q}_1$ dynamic pressure of downstream flow where local static pressure behind the bow shock wave is equal to free-stream static pressure

R_α ratio of total fuselage plan-form area to plan-form area of equivalent body of revolution having same local cross-sectional areas (see eq. (6))

R_φ	ratio of projected area of fuselage on plane normal to fuselage crossflow at combined α and β to area of equivalent body of revolution having the same local cross-sectional area (see eq. (31))
r	rate of yaw
S	reference area equal to area of wing with leading and trailing edges extended to plane of symmetry
S_{AB}	plan form and side area of fuselage afterbody for normal- and side-force considerations, respectively (see Newtonian theory, eqs. (8) and (37))
S_B	fuselage frontal area
S_{NC}	base area of nose cone approximating fuselage nose section (see Newtonian method, eq. (8))
S_R	area of directional-control surface
S_T	area of exposed horizontal-tail surfaces
S'_T	area of horizontal tail with leading and trailing edges extended to fuselage center line
S_W	area of exposed wing panels
V	local-stream velocity
V_∞	free-stream velocity
v	side velocity
w	vertical velocity
X,Y,Z	coordinate axes (see fig. 4)
$\bar{x}$	longitudinal distance from center of gravity to center of pressure of component lift measured in direction of fuselage center line
x_c	longitudinal distance from vertex to centroid of area of fuselage measured in direction of fuselage center line

[redacted]

x_o longitudinal distance from vertex of fuselage to center of gravity measured in direction of fuselage center line

$\bar{y}$ lateral distance from fuselage center line to center of pressure

$\bar{z}$ vertical distance from fuselage center line to center of pressure

α angle of attack, deg

$\dot{\alpha}$ time rate of change of angle of attack due to constant vertical acceleration (plunging motion)

α_e effective angle of attack of horizontal tail at combined α and β (see eq. (39)), deg

β angle of sideslip, deg

$\dot{\beta}$ time rate of change of sideslip angle due to constant lateral acceleration

Γ_T dihedral angle of horizontal tail measured from X-Y plane, positive when rotated upward

γ ratio of specific heat at constant pressure to specific heat at constant volume

δ_R deflection angle of directional-control surfaces, positive for rotation of leading edge to right, deg

ϵ downwash angle at tail, deg

$\bar{\epsilon}$ semiapex angle of wing or tail surface, deg

η ratio of drag coefficient of a circular cylinder of finite length to that for cylinder of infinite length (see ref. 30)

θ_q potential function for constant rate of pitch (see ref. 39)

λ_T taper ratio of horizontal-tail panels, $\frac{\text{Tip chord}}{\text{Root chord}}$

μ angle between plane containing velocity vector and fuselage center line and the normal to the plane of symmetry at combined α and β (see eqs. (31) and (32))

[redacted]

H 1 4 6

ν	angle of inclination of fuselage side fairings (see Newtonian method, eq. (8))
ρ_∞	free-stream density, slugs/cu ft
σ	sidewash angle at tail, deg
τ_{NC}	semivertex angle of nose cone (see Newtonian method eq. (8))
τ_v	semivertex angle of vertical-tail wedge sections (see fig. 1)
φ	angle between free-stream velocity and fuselage center line at combined α and β
Ω_α	potential function for constant angle of attack (see ref. 39)
$\overline{\frac{\partial}{\partial z}\left(\frac{\theta_q}{q\bar{c}_w}\right)}$	average upwash at tail due to steady pitching rate of wing (see ref. 39)
$\overline{\frac{\partial}{\partial z}\left(\frac{\Omega_\alpha}{\alpha V}\right)}$	average upwash at tail due to steady plunging motion of wing (see ref. 39)

Subscripts:

av	average
B	fuselage
BL	fuselage in presence of lower vertical tail
BR_l	fuselage in presence of lower directional-control panel
BR_u	fuselage in presence of upper directional-control panel
BT	fuselage in presence of horizontal tail
BU	fuselage in presence of upper vertical tail
BW	fuselage in presence of wing
L	lower vertical tail (exposed)

[redacted]

[redacted]

LB	lower vertical tail in presence of fuselage
P	designates that angle is measured in plane perpendicular to the plane of the horizontal tail
R_l	lower directional-control panel
R_lB	lower directional-control panel in presence of fuselage
R_u	upper directional-control panel
R_uB	upper directional-control panel in presence of fuselage
T	horizontal tail (exposed)
TB	horizontal tail in presence of fuselage
U	upper vertical tail (exposed)
BU	upper vertical tail in presence of fuselage
W	wing (exposed)
WB	wing in presence of fuselage
α	quantity due to angle of attack or sideslip (ref. 44)
φ	quantity due to combined angles of attack and sideslip (ref. 44)

H
1
4
6

[redacted]

REFERENCES

1. Driver, Cornelius: Effect of Forebody Strakes on the Aerodynamic Characteristics in Pitch and Sideslip of a Hypersonic Airplane Configuration at Mach Numbers of 1.41, 2.01, and 6.86. NASA TM X-116, 1959.

2. Tunnell, Phillips J., and Latham, Eldon A.: The Static and Dynamic-Rotary Stability Derivatives of a Model of the X-15 Research Airplane at Mach Numbers From 1.55 to 3.50. NASA MEMO 12-23-58A, 1959.

3. Franklin, Arthur E., and Lust, Robert M.: Investigation of the Aerodynamic Characteristics of a 0.067-Scale Model of the X-15 Airplane (Configuration 3) at Mach Numbers of 2.29, 2.98, and 4.65. NASA TM X-38, 1959.

4. Penland, Jim A., and Fetterman, David E., Jr.: Static Longitudinal, Directional, and Lateral Stability and Control Data at a Mach Number of 6.83 of the Final Configuration of the X-15 Research Airplane. NASA TM X-236, 1960.

5. Dryer, Murray, and North, Warren J.: Preliminary Analysis of the Effect of Flow Separation Due to Rocket Jet Pluming on Aircraft Dynamic Stability During Atmospheric Exit. NASA MEMO 4-22-59E, 1959.

6. Wolowicz, Chester H., and Rediess, Herman A.: Effects of Jet Exhausts on Flight-Determined Longitudinal and Lateral Dynamic Stability Characteristics of the Douglas D-558-II Research Airplane. NACA RM H57G09, 1957.

7. Love, Eugene S.: Supersonic Wave Interference Affecting Stability. NACA TN 4358, 1958.

8. Ulmann, Edward F., and Ridyard, Herbert W.: Flow-Field Effects on Static Stability and Control at High Supersonic Mach Numbers. NACA RM L55L19a, 1956.

9. Margolis, Kenneth, and Bobbitt, Percy J.: Theoretical Calculations of the Stability Derivatives at Supersonic Speeds for a High-Speed Airplane Configuration. NACA RM L53G17, 1953.

10. Nielsen, Jack N.: The Effects of Body Vortices and the Wing Shock-Expansion Field on the Pitch-Up Characteristics of Supersonic Airplanes. NACA RM A57L23, 1958.

[redacted]

11. Nielsen, Jack N., and Kaattari, George E.: The Effects of Vortex and Shock-Expansion Fields on Pitch and Yaw Instabilities of Supersonic Airplanes. Preprint No. 743, Inst. Aero. Sci., 1957.

12. Ames Research Staff: Equations, Tables, and Charts for Compressible Flow. NACA Rep. 1135, 1953. (Supersedes NACA TN 1428.)

13. Dugan, Duane W.: Estimation of Static Longitudinal Stability of Aircraft Configurations at High Mach Numbers and at Angles of Attack Between 0° and ±180°. NASA MEMO 1-17-59A, 1959.

14. Kaattari, George E.: Estimation of Directional Stability Derivatives at Moderate Angles and Supersonic Speeds. NASA MEMO 12-1-58A, 1959.

15. Jorgensen, Leland H., and Perkins, Edward W.: Investigation of Some Wake Vortex Characteristics of an Inclined Ogive-Cylinder Body at Mach Number 2. NACA Rep. 1371, 1958. (Supersedes NACA RM A55E31.)

16. Pitts, William C., Neilsen, Jack N., and Kaattari, George E.: Lift and Center of Pressure of Wing-Body-Tail Combinations at Subsonic, Transonic, and Supersonic Speeds. NACA Rep. 1307, 1957.

17. Spahr, J. Richard: Longitudinal Aerodynamic Characteristics to Large Angles of Attack of a Cruciform Missile Configuration at a Mach Number of 2. NACA RM A54H27, 1954.

18. Van Dyke, Milton D.: A Study of Hypersonic Small-Disturbance Theory. NACA Rep. 1194, 1954. (Supersedes NACA TN 3173.)

19. Ivey, H. Reese, and Cline, Charles W.: Effect of Heat-Capacity Lag on the Flow Through Oblique Shock Waves. NACA TN 2196, 1950.

20. Shapiro, Ascher H.: The Dynamics and Thermodynamics of Compressible Fluid Flow. Vol. II. The Ronald Press Co., 1954.

21. Raymond, Joseph L.: Thin Airfoils in Hypersonic Flow With Strong Shocks. Rep. P-1189, the RAND Corp., Dec. 19, 1957.

22. Harmon, Sidney M., and Jeffreys, Isabella: Theoretical Lift and Damping in Roll of Thin Wings With Arbitrary Sweep and Taper at Supersonic Speeds. Supersonic Leading and Trailing Edges. NACA TN 2114, 1950.

23. Purser, Paul E., and Campbell, John P.: Experimental Verification of a Simplified Vee-Tail Theory and Analysis of Available Data on Complete Models With Vee Tails. NACA Rep. 823, 1945.

24. Haefeli, Rudolph C., Mirels, Harold, and Cummings, John L.: Charts for Estimating Downwash Behind Rectangular, Trapezoidal, and Triangular Wings at Supersonic Speeds. NACA TN 2141, 1950.

25. Allen, H. Julian, and Perkins, Edward W.: A Study of Effects of Viscosity on Flow Over Slender Inclined Bodies of Revolution. NACA Rep. 1048, 1951.

26. Syvertson, Clarence A., and Dennis, David H.: A Second-Order Shock-Expansion Method Applicable to Bodies of Revolution Near Zero Lift. NACA Rep. 1328, 1957. (Supersedes NACA TN 3527.)

27. Eggers, A. J., Jr., and Savin, Raymond C.: A Unified Two-Dimensional Approach to the Calculation of Three-Dimensional Hypersonic Flows, With Application to Bodies of Revolution. NACA Rep. 1249, 1955. (Supersedes NACA TN 2811.)

28. Jorgensen, Leland H.: Elliptic Cones Alone and With Wings at Supersonic Speeds. NACA Rep. 1376, 1958. (Supersedes NACA TN 4045.)

29. Jorgensen, Leland H.: Inclined Bodies of Various Cross Sections at Supersonic Speeds. NASA MEMO 10-3-58A, 1958.

30. Allen, H. Julian: Estimation of the Forces and Moments Acting on Inclined Bodies of Revolution of High Fineness Ratio. NACA RM A9I26, 1949.

31. Perkins, Edward W., and Jorgensen, Leland H.: Comparison of Experimental and Theoretical Normal-Force Distributions (Including Reynolds Number Effects) on an Ogive-Cylinder Body at Mach Number 1.98. NACA TN 3716, 1956.

32. Delany, Noel K., and Sorensen, Norman E.: Low-Speed Drag of Cylinders of Various Shapes. NACA TN 3038, 1953.

33. Gowen, Forrest E., and Perkins, Edward W.: Drag of Circular Cylinders for a Wide Range of Reynolds Numbers and Mach Numbers. NACA TN 2960, 1953.

34. Carlson, Harry W., and Gapcynski, John P.: An Experimental Investigation at a Mach Number of 2.01 of the Effects of Body Cross-Section Shape on the Aerodynamic Characteristics of Bodies and Wing-Body Combinations. NACA RM L55E23, 1955.

35. Martin, John C., Margolis, Kenneth, and Jeffreys, Isabella: Calculation of Lift and Pitching Moments Due to Angle of Attack and Steady Pitching Velocity at Supersonic Speeds for Thin Sweptback Tapered Wings With Streamwise Tips and Supersonic Leading and Trailing Edges. NACA TN 2699, 1952.

[redacted]

36. Harmon, Sidney M.: Stability Derivatives at Supersonic Speeds of Thin Rectangular Wings With Diagonals Ahead of Tip Mach Lines. NACA Rep. 925, 1949. (Supersedes NACA TN 1706.)

37. Henderson, Arthur, Jr.: Pitching-Moment Derivatives C_{m_q} and $C_{m_{\dot{\alpha}}}$ at Supersonic Speeds for a Slender-Delta-Wing and Slender-Body Combination and Approximate Solutions for Broad-Delta-Wing and Slender-Body Combinations. NACA TN 2553, 1951.

38. Tobak, Murray, Reese, David E., and Beam, Benjamin H.: Experimental Damping in Pitch of 45° Triangular Wings. NACA RM A50J26, 1950.

39. Martin, John C., Diederich, Margaret S., and Bobbitt, Percy J.: A Theoretical Investigation of the Aerodynamics of Wing-Tail Combinations Performing Time-Dependent Motions at Supersonic Speeds. NACA TN 3072, 1954.

40. Goodwin, Frederick K., and Kaattari, George E.: Estimation of Directional Stability Derivatives at Small Angles and Subsonic and Supersonic Speeds. NASA MEMO 12-2-58A, 1958.

41. Spahr, J. Richard, and Polhamus, Edward C.: Aerodynamic Loads on Tails at High Angles of Attack and Sideslip. NACA RM A57E21, 1957.

42. Jones, Arthur L., and Alksne, Alberta: A Summary of Lateral-Stability Derivatives Calculated for Wing Plan Forms in Supersonic Flow. NACA Rep. 1052, 1951.

43. Jones, Arthur L., Spreiter, John R., and Alksne, Alberta: The Rolling Moment Due to Sideslip of Triangular, Trapezoidal, and Related Plan Forms in Supersonic Flow. NACA TN 1700, 1948.

44. Spahr, J. Richard: Contribution of the Wing Panels to the Forces and Moments of Supersonic Wing-Body Combinations at Combined Angles. NACA TN 4146, 1958.

45. Boatright, William B.: Experimental Investigation of Effects of Wing Plan Form and Dihedral Angle on Sideslip Derivatives of Sweptback-Wing-Body Combinations at Supersonic Speeds. NACA RM L58E08, 1958.

46. McLellan, Charles H.: A Method for Increasing the Effectiveness of Stabilizing Surfaces at High Supersonic Mach Numbers. NACA RM L54F21, 1954.

H
1
4
6

[redacted]

47. Moul, Martin T., and Paulson, John W.: Dynamic Lateral Behavior of High-Performance Aircraft. NACA RM L58E16, 1958.

48. Pitts, William C.: Force, Moment, and Pressure-Distribution Characteristics of Rectangular Wings at High Angles of Attack and Supersonic Speeds. NACA RM A55K09, 1956.

49. Margolis, Kenneth, and Bobbitt, Percy J.: Theoretical Calculations of the Pressures, Forces, and Moments at Supersonic Speeds Due to Various Lateral Motions Acting on Thin Isolated Vertical Tails. NACA Rep. 1268, 1956.

50. Fisher, Lewis R., and Fletcher, Herman S.: Effect of Lag of Sidewash on the Vertical-Tail Contribution to Oscillatory Damping in Yaw of Airplane Models. NACA TN 3356, 1955.

51. Harmon, Sidney M., and Martin, John C.: Theoretical Calculations of the Lateral Force and Yawing Moment Due to Rolling at Supersonic Speeds for Sweptback Tapered Wings With Streamwise Tips. Supersonic Leading Edges. NACA TN 2156, 1950.

52. Adams, Gaynor J., and Dugan, Duane W.: Theoretical Damping in Roll and Rolling Moment Due to Differential Wing Incidence for Slender Cruciform Wings and Wing-Body Combinations. NACA Rep. 1088, 1952.

53. Tucker, Warren A., and Piland, Robert O.: Estimation of the Damping in Roll of Supersonic-Leading-Edge Wing-Body Combinations. NACA TN 2151, 1950.

54. Strass, H. Kurt, and Marley, Edward T.: Rolling Effectiveness of All-Movable Wings at Small Angles of Incidence at Mach Numbers From 0.6 to 1.6. NACA RM L51H03, 1951.

55. Purser, Paul E.: An Approximation to the Effect of Geometric Dihedral on the Rolling Moment Due to Sideslip for Wings at Transonic and Supersonic Speeds. NACA RM L52B01, 1952.

56. Bobbitt, Percy J.: Linearized Lifting-Surface and Lifting-Line Evaluations of Sidewash Behind Rolling Triangular Wings at Supersonic Speeds. NACA TN 3609, 1956.

[redacted]

TABLE I

AIRPLANE GEOMETRIC CHARACTERISTICS

Wing (extended to body center line):	
Area, sq ft	200
Aspect ratio	2.50
Taper ratio	0.20
Mean aerodynamic chord, in.	123.23
Sweep of leading edge, deg	36.75
Span, ft	22.36
Root chord, in.	178.89
Tip chord, in.	35.78
Dihedral angle, deg	0
Incidence angle, deg	0
Twist, deg	0
Airfoil section	NACA 66005 (modified)
Fuselage station for 20-percent mean aerodynamic chord, in.	339.19
Wing station for 20-percent mean aerodynamic chord, in.	52.17
Flap area, sq ft	15.48
Flap travel, deg	40
Wing (exposed):	
Area, sq ft	105
Aspect ratio	2.15
Taper ratio	0.27
Root chord, in.	131.95
Tip chord, in.	35.78
Horizontal tail (exposed):	
Area, sq ft	51.76
Aspect ratio	2.81
Taper ratio	0.21
Mean aerodynamic chord, in.	60.07
Sweep of quarter-chord line, deg	45
Span, overall, ft	17.64
Root chord, in.	84.27
Tip chord, in.	25.28
Dihedral angle, deg	-15
Airfoil section	NACA 66005 (modified)
Fuselage station for 50-percent horizontal-tail mean aerodynamic chord, in.	537.52
Span station for 50-percent horizontal-tail mean aerodynamic chord, from fuselage, in.	26.96
Tail arm, 20-percent wing mean aerodynamic chord to 50-percent horizontal-tail mean aerodynamic chord, in.	198.33
Incidence range, normal to plane of symmetry, deg -	
Pitch control	35 down, 15 up
Roll control	±7.5

[redacted]

[redacted]

H-140

TABLE I.- Concluded

AIRPLANE GEOMETRIC CHARACTERISTICS

Vertical tail (upper, exposed):	
Area, sq ft	40.8
Aspect ratio	1.03
Taper ratio	0.74
Mean aerodynamic chord, in.	107.5
Sweep of leading edge, deg	30
Span (exposed), in.	55
Root chord, in.	122.5
Tip chord, in.	90.75
Airfoil section	10° wedge
Fuselage station for 50-percent vertical-tail mean aerodynamic chord, in.	520.25
Span station for 50-percent vertical-tail mean aerodynamic chord, from fuselage, in.	26.15
Tail arm, 20-percent wing mean aerodynamic chord to 50-percent vertical-tail mean aerodynamic chord, in.	181.06
Movable area, outboard panel, sq ft	26.5
Angular travel of movable area, deg	±7.5
Vertical tail (lower, exposed):	
Area, sq ft	34.2
Aspect ratio	0.785
Taper ratio	0.79
Mean aerodynamic chord, in.	109.2
Sweep of leading edge, deg	30
Span, exposed, in.	44
Root chord, in.	121.4
Tip chord, in.	96
Airfoil section	10° wedge
Fuselage station for 50-percent vertical-tail mean aerodynamic chord, in.	519.4
Span station for 50-percent vertical-tail mean aerodynamic chord from fuselage, in.	21.15
Tail arm, 20-percent wing mean aerodynamic chord to 50-percent vertical-tail mean aerodynamic chord, in.	180.21
Movable (jettisonable) area, sq ft	19.9
Angular travel of movable area, deg	±7.5
Fuselage:	
Length, high-speed nose, ft	49.17
Length, low-speed nose, less boom, ft	50.16
Width, including side fairings, station 346 to station 411, in.	88.0
Height, station 186 to station 530, in.	56.0
Maximum cross-sectional area, sq ft	21.4
Fineness ratio, average	9.4
Nose apex angle, deg	31.0
Speed brakes (upper and lower):	
Location hinge line, fuselage station, in.	534
Side area, each, sq ft	4.88
Angular travel, fuselage center line, deg	41

[redacted]

TABLE II

SUMMARY OF WIND-TUNNEL TESTS

Facility	Model scale	Reynolds number, $R \times 10^{-6}$	M	α, deg	β, deg	Center of gravity, percent wing $\bar{c}$	Scope
Langley 4- by 4-foot supersonic pressure tunnel (ref. 1)	0.020	0.46 to 0.71	1.41, 2.01	0 to 24	0 to 20	20	C_L, C_m, C_D; C_n, C_l, C_Y. Effect of forebody strakes.
Langley Unitary Plan tunnel (ref. 3)	0.067	0.51 to 4.43	2.29, 2.98, 4.65	-10 to 20	-6 to 10	16	C_L, C_m, C_D; C_Y, C_n, C_l. Pitch, yaw, roll control effectiveness. Effect of speed brakes. Partial model buildup.
Langley 11-inch hypersonic tunnel (ref. 1)	0.020	0.64	6.86	-20 to 24	0 and -4.5	20	C_L, C_m, C_D; C_Y, C_n, C_l. Pitch, yaw, roll control effectiveness. Effect of speed brakes. Model buildup.
Ames Unitary Plan tunnel (ref. 2)	0.090	1.5	1.55, 2.0, 2.5, 3.0, 3.5	-6 to 14	0	25	C_{m_α}, $C_{m_q} + C_{m_{\dot{\alpha}}}$, $C_{n_r} - C_{n_{\dot{\beta}}}$, $C_{l_r} - C_{l_{\dot{\beta}}}$, $C_{n_p} + C_{n_{\dot{\beta}}} \sin \alpha$, $C_{l_p} + C_{l_{\dot{\beta}}} \sin \alpha$, C_{l_β}, C_{n_β}. Effect of speed brakes. Model buildup.
Langley 11-inch hypersonic tunnel (ref. 4)	0.020	0.64	6.83	-20 to 24	0 and -4.5	20	C_L, C_m, C_D, C_{Y_β}, C_{n_β}, C_{l_β}. Pitch, yaw, roll control effectiveness. Effect of speed brakes. Partial model buildup.

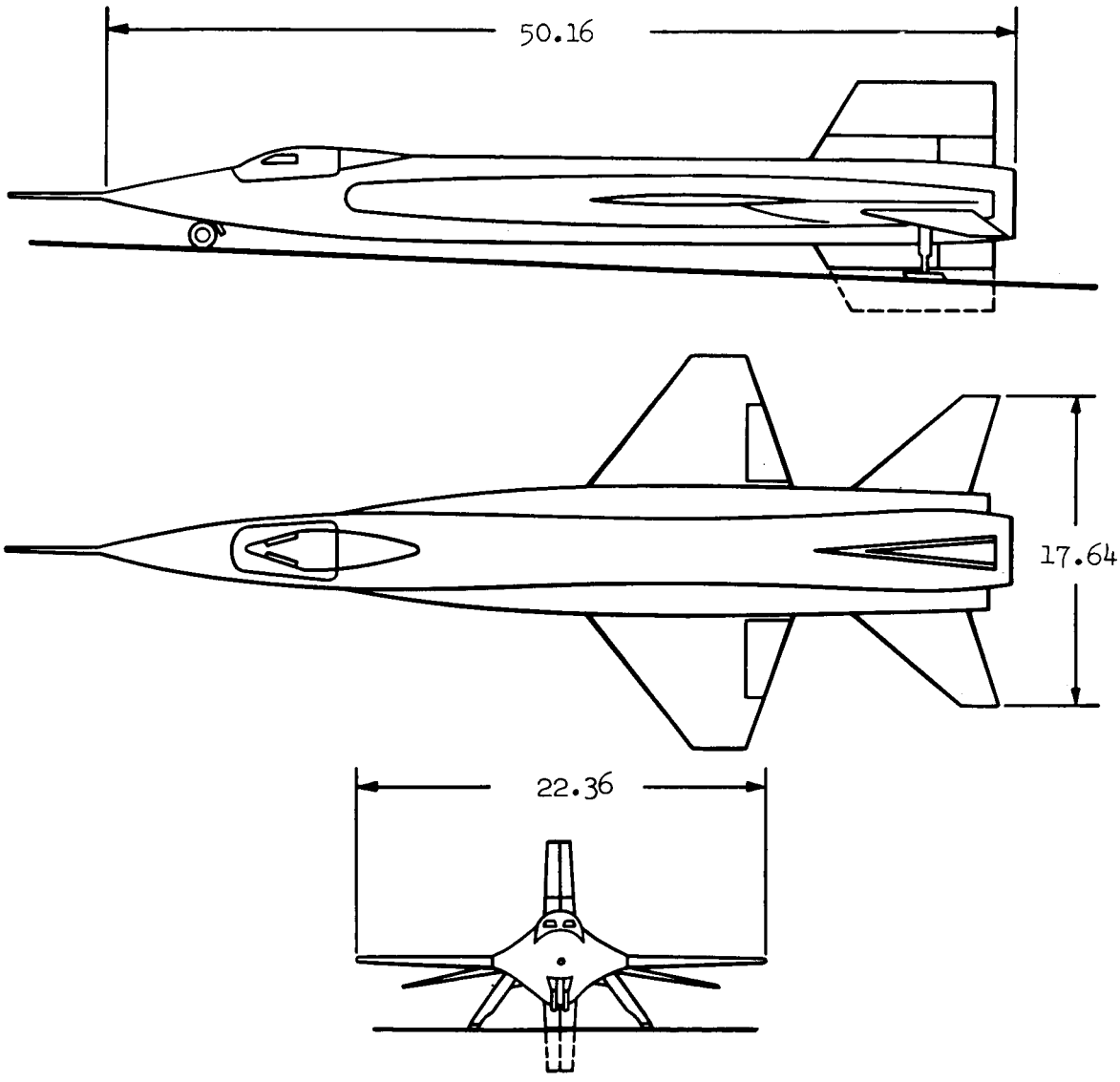

Figure 1.- Three-view drawing of the X-15 airplane. All dimensions in feet.

[redacted]

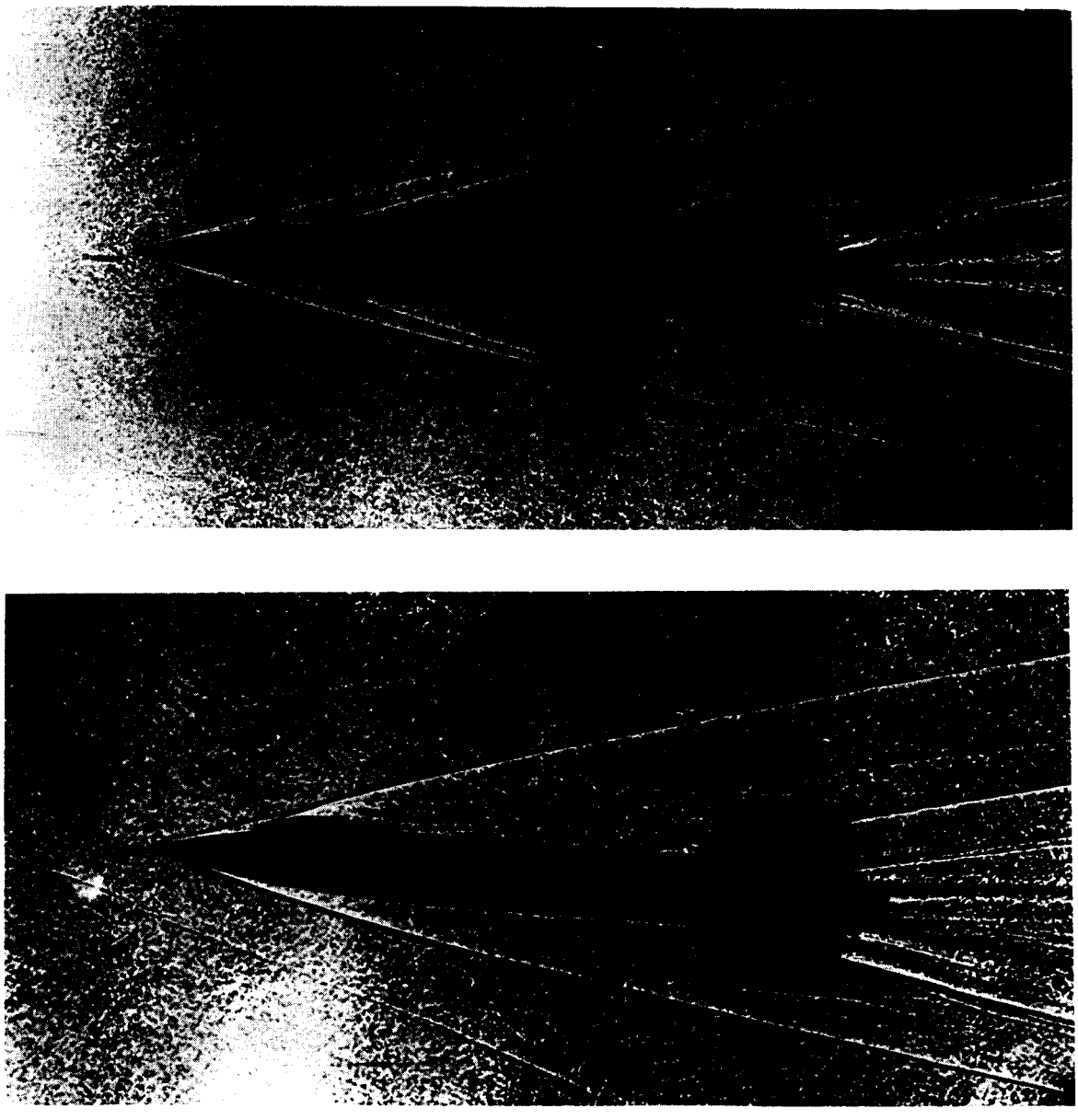

L-60-281

Figure 2.- Shadowgraphs of a free-flight model of the X-15 airplane at a Mach number of 6 taken in the Ames supersonic free-flight wind tunnel.

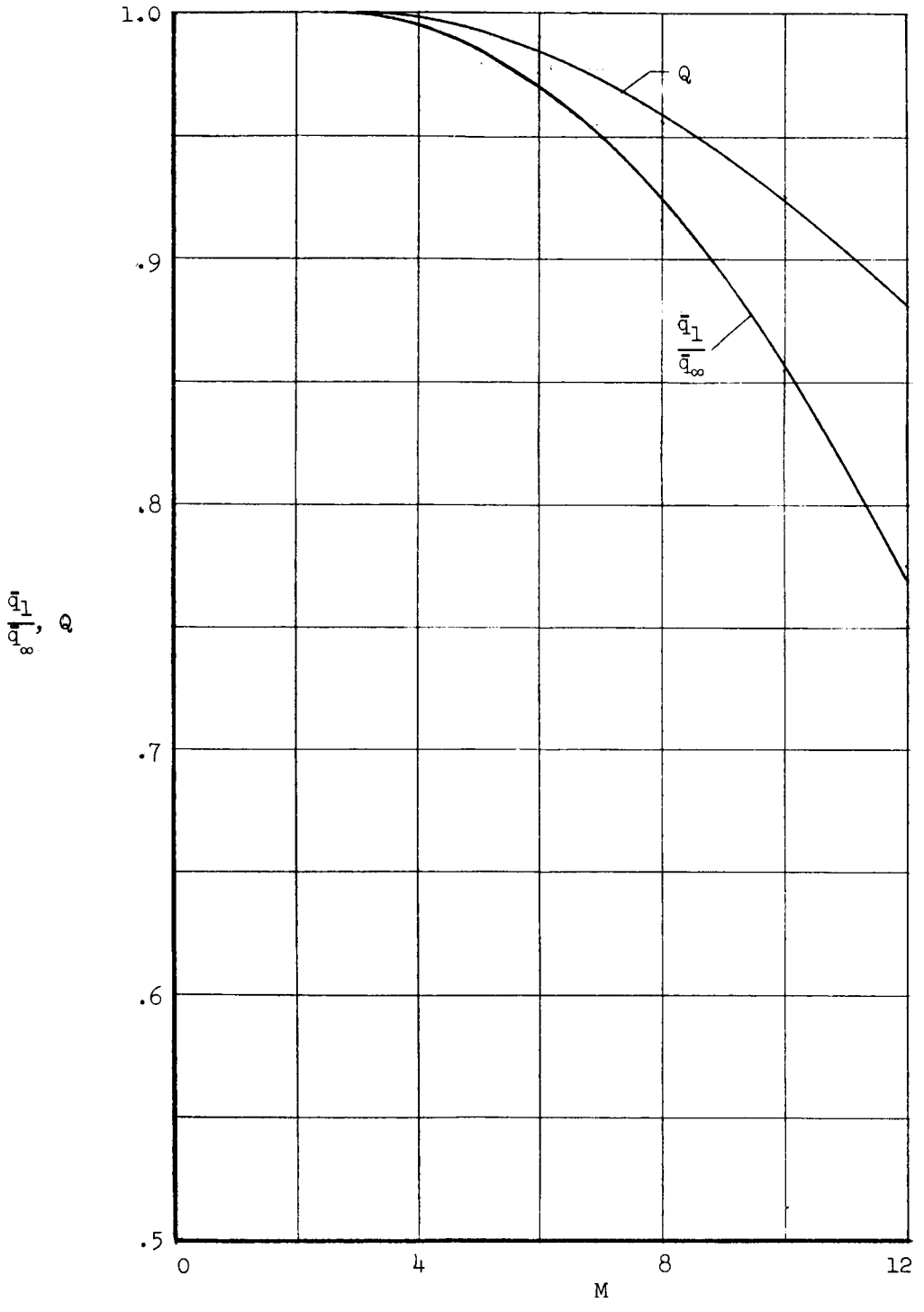

Figure 3.- Estimated losses in dynamic pressure and lift effectiveness for surfaces in the flow downstream from the fuselage bow-shock wave.

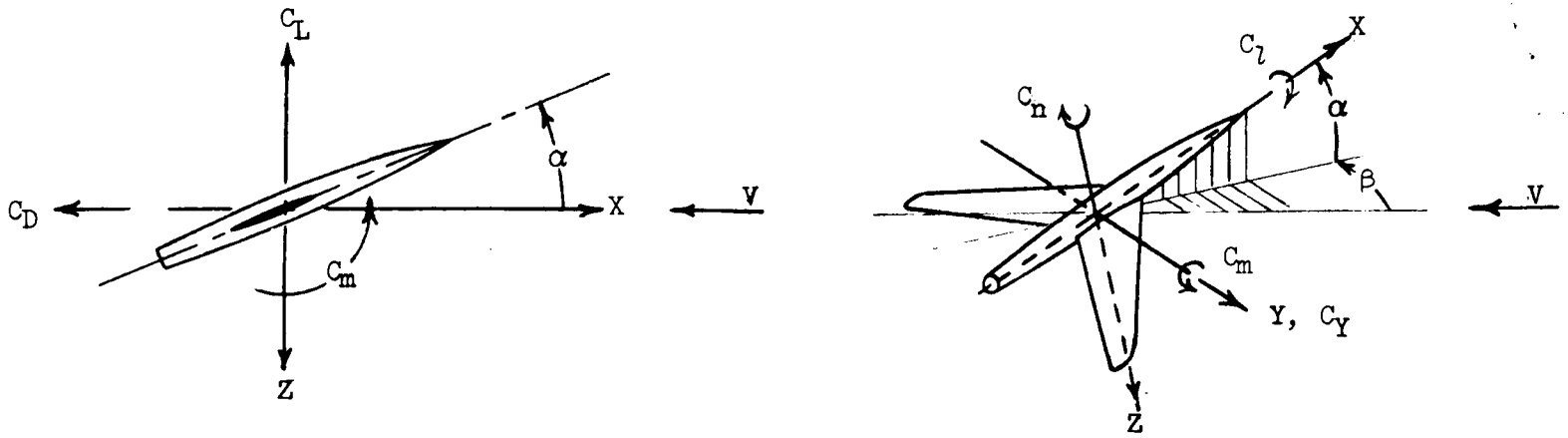

(a) Stability axes for longitudinal derivatives.

(b) Body axes for lateral-directional derivatives.

Figure 4.- Systems of axes. Positive values of direction, force, moments, and angles are indicated by arrows.

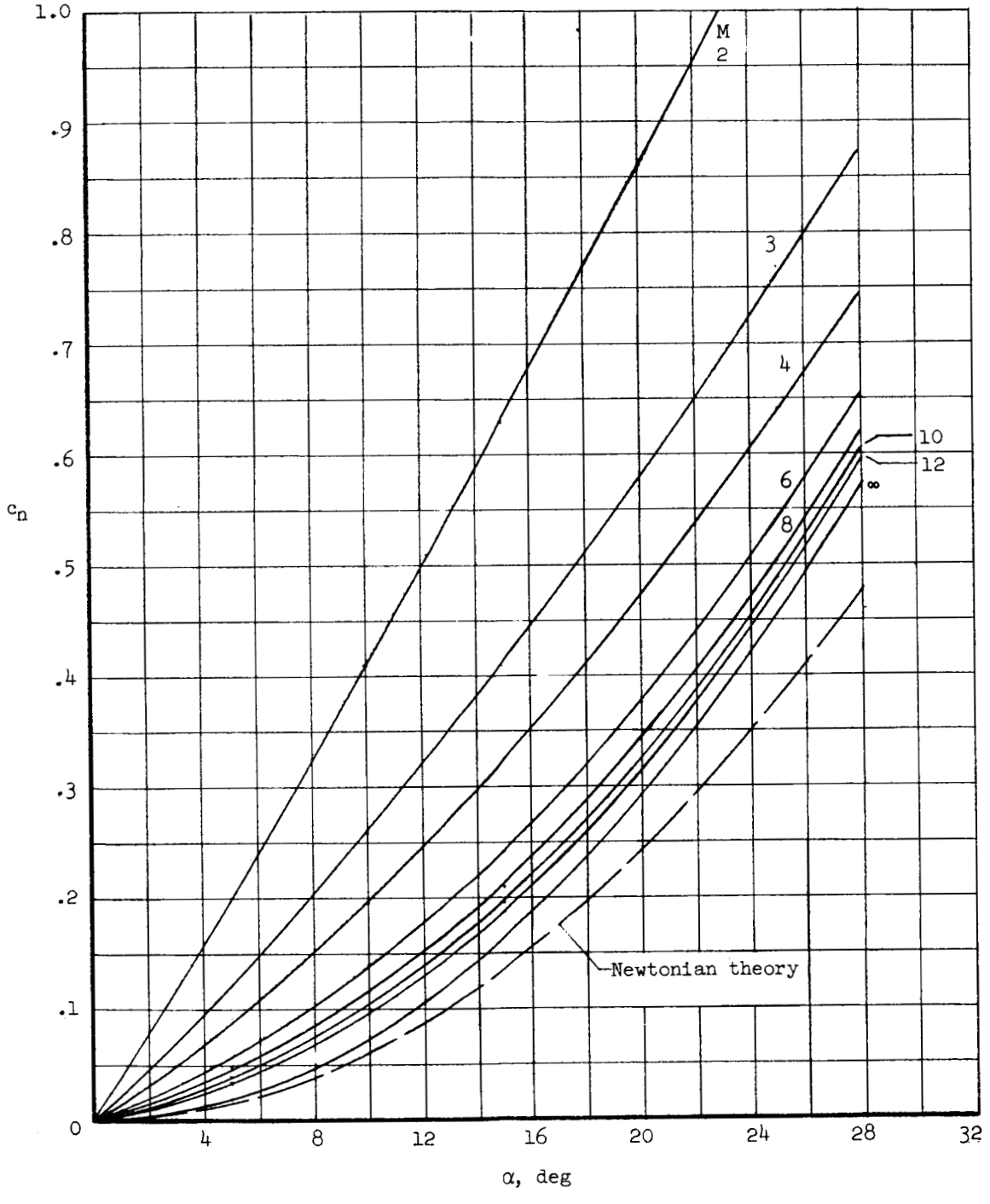

Figure 5.- Calculated normal-force curves for two-dimensional flat plate.

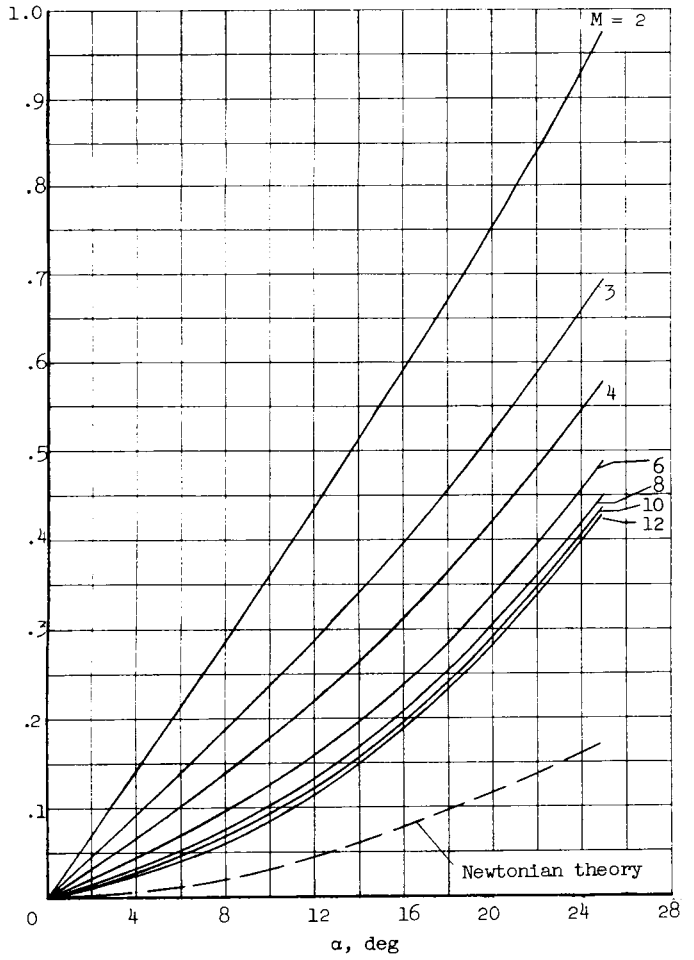

(a) Wing.

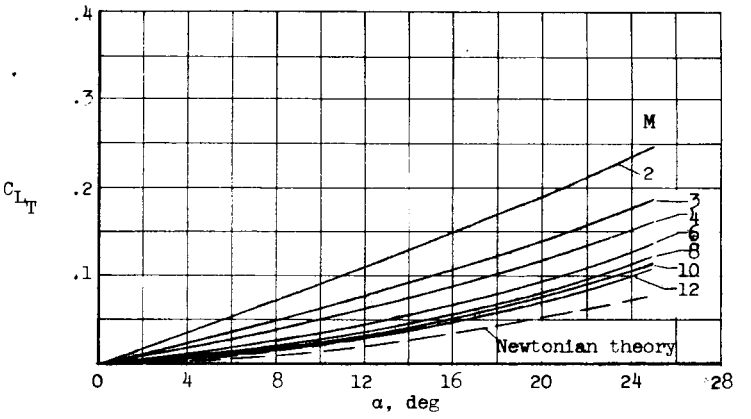

(b) Horizontal tail.

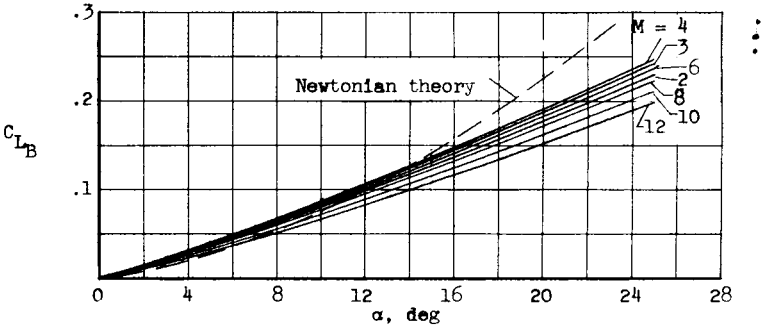

(c) Fuselage.

Figure 6.- Calculated lift curves for the wing, horizontal tail, and fuselage of the X-15 airplane.

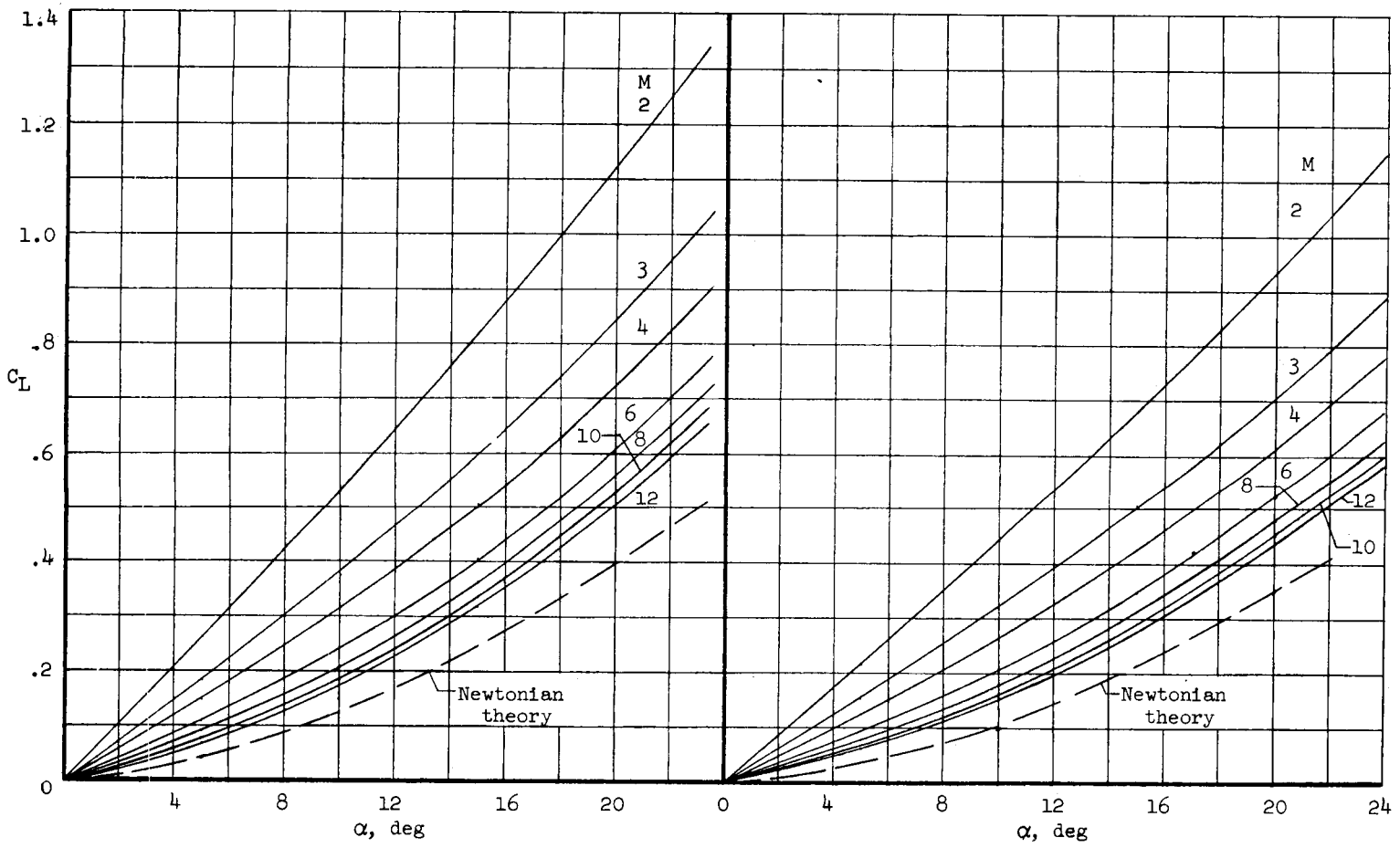

(a) Horizontal tail on.

(b) Horizontal tail off.

Figure 7.- Calculated lift curves for the X-15 airplane with the horizontal tail on and off.

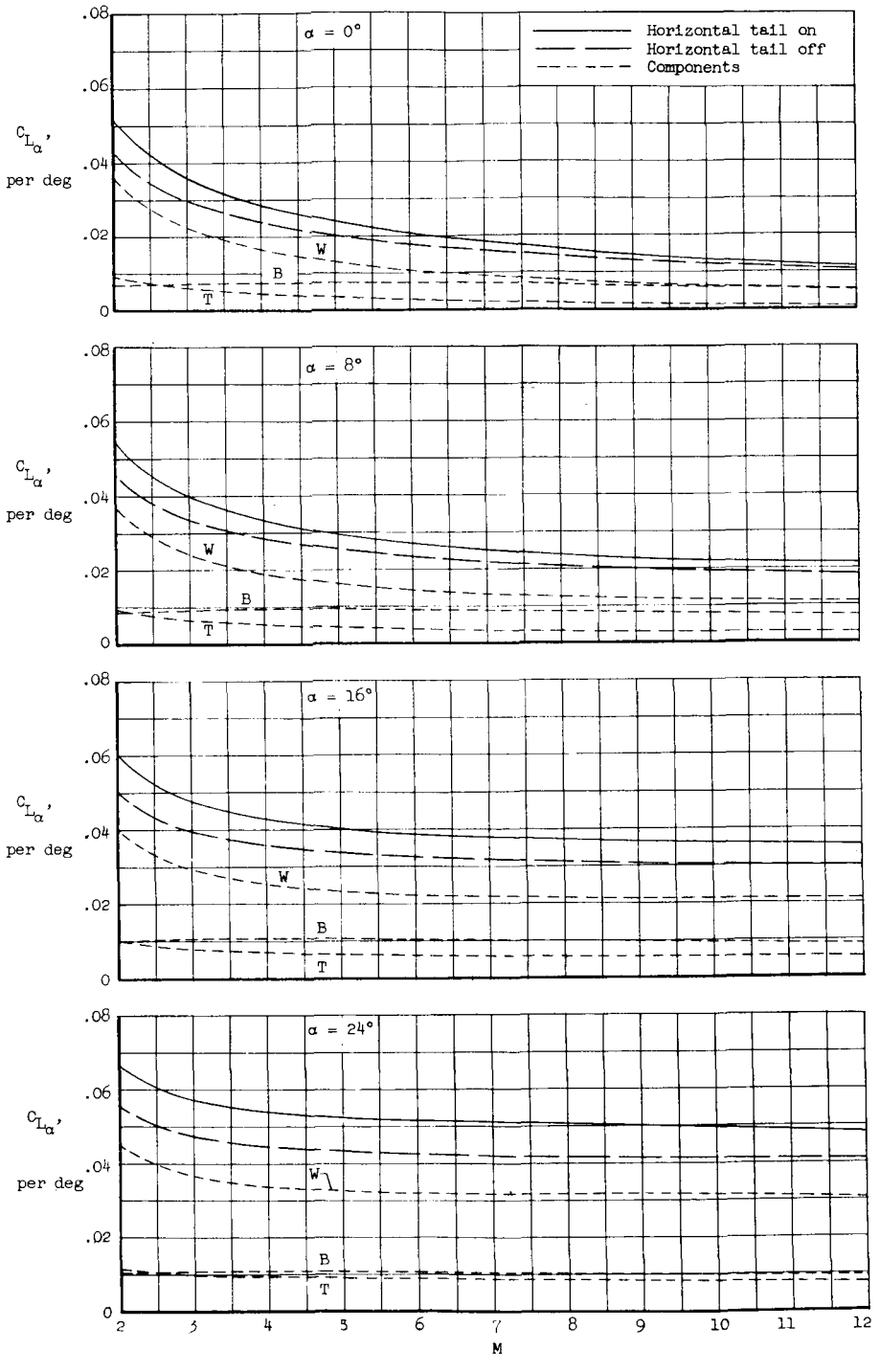

Figure 8.- Buildup of calculated lift curves for the X-15 airplane at angles of attack of 0°, 8°, 16°, and 24°. $i_T = 0°$.

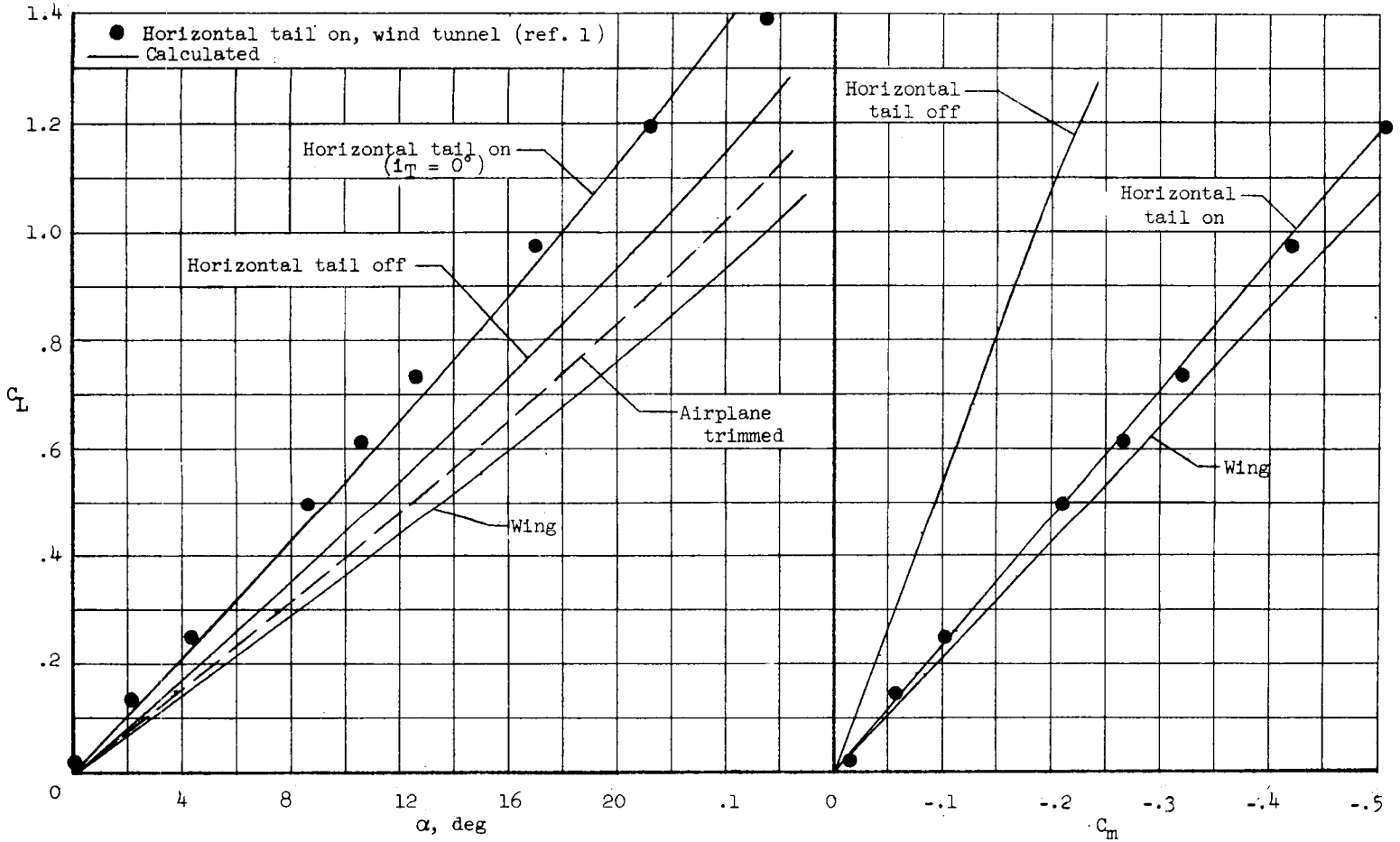

(a) M = 2.01.

Figure 9.- Comparison of calculated and experimental lift and pitching-moment characteristics for the X-15 airplane at various Mach numbers.

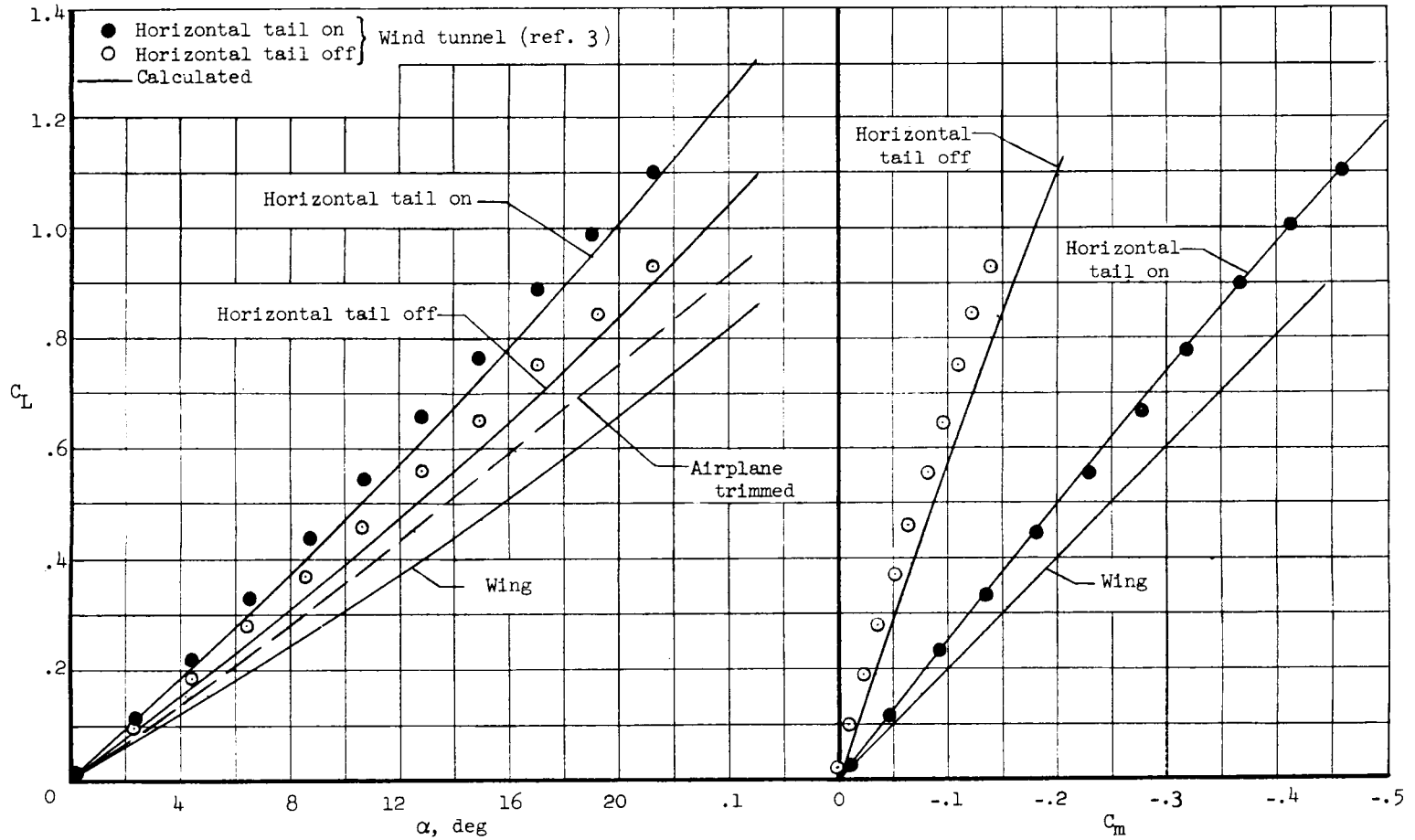

(b) M = 2.29.

Figure 9.- Continued.

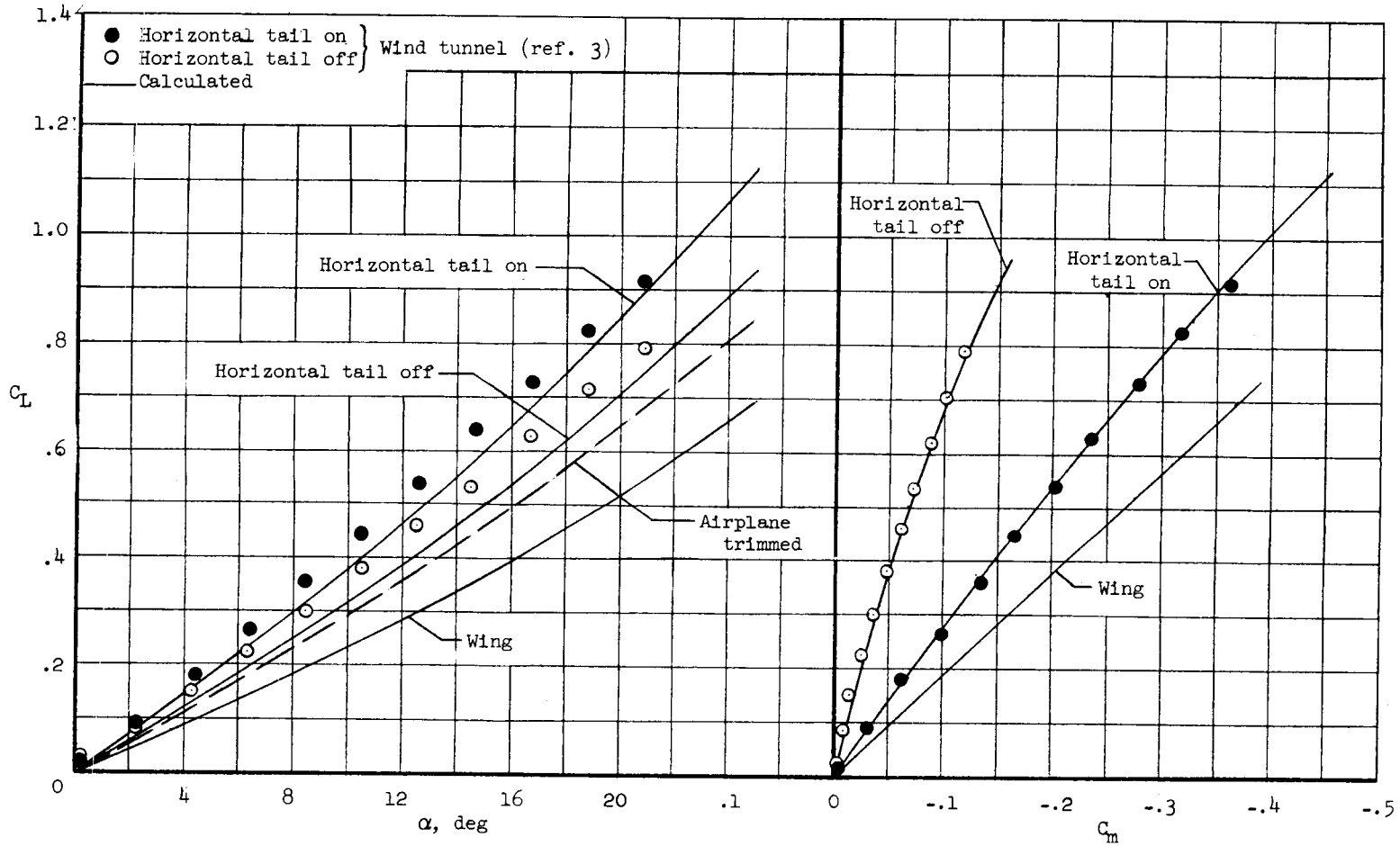

(c) M = 2.98.

Figure 9.- Continued.

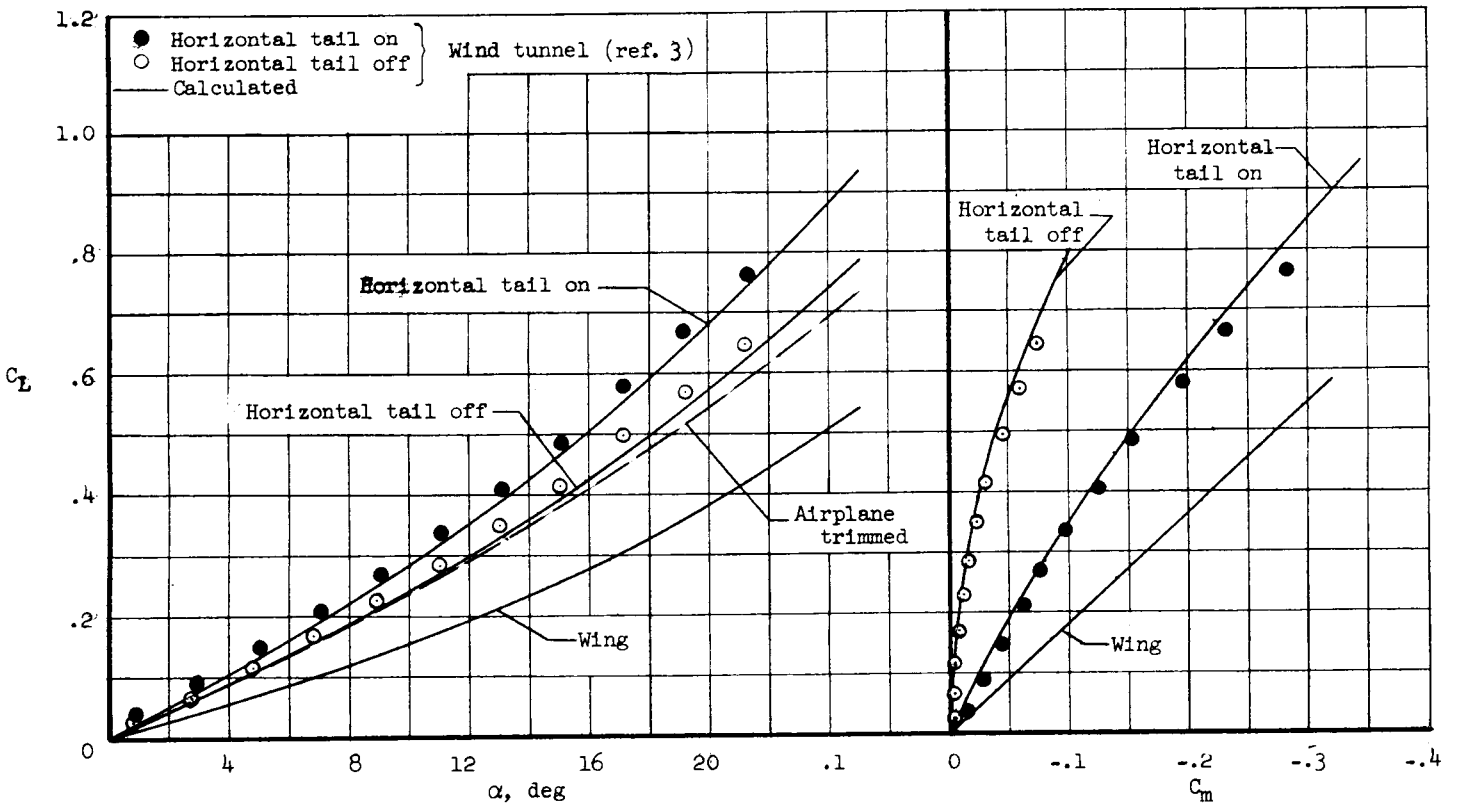

(d) M = 4.65.

Figure 9.- Continued.

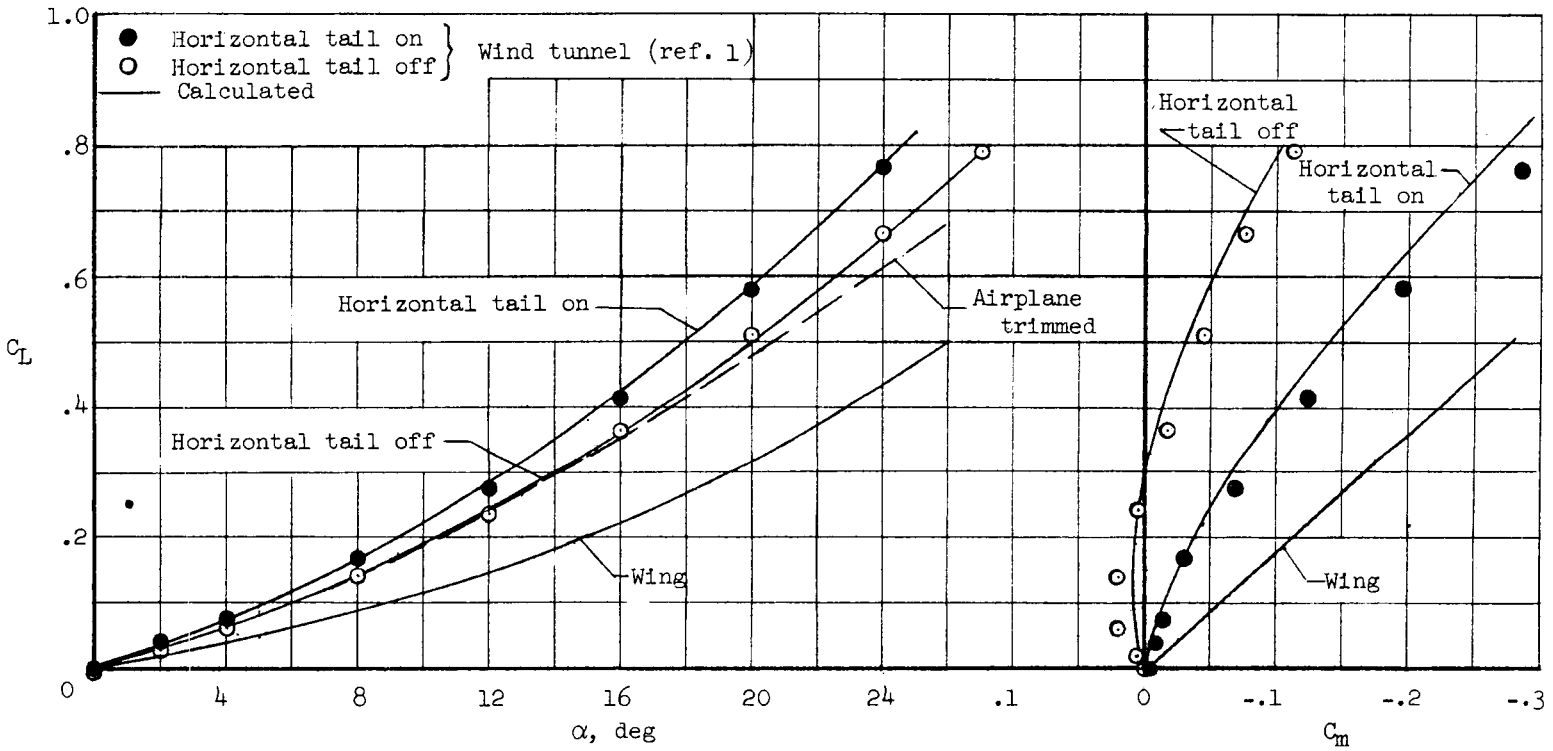

(e) M = 6.86.

Figure 9.- Concluded.

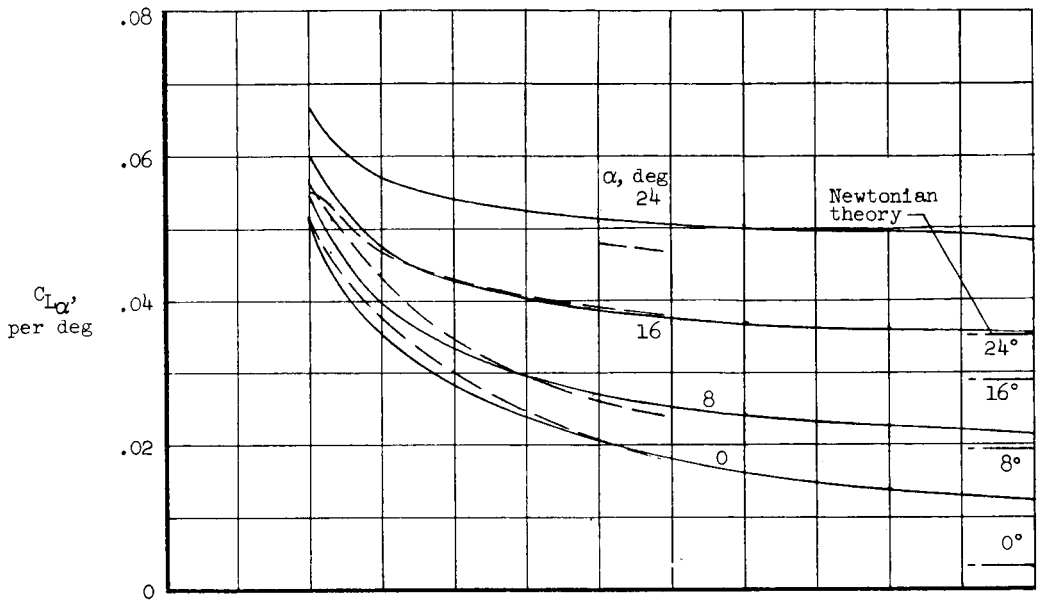

(a) Horizontal tail on. $i_T = 0^o$.

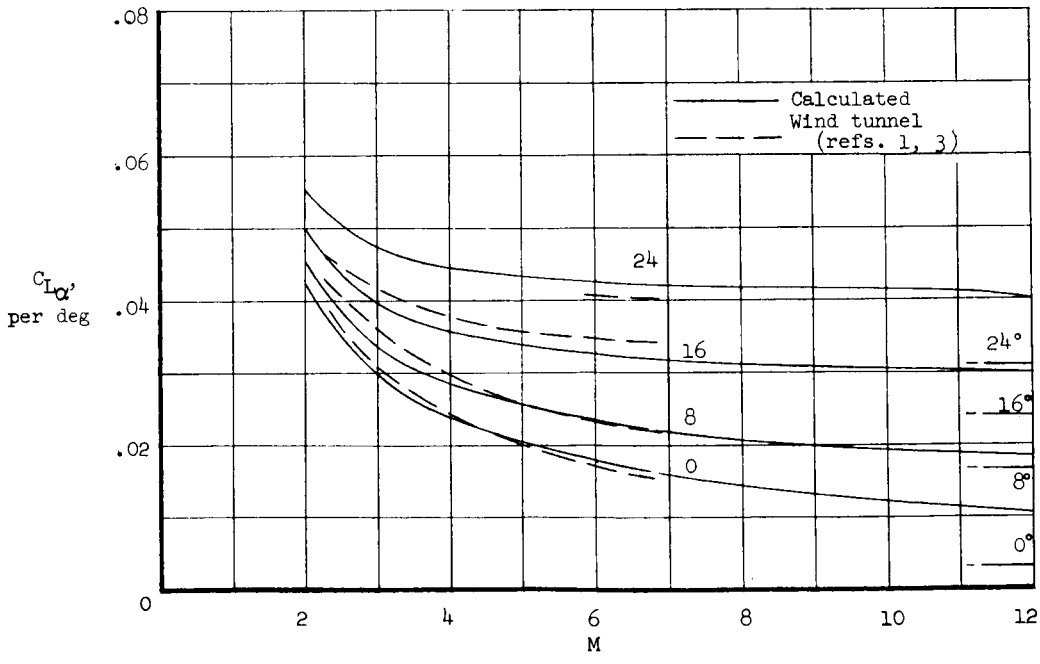

(b) Horizontal tail off.

Figure 10.- Comparison of calculated and experimental lift-curve slopes of the X-15 airplane with the horizontal tail on and off.

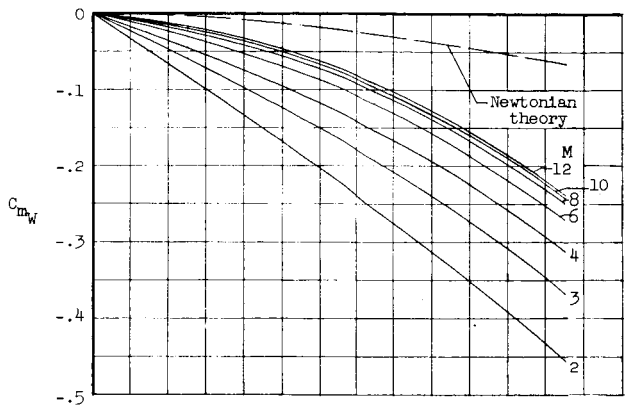

(a) Wing.

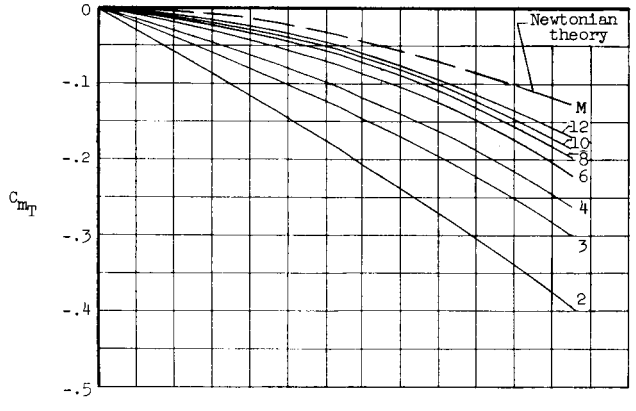

(b) Horizontal tail.

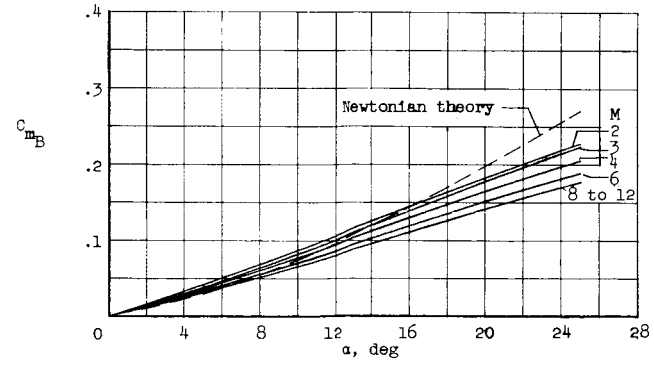

(c) Fuselage.

Figure 11.- Calculated pitching-moment characteristics of the wing and the horizontal tail. $i_T = 0^\circ$.

[redacted]

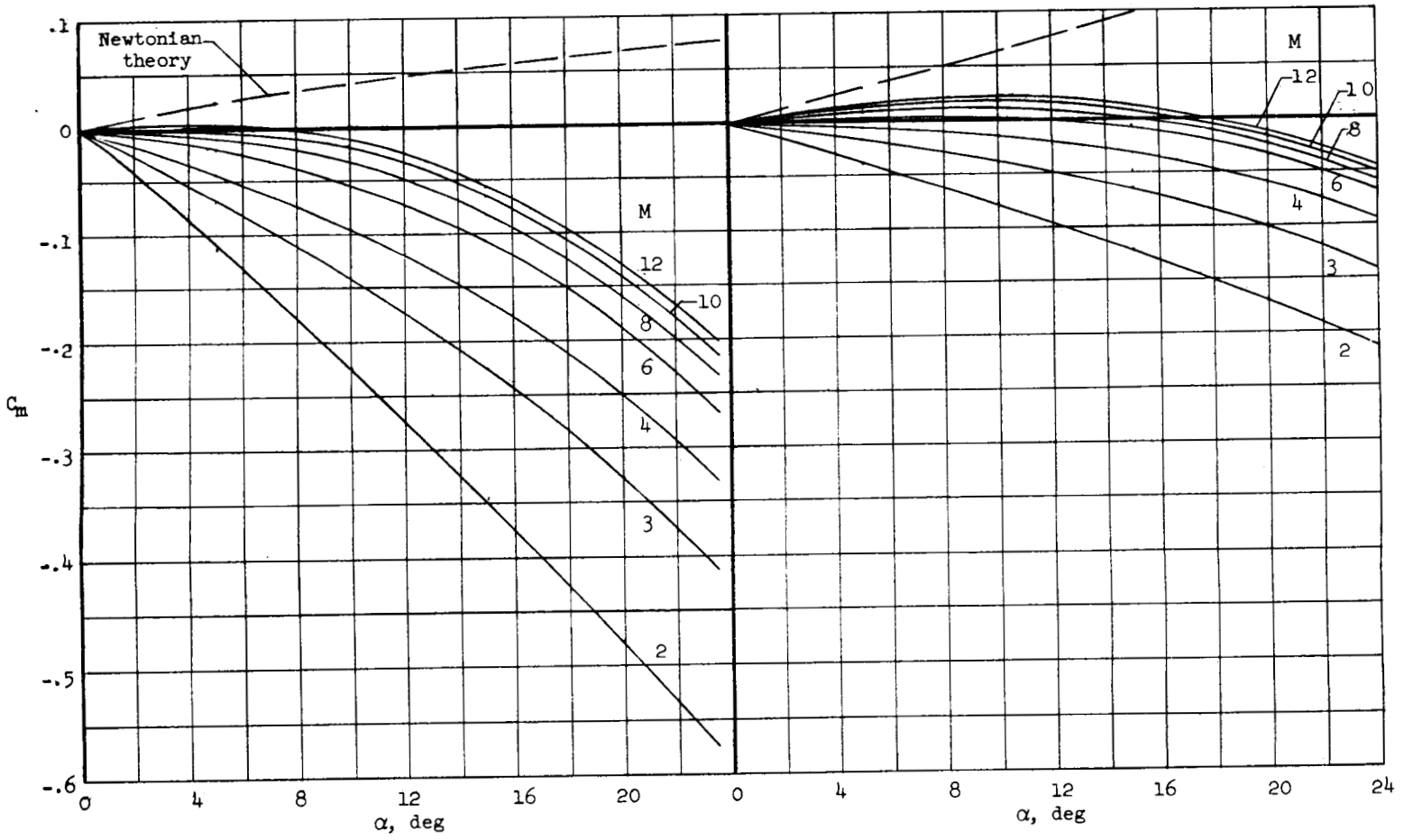

(a) Horizontal tail on. $i_T = 0^o$.

(b) Horizontal tail off.

Figure 12.- Calculated pitching-moment characteristics of the X-15 airplane with the horizontal tail on and off.

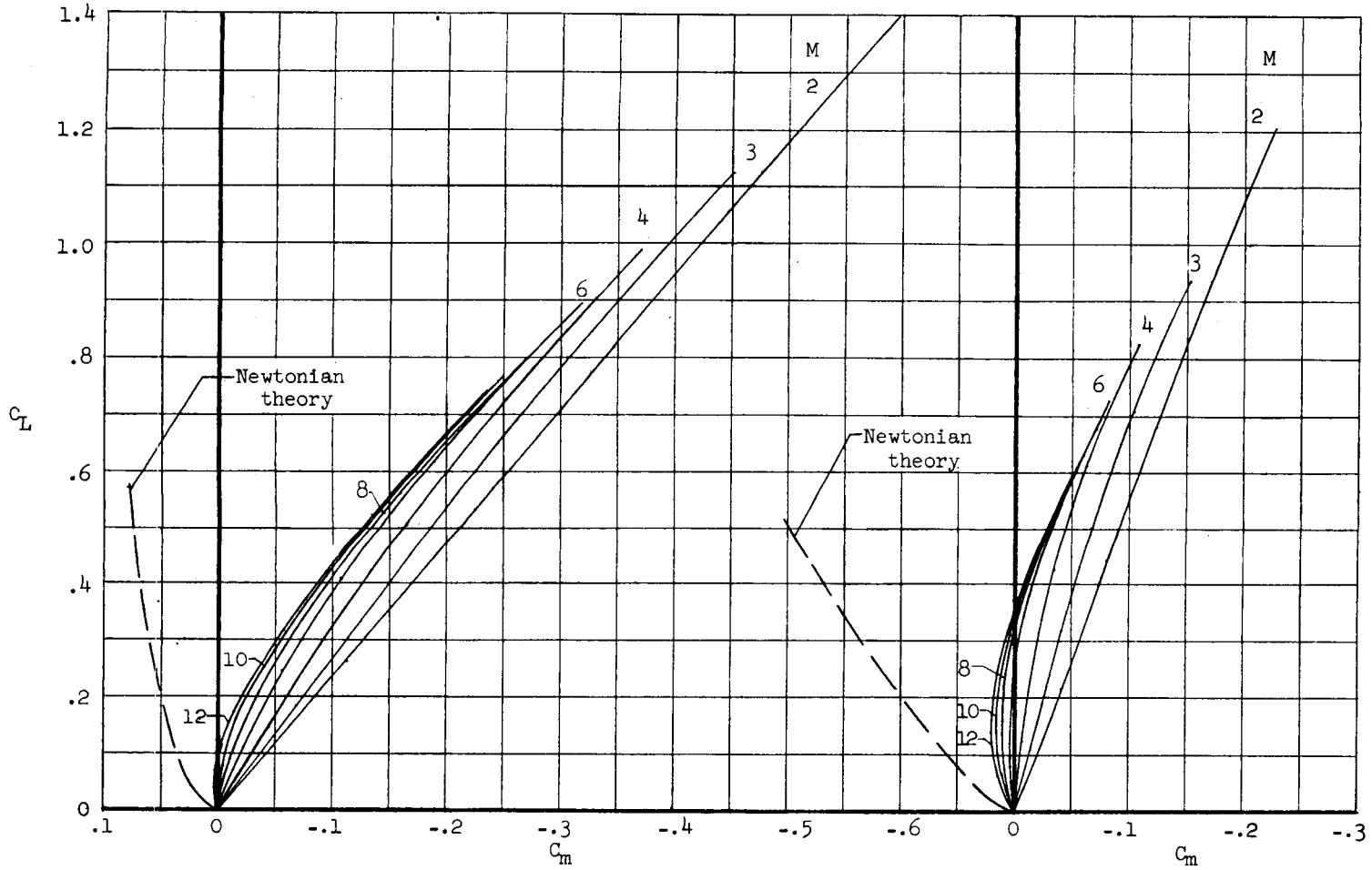

(a) Horizontal tail on. $i_T = 0^o$.

(b) Horizontal tail off.

Figure 13.- Calculated stability characteristics of the X-15 airplane with the horizontal tail on and off.

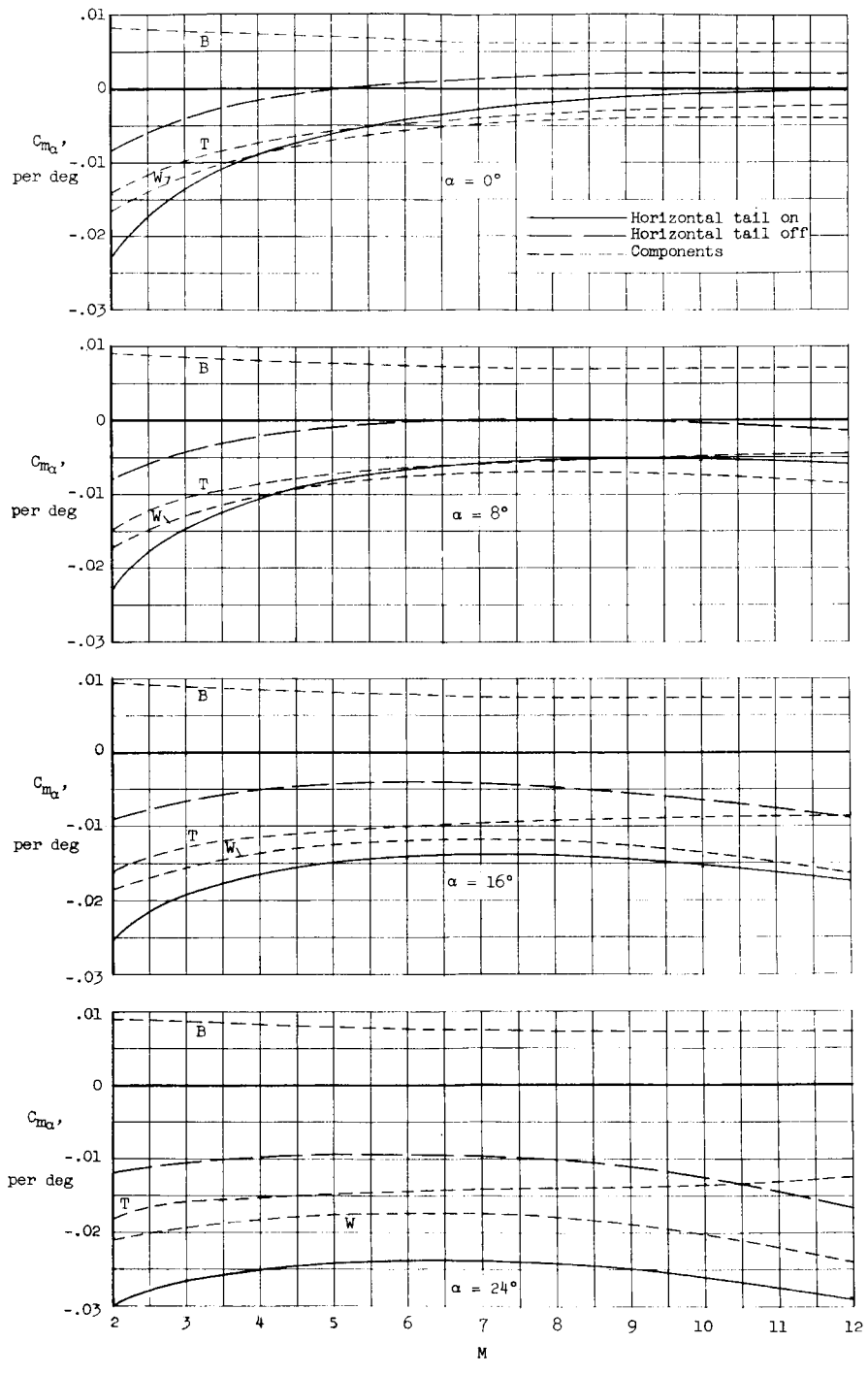

Figure 14.- Buildup of calculated pitching-moment characteristics for the X-15 airplane at angles of attack of 0°, 8°, 16°, and 24°. $i_T = 0°$.

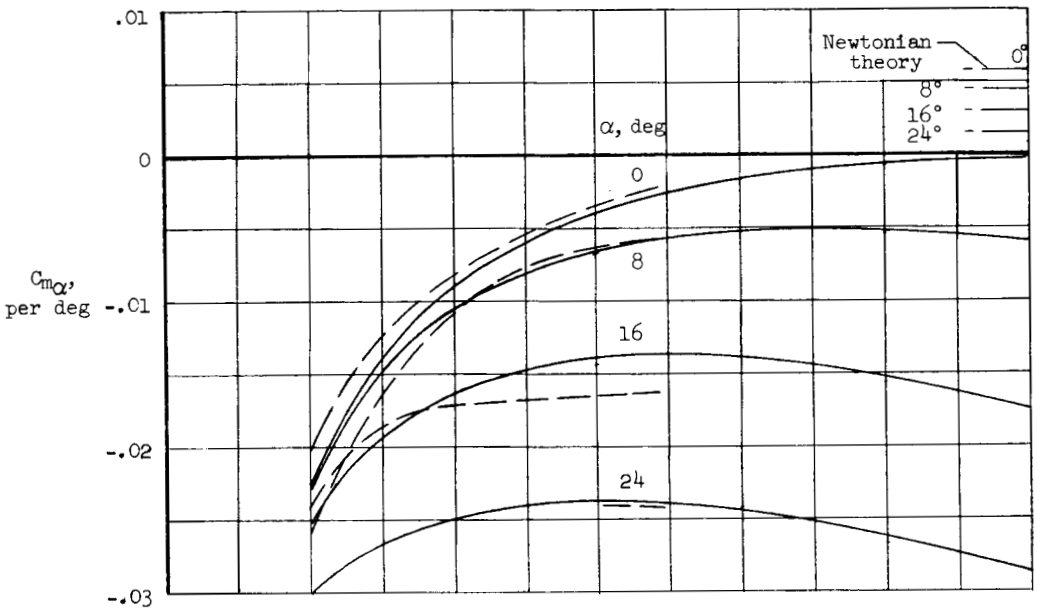

(a) Horizontal tail on. $i_T = 0^o$.

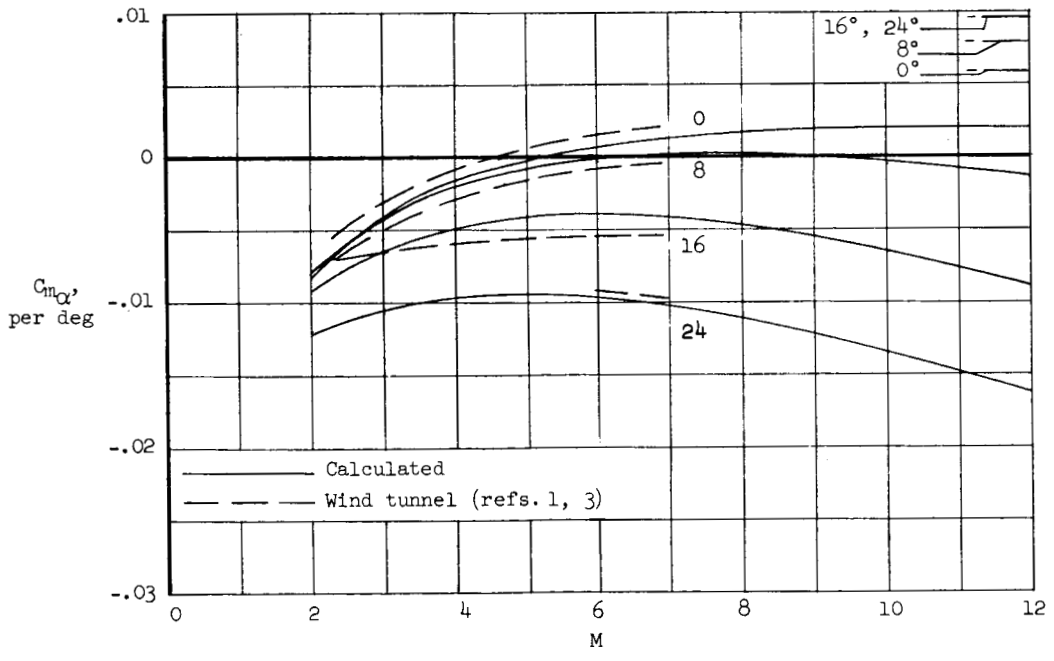

(b) Horizontal tail off.

Figure 15.- Comparison of calculated and experimental values of C_{m_α} for the X-15 airplane with the horizontal tail on and off.

[redacted]

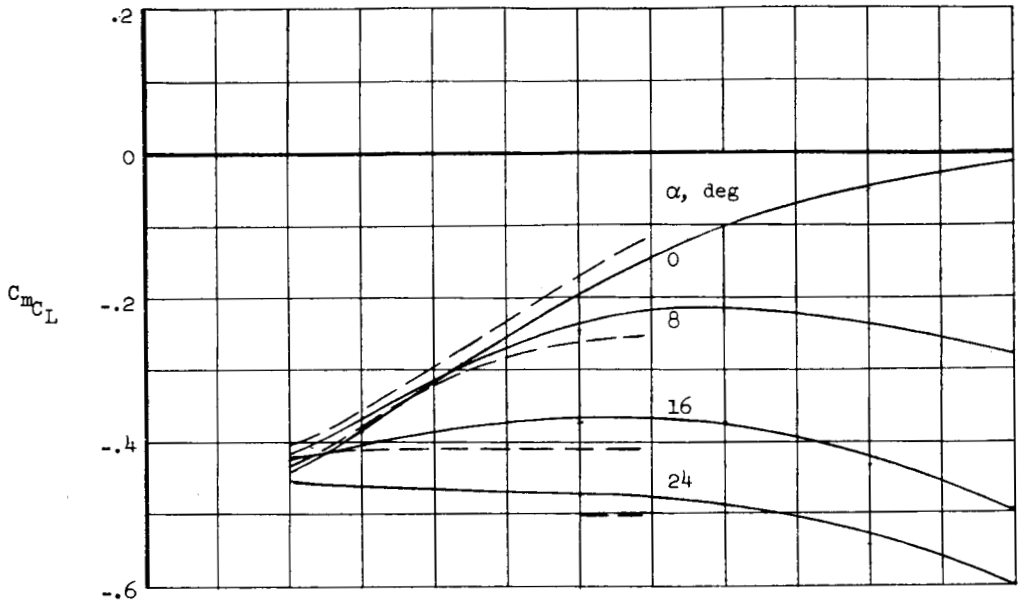

(a) Horizontal tail on. $i_T = 0^o$.

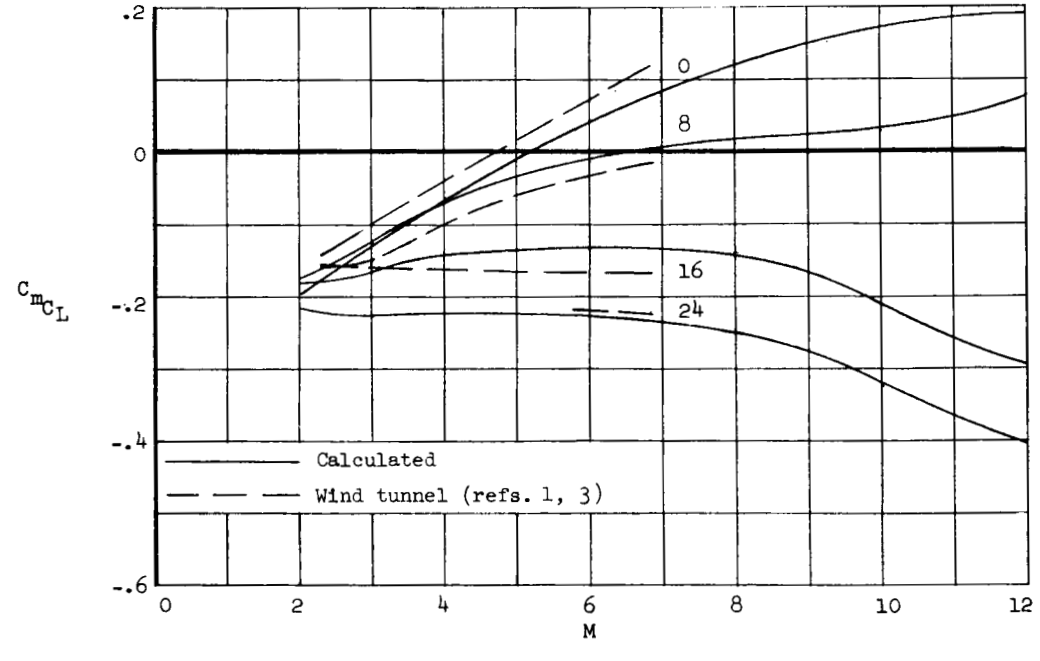

(b) Horizontal tail off.

Figure 16.- Comparison of the calculated and experimental static margins for the X-15 airplane with the horizontal tail on and off.

[redacted]

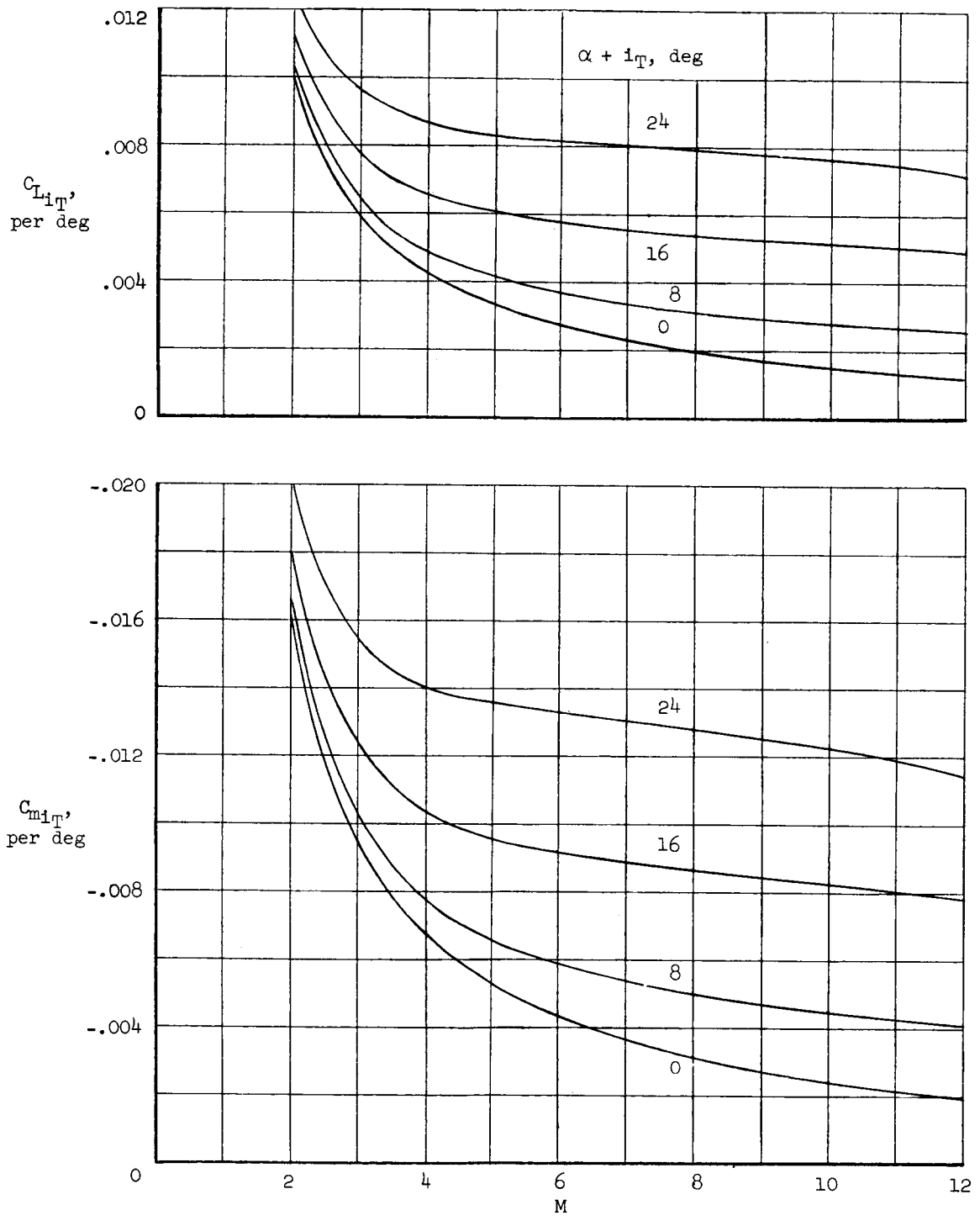

Figure 17.- Calculated effectiveness of the horizontal stabilizer of the X-15 airplane.

H-146

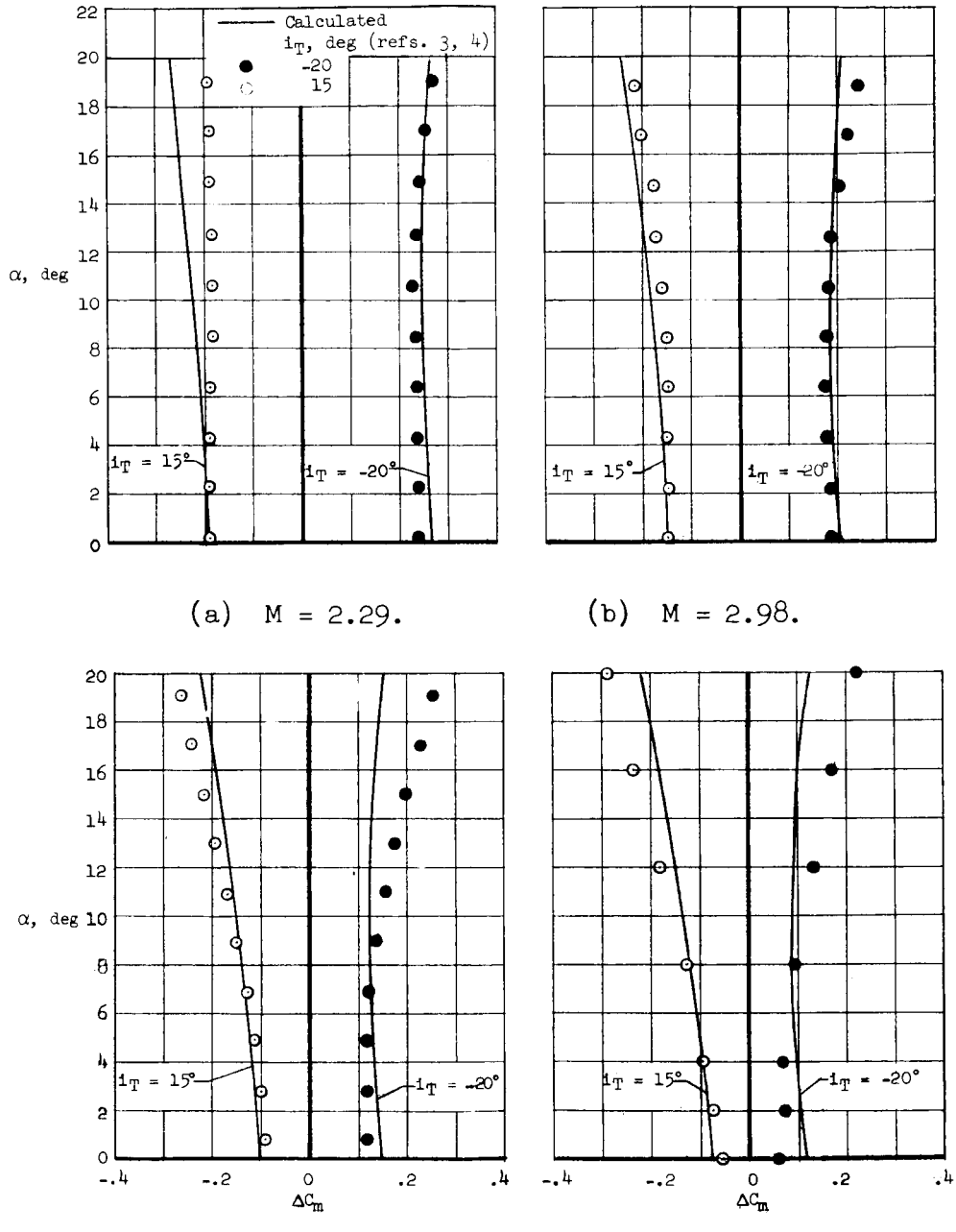

(a) M = 2.29. (b) M = 2.98.

(c) M = 4.65. (d) M = 6.86.

Figure 18.- Comparison of the calculated and experimental stabilizer effectiveness of the X-15 airplane for incidence settings of 15° (leading edge up) and -20° (leading edge down) at various Mach numbers.

H-146

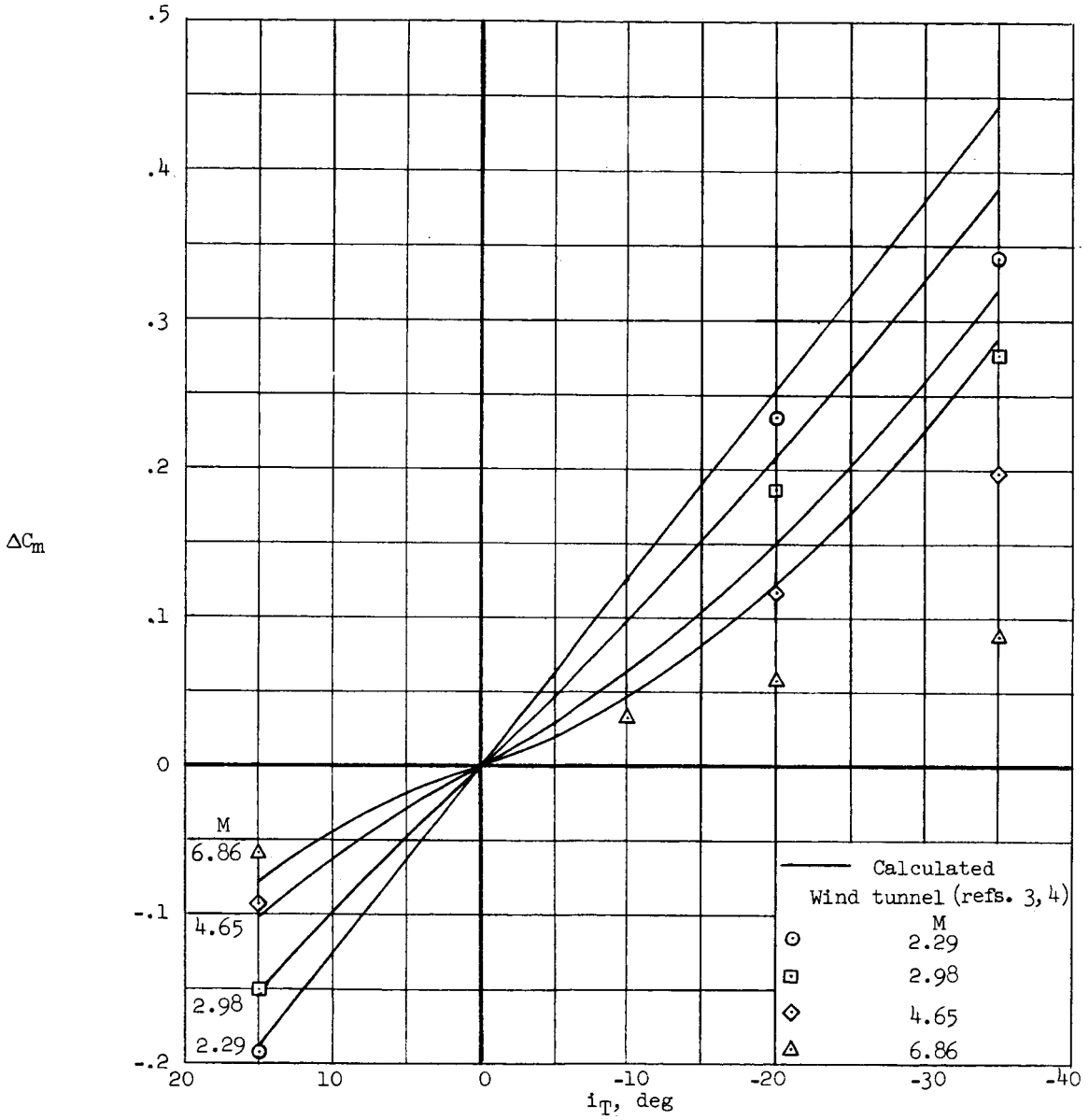

Figure 19.- Comparison of the calculated and experimental stabilizer characteristics for the X-15 airplane for several Mach numbers at zero angle of attack.

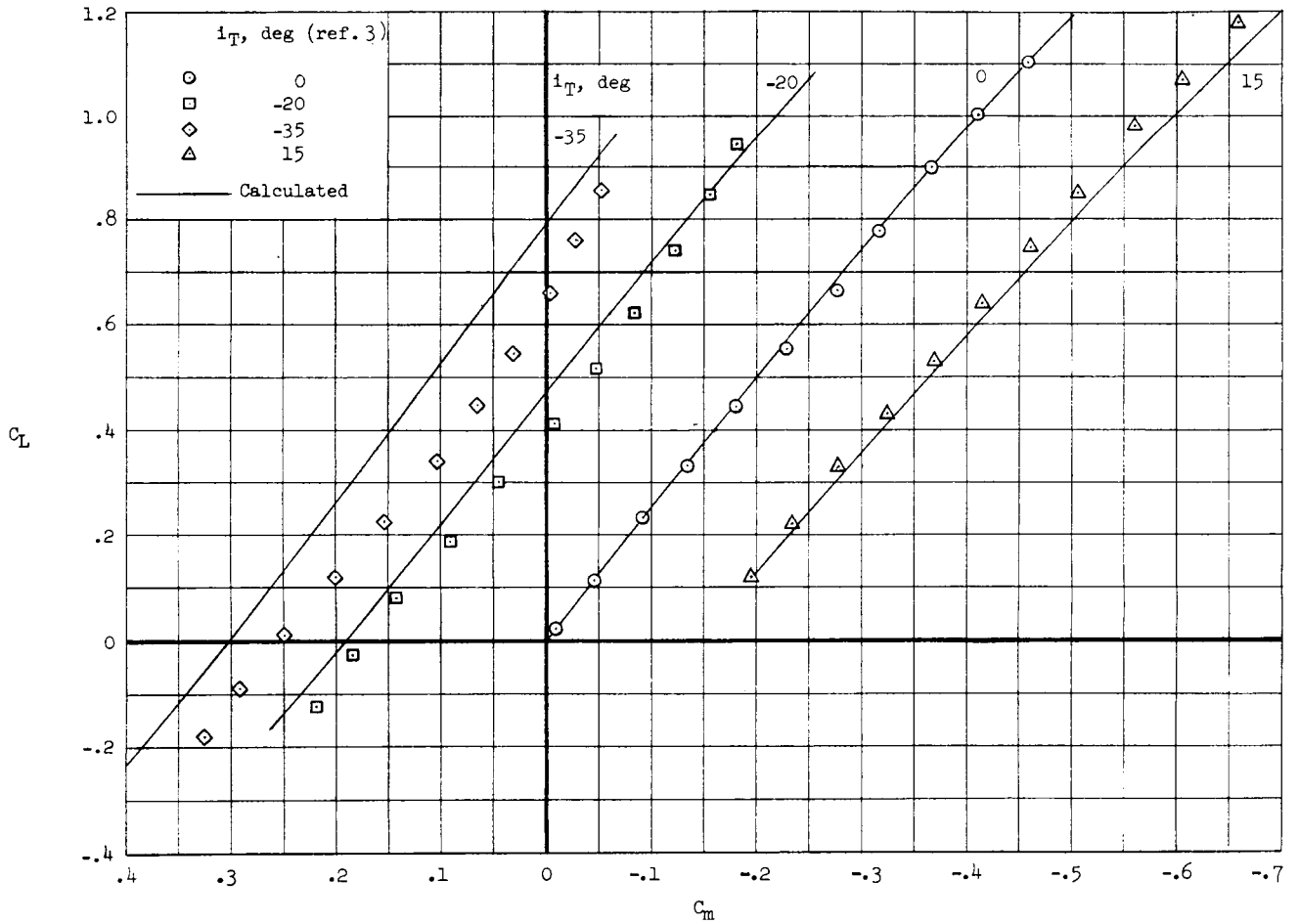

(a) M = 2.29.

Figure 20.- Comparison of the calculated and experimental stability characteristics of the X-15 airplane for various Mach numbers and stabilizer-incidence settings.

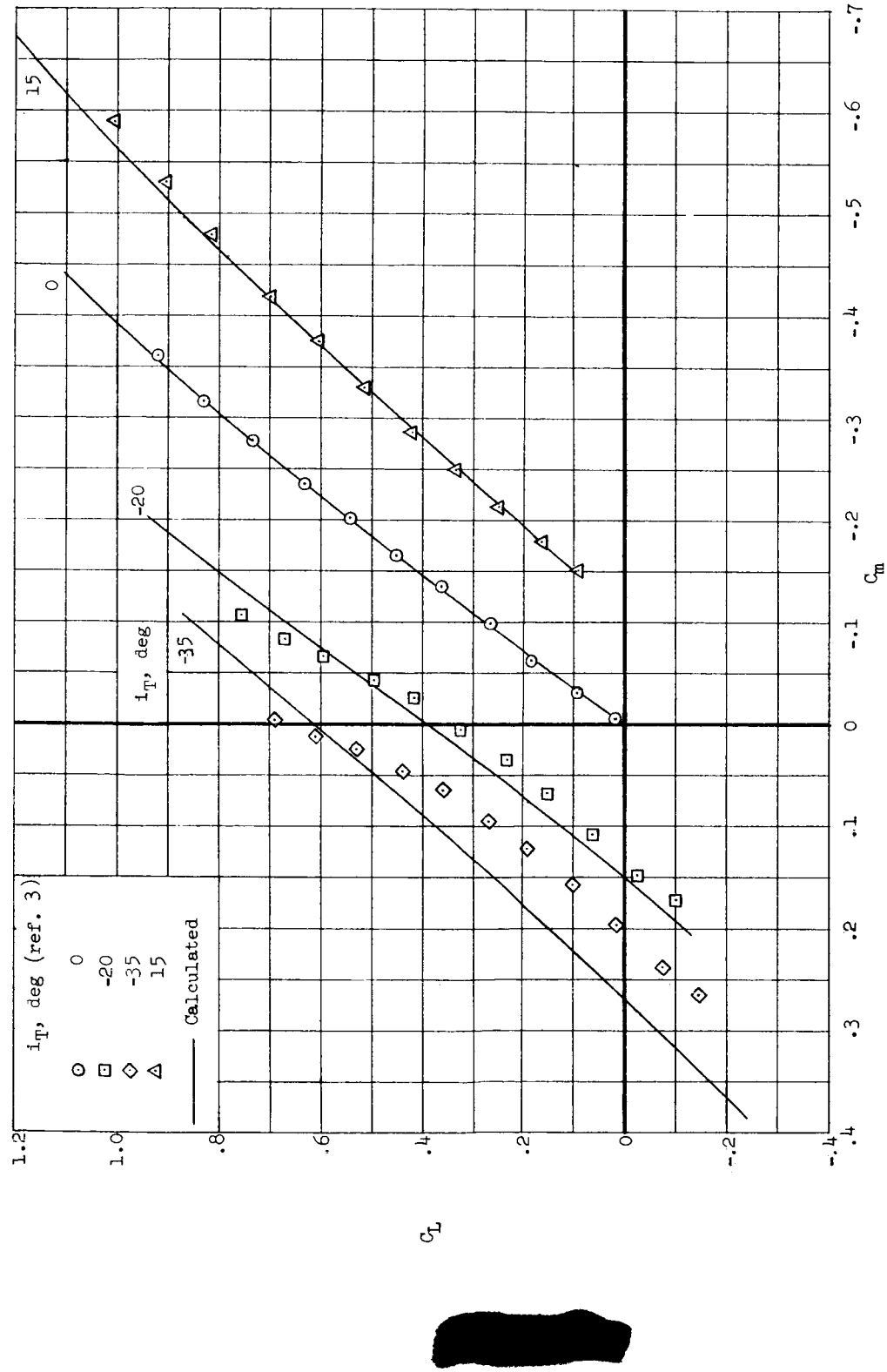

(b) M = 2.98.

Figure 20.- Continued.

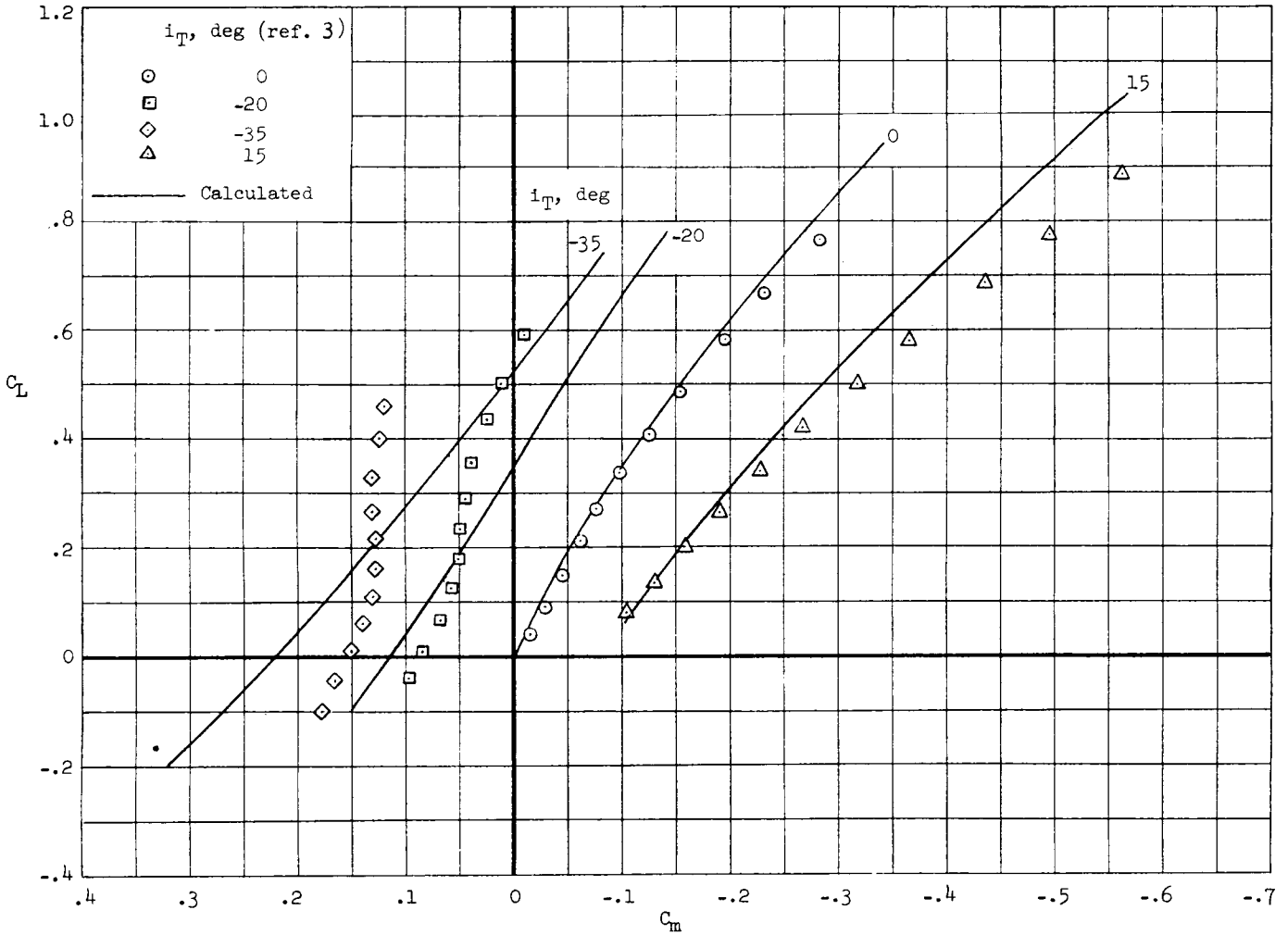

(c) M = 4.65.

Figure 20.- Continued.

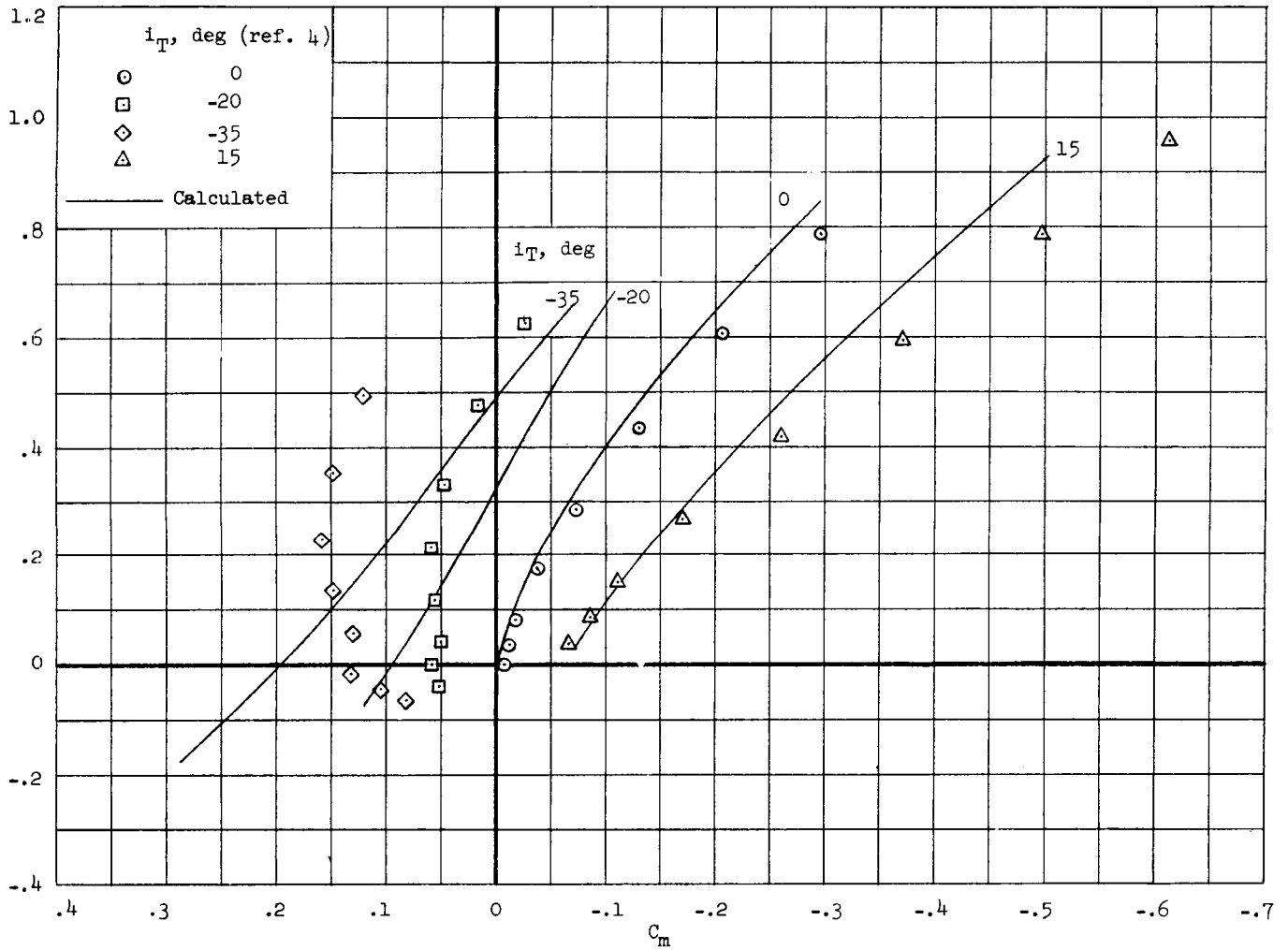

(d) M = 6.86.

Figure 20.- Concluded.

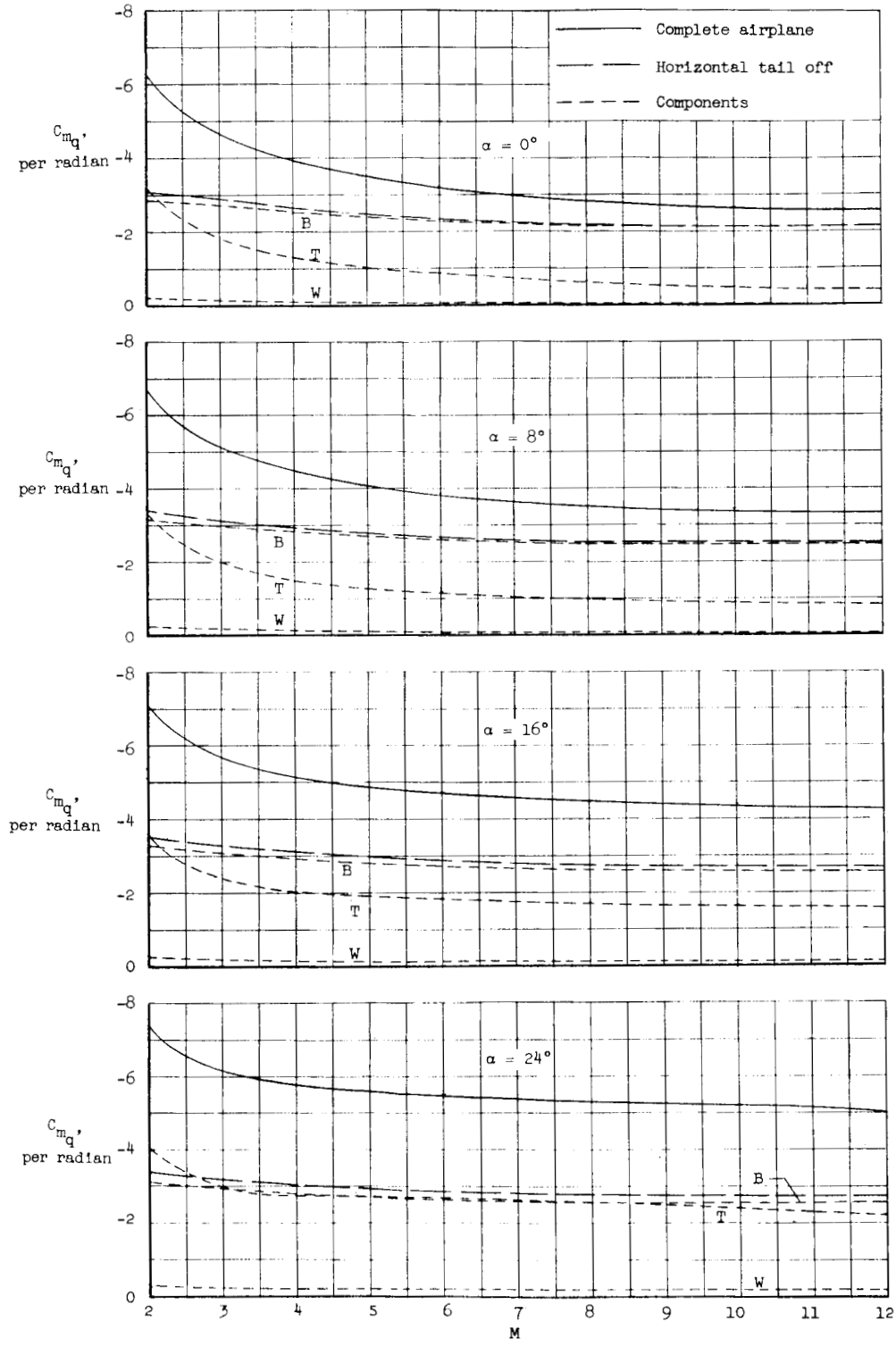

Figure 21.- Buildup of the calculated damping characteristics due to pitching rate for the X-15 airplane at angles of attack of 0°, 8°, 16°, and 24°. $i_T = 0°$.

[redacted]

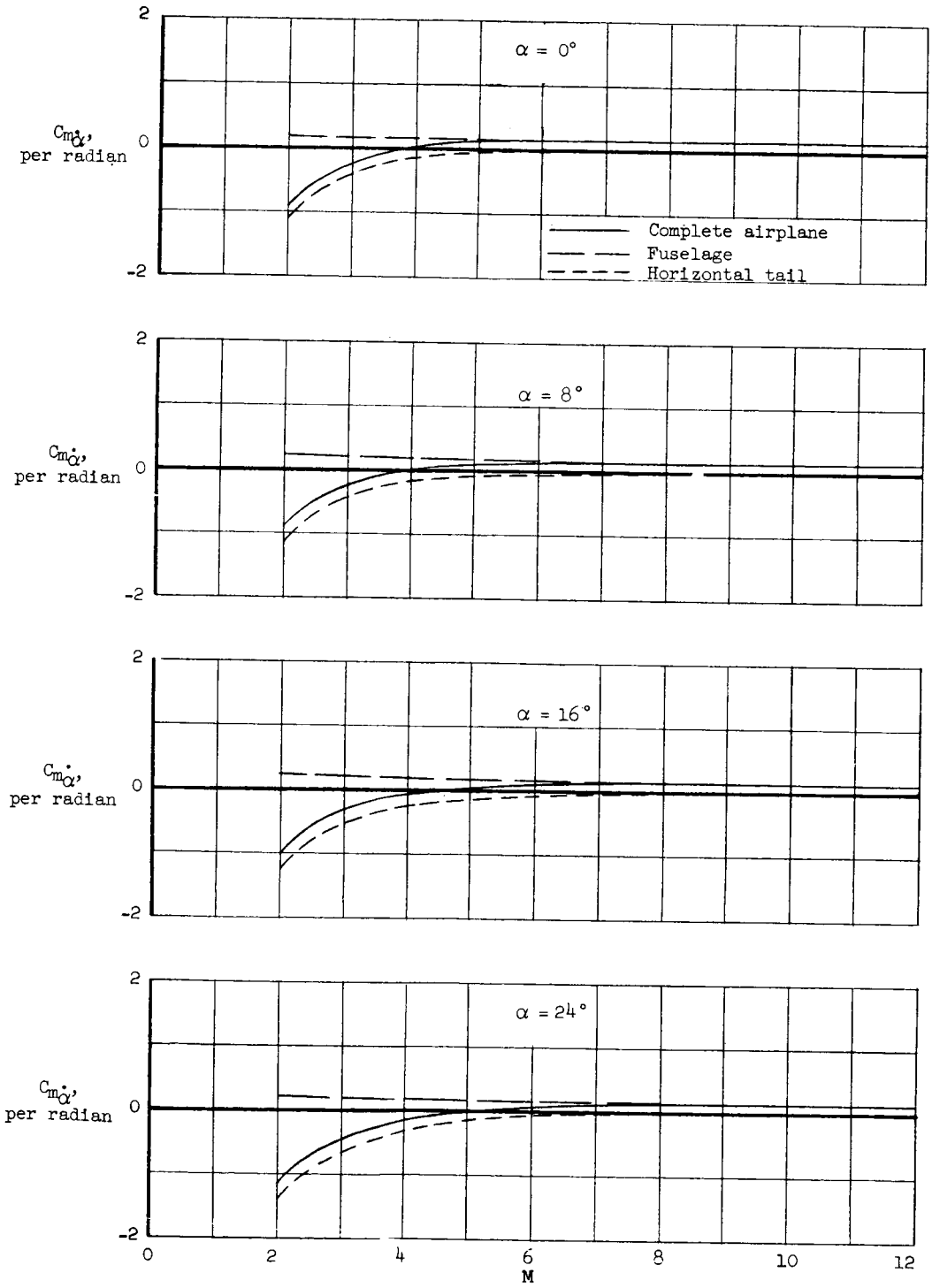

Figure 22.- Buildup of the calculated damping characteristics due to vertical acceleration for the X-15 airplane. $i_T = 0^o$.

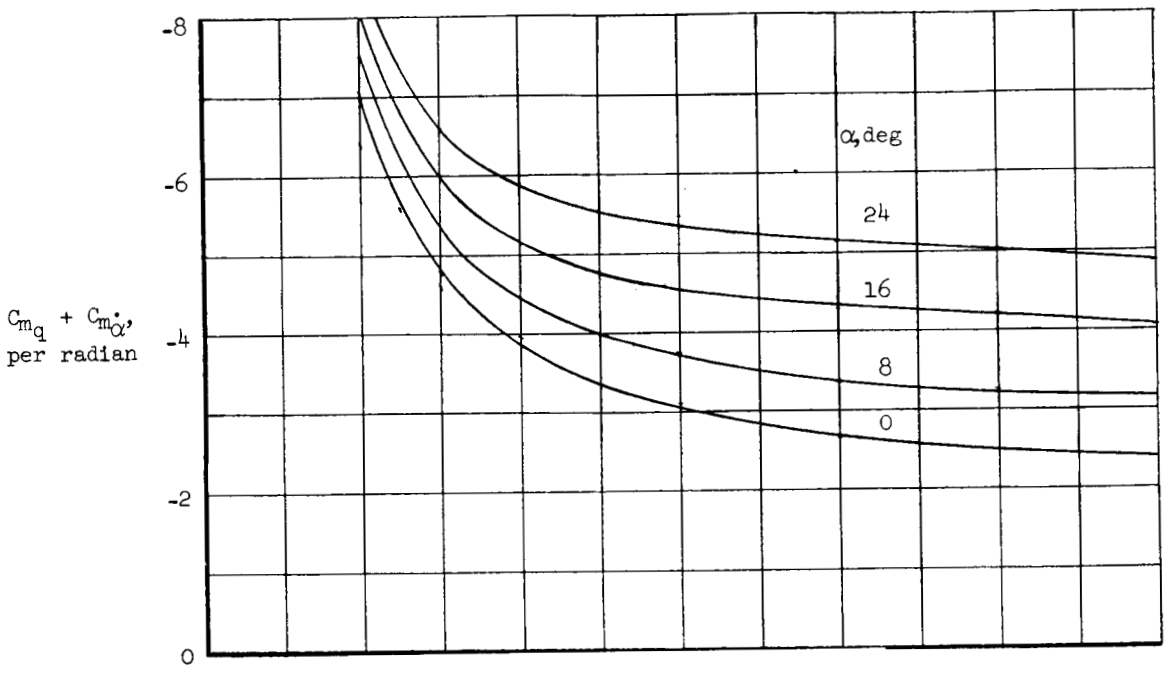

(a) Horizontal tail on. $i_T = 0^o$.

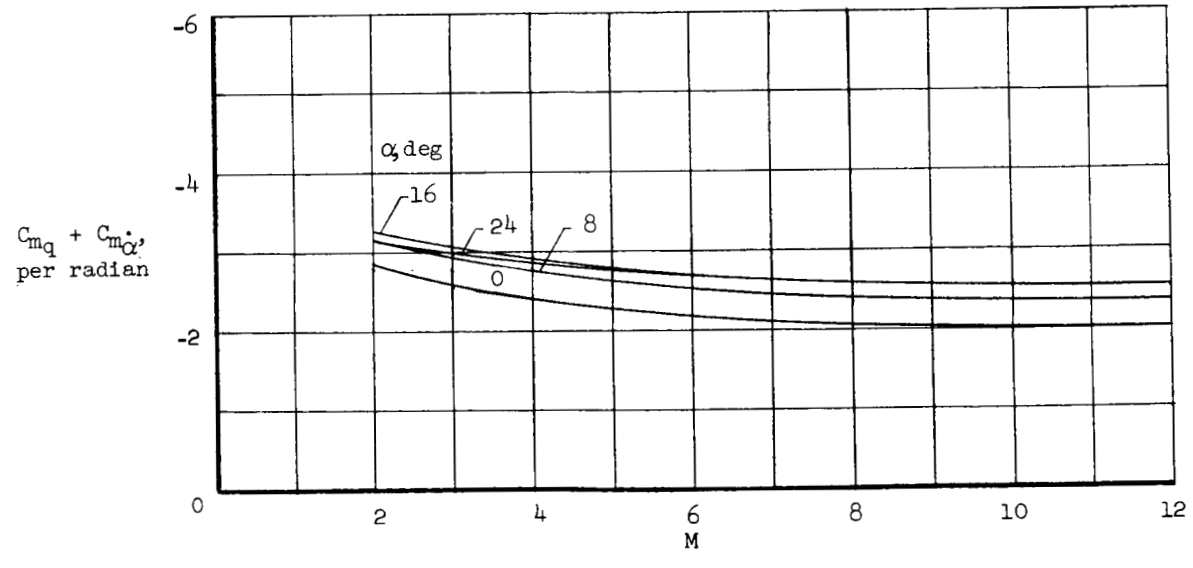

(b) Horizontal tail off.

Figure 23.- Calculated damping-in-pitch derivatives for the X-15 airplane.

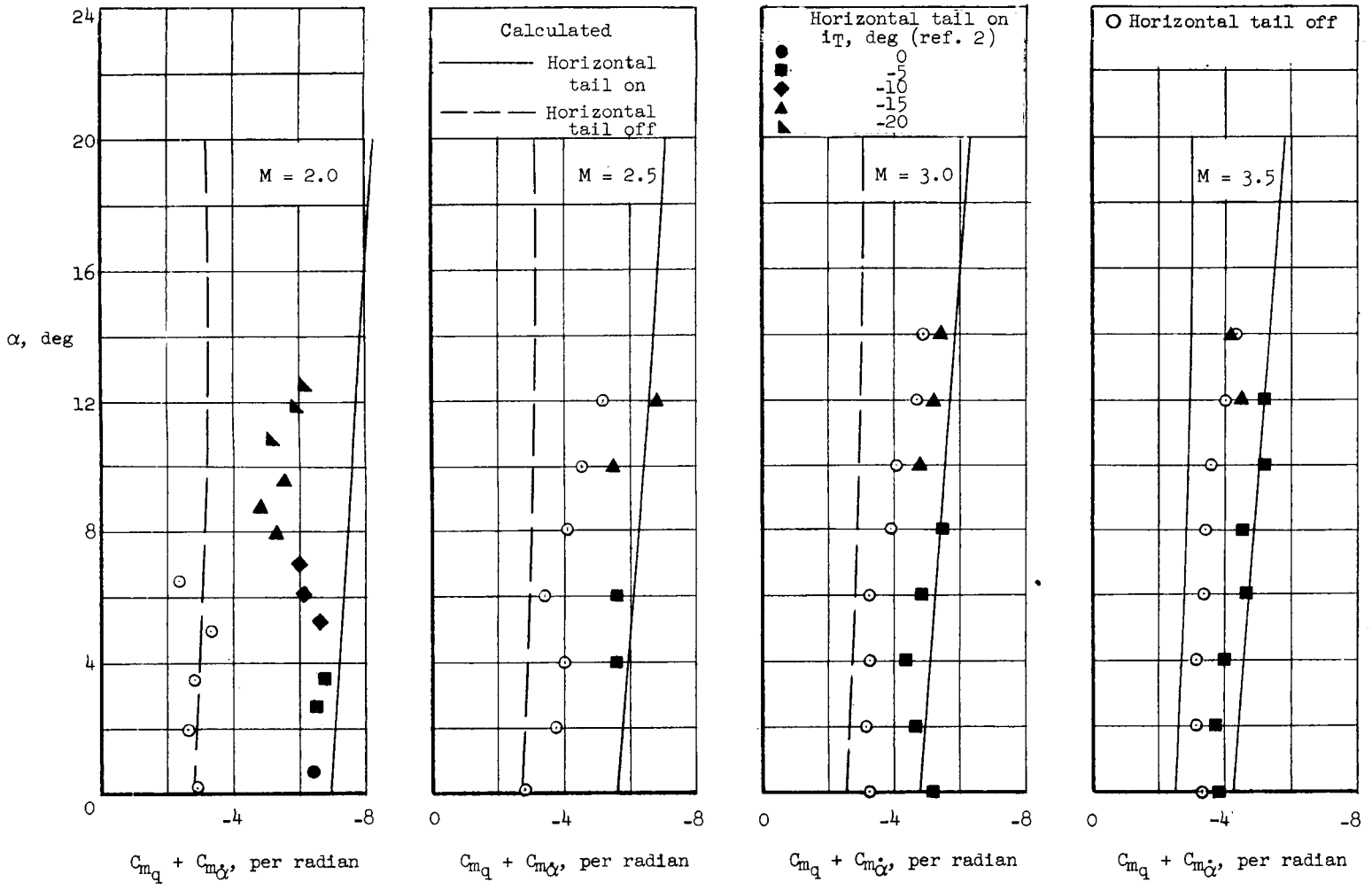

Figure 24.- Comparison of the calculated and experimental damping-in-pitch derivatives for the X-15 airplane with horizontal tail on and off at several Mach numbers. $i_T = 0^o$.

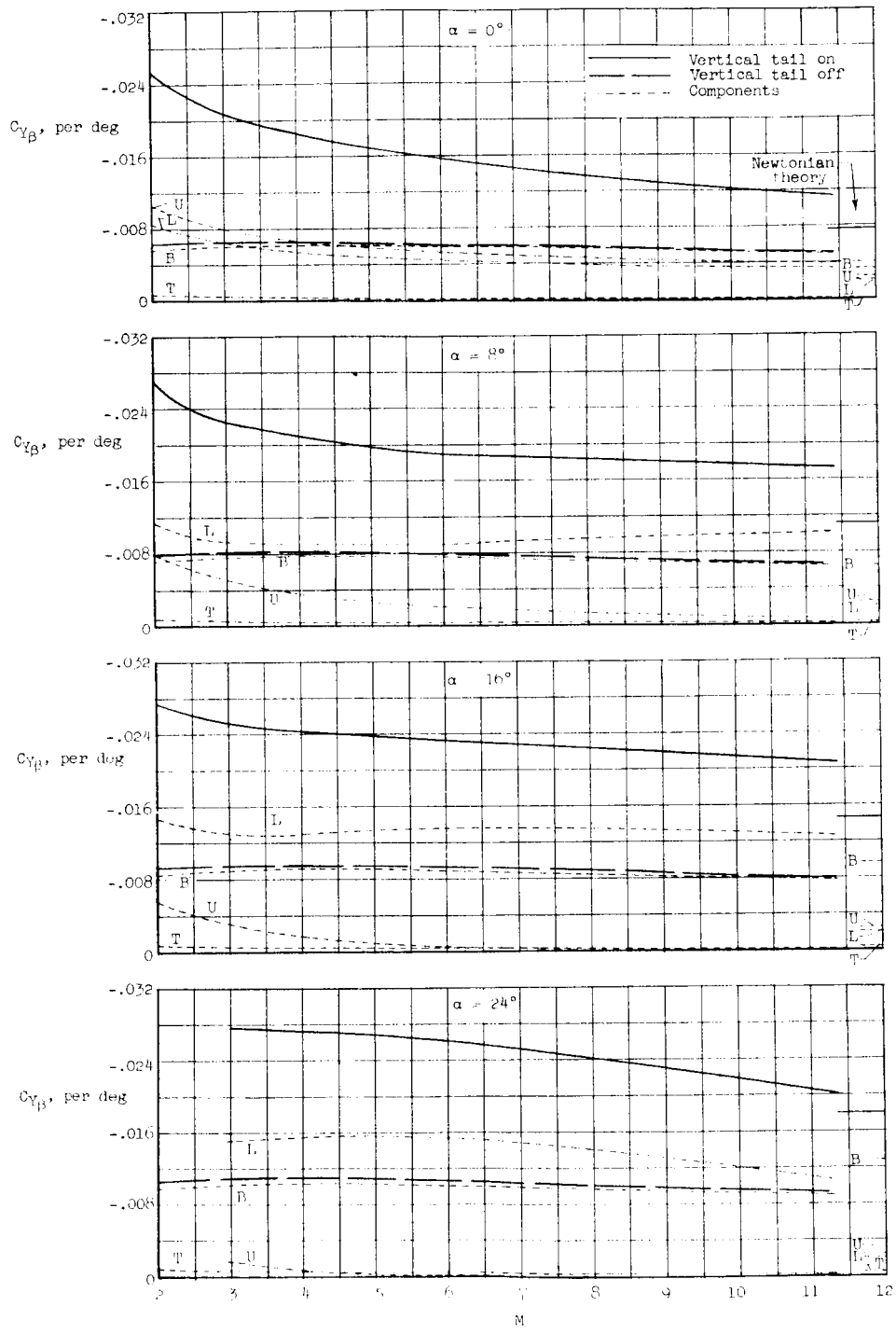

Figure 25.- Buildup of the calculated side-force characteristics of the X-15 airplane at angles of attack of 0°, 8°, 16°, and 24°. $i_T = 0°$.

DECLASSIFIED

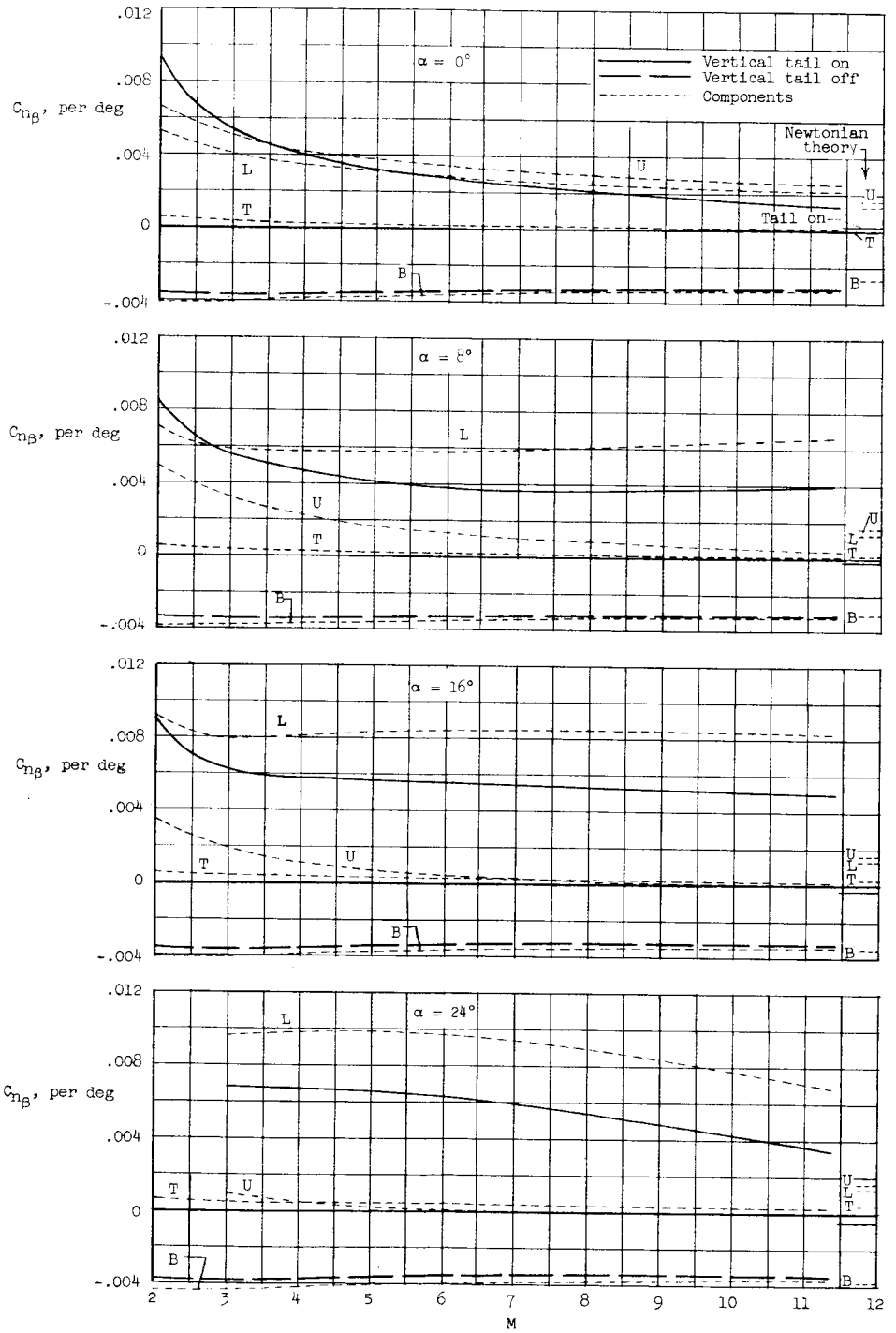

Figure 26.- Buildup of the calculated directional-stability characteristics of the X-15 airplane at angles of attack of 0°, 8°, 16°, and 24°. $i_T = 0°$.

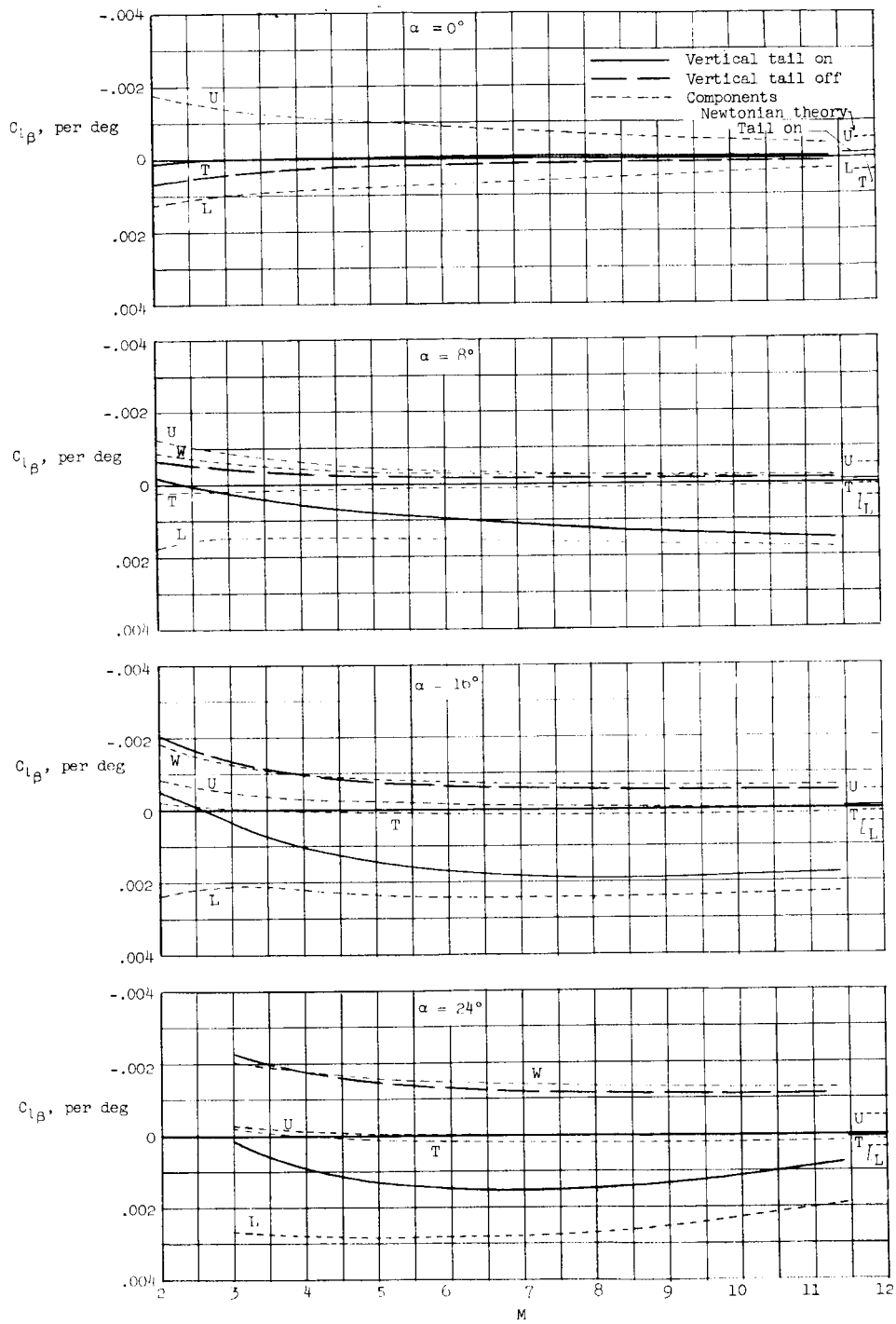

Figure 27.- Buildup of the calculated dihedral effect for the X-15 airplane at angles of attack of 0°, 8°, 16°, and 24°. $i_T = 0°$.

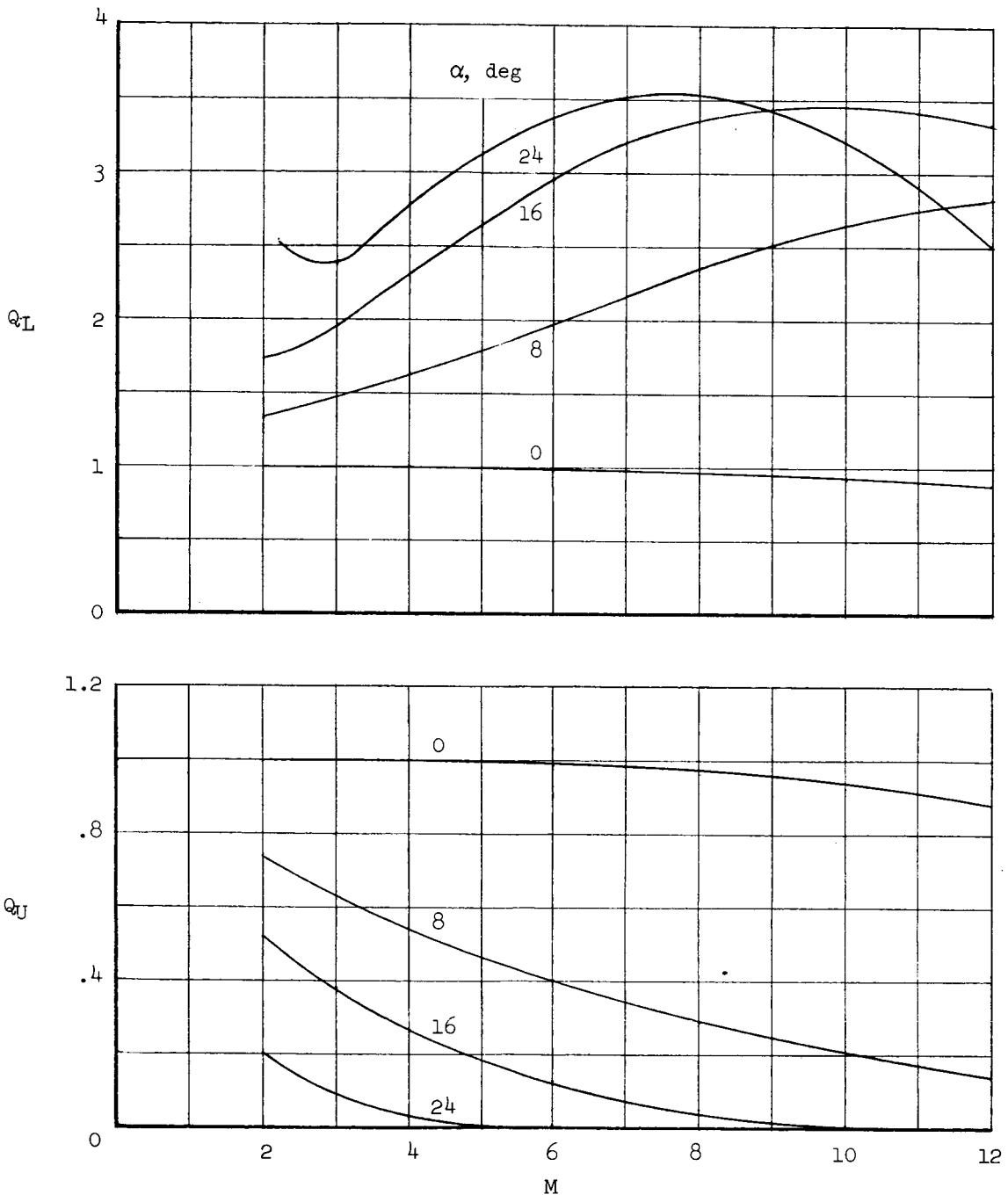

Figure 28.- Effect of wing-body shock fields on lift effectiveness of the upper and lower vertical tails.

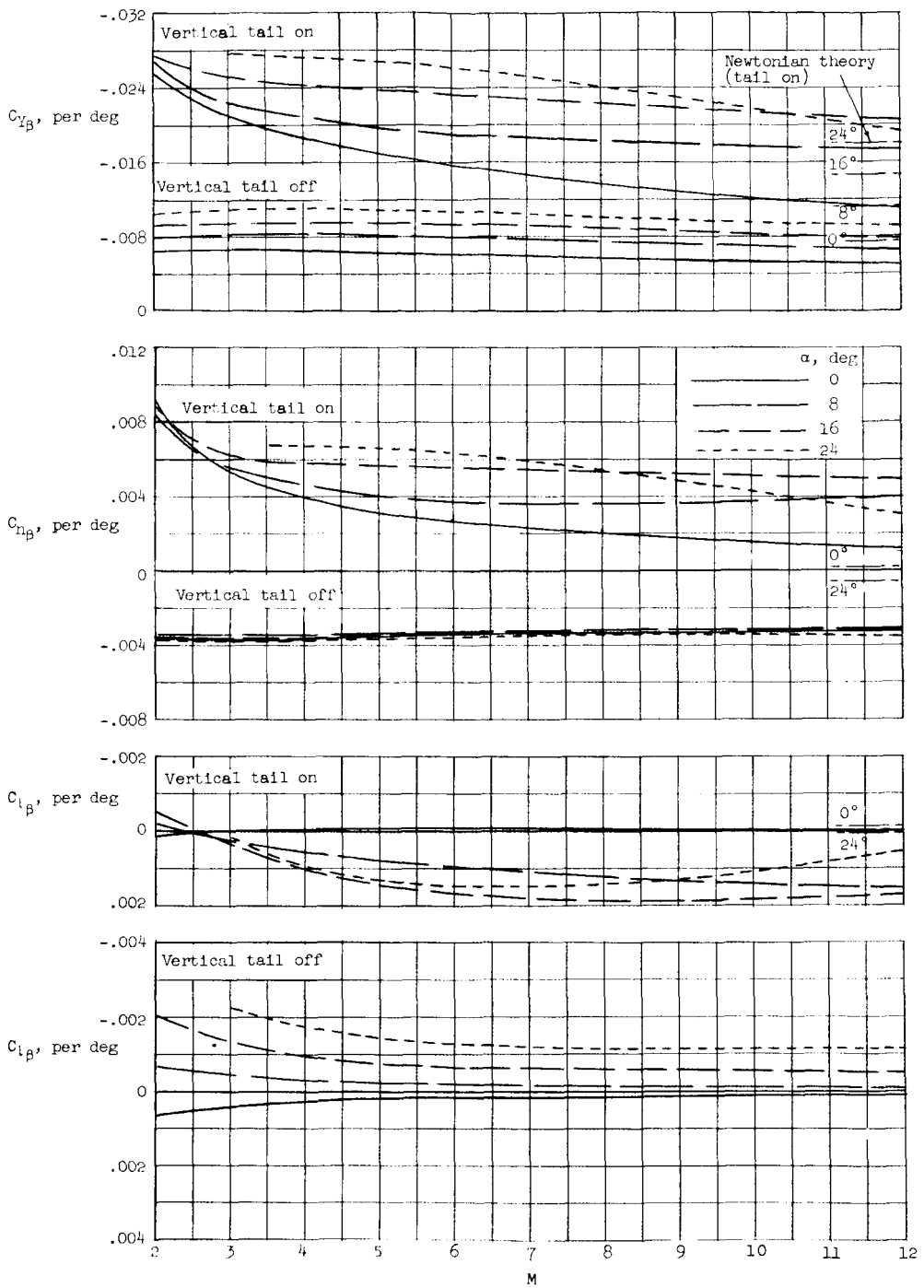

Figure 29.- Summary of the calculated sideslip derivatives for the X-15 airplane with vertical tail on and off at angles of attack of 0°, 8°, 16°, and 24°. $i_T = 0°$.

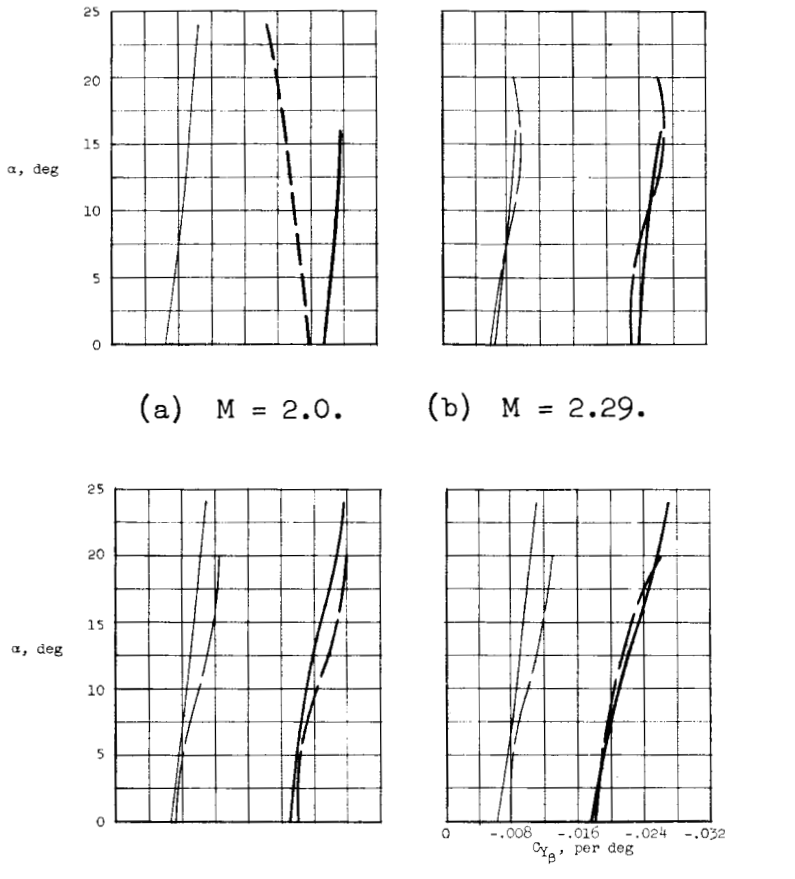

Figure 30.- Comparison of the calculated and experimental side-force derivatives for the X-15 airplane with the vertical tail on and off. $i_T = 0^o$.

H-146

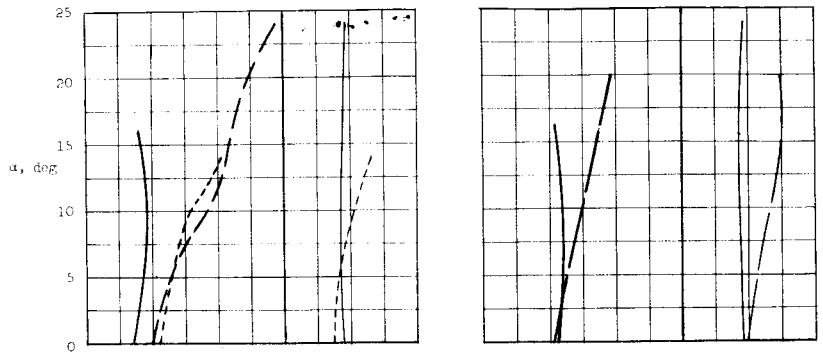

(a) M = 2.0. (b) M = 2.29.

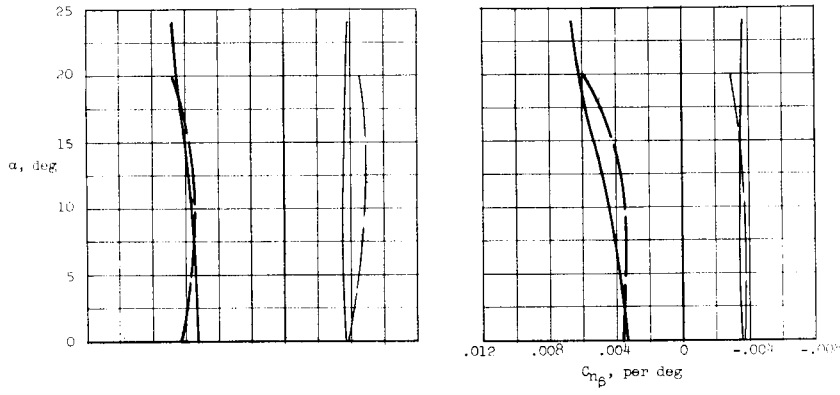

(c) M = 3.0. (d) M = 4.68.

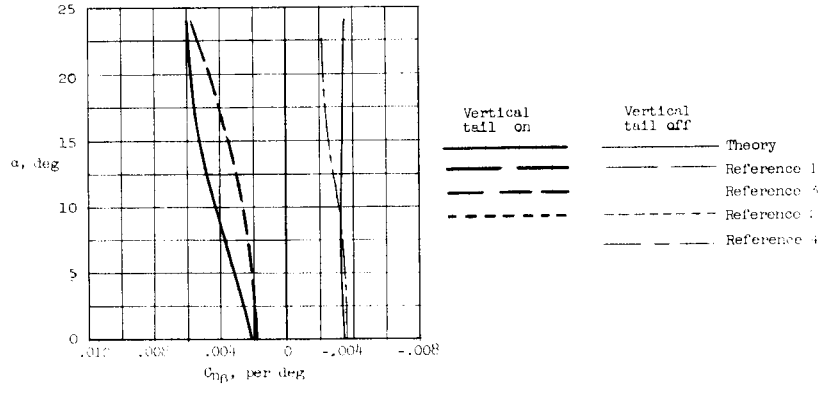

(e) M = 6.86.

Figure 31.- Comparison of the calculated and experimental directional-stability derivatives for the X-15 airplane with the vertical tail on and off. $i_T = 0^\circ$.

DECLASSIFIED

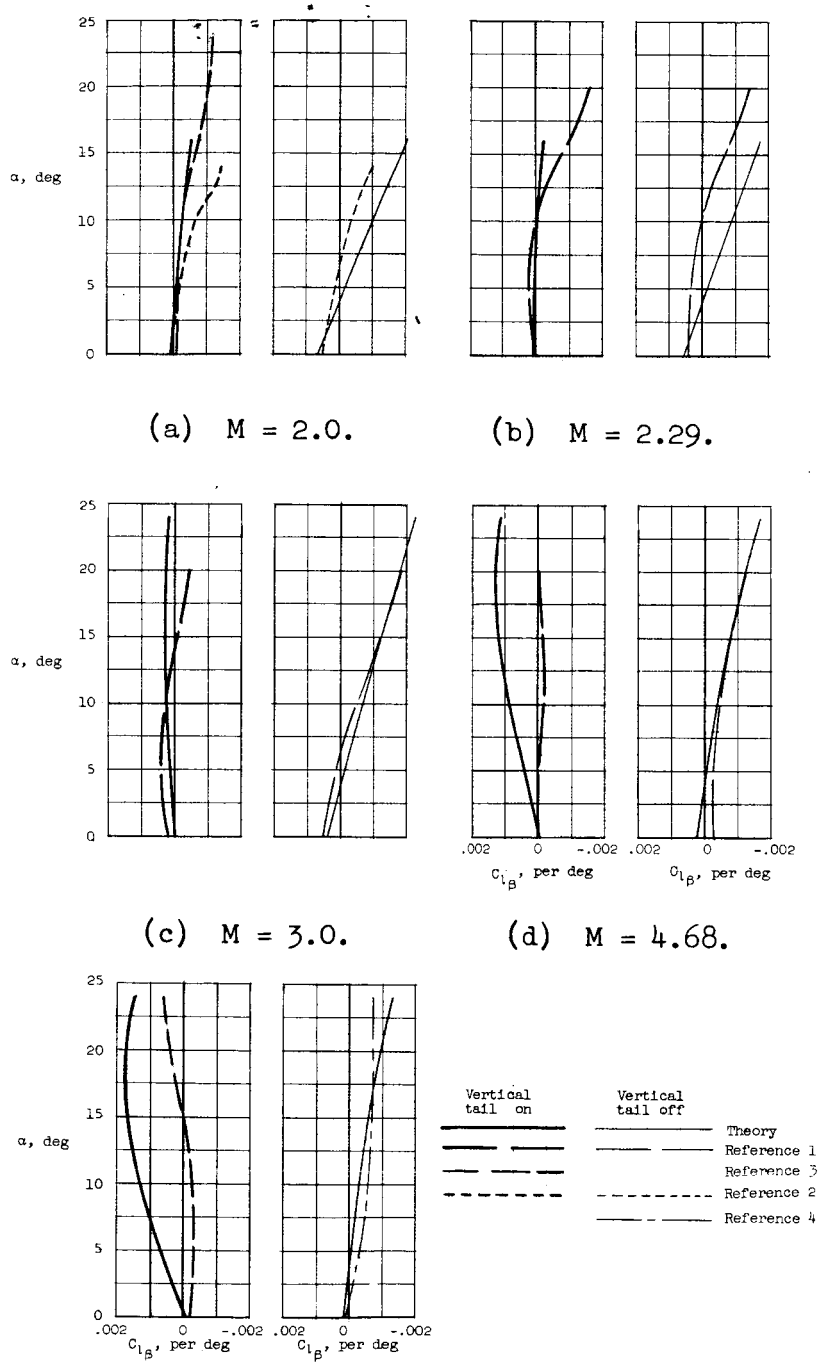

(a) M = 2.0. (b) M = 2.29.

(c) M = 3.0. (d) M = 4.68.

(e) M = 6.86.

Figure 32.- Comparison of the calculated and experimental dihedral effect for the X-15 airplane with the vertical tail on and off. $i_T = 0^\circ$.

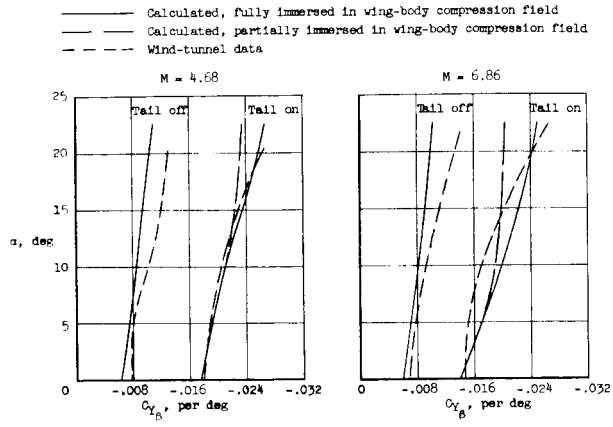

(a) Side-force derivative.

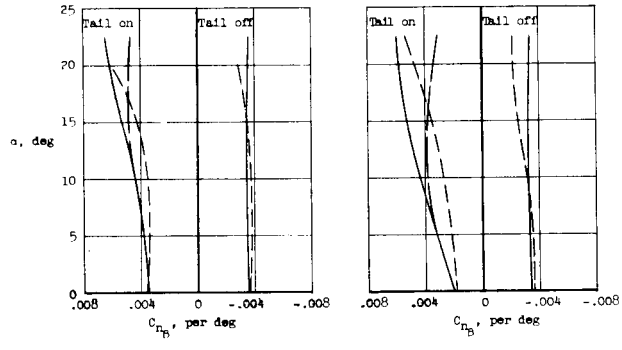

(b) Yawing-moment derivative.

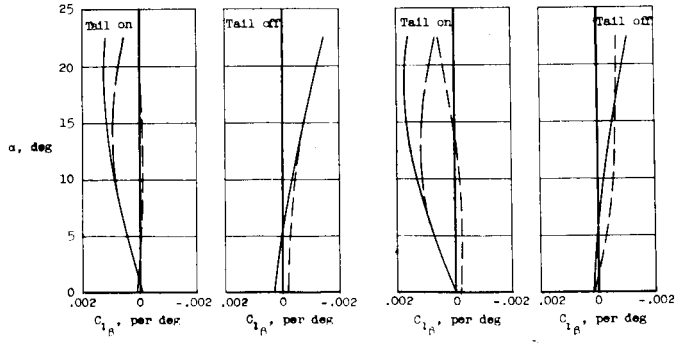

(c) Rolling-moment derivative.

Figure 33.- Comparison of experimental sideslip derivatives at Mach numbers of 4.65 and 6.86 with those calculated for the lower vertical tail fully and partially immersed in wing-body compression field.

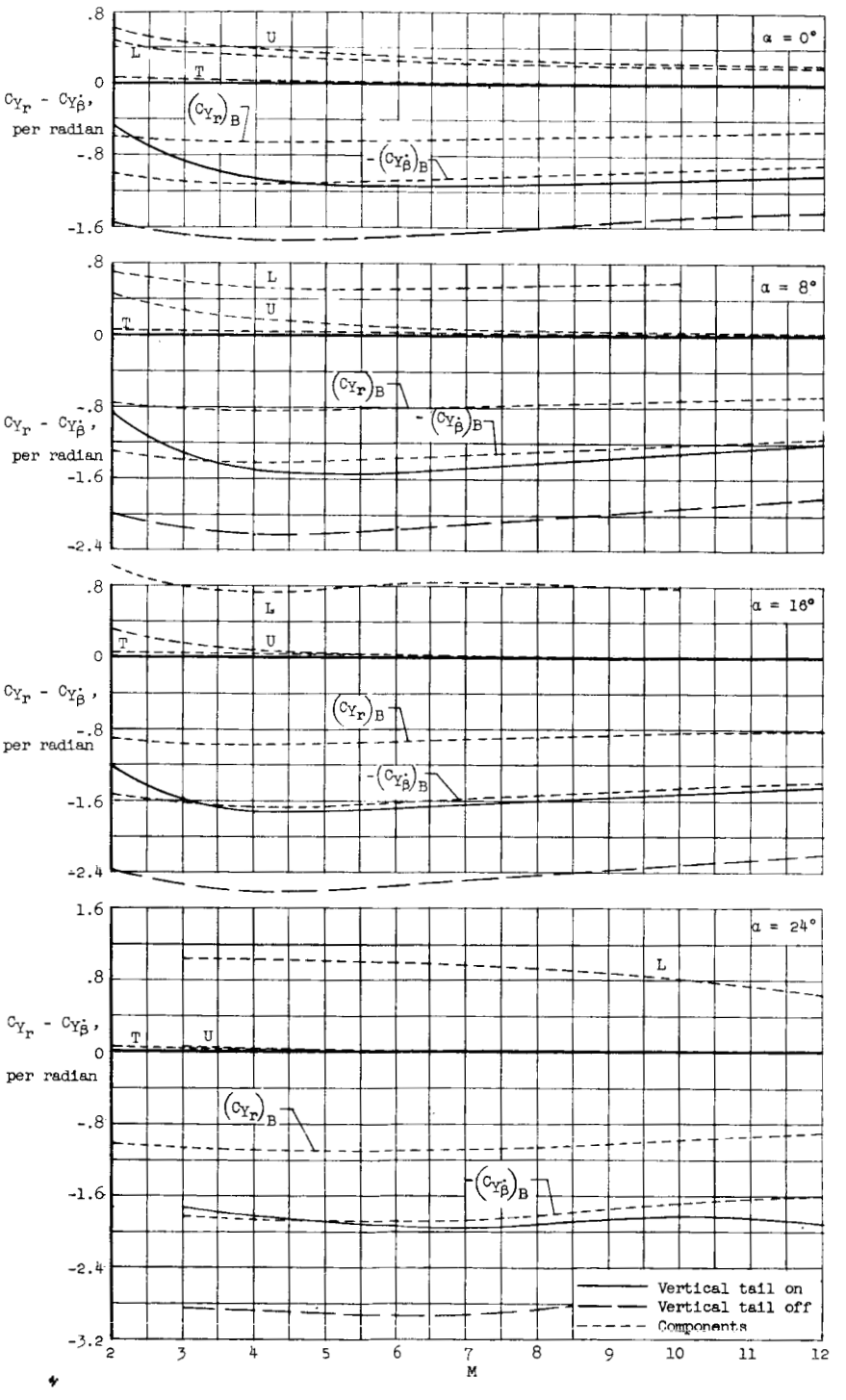

Figure 34.- Buildup of the calculated side-force derivative due to yawing rate for the X-15 airplane. $i_T = 0^o$.

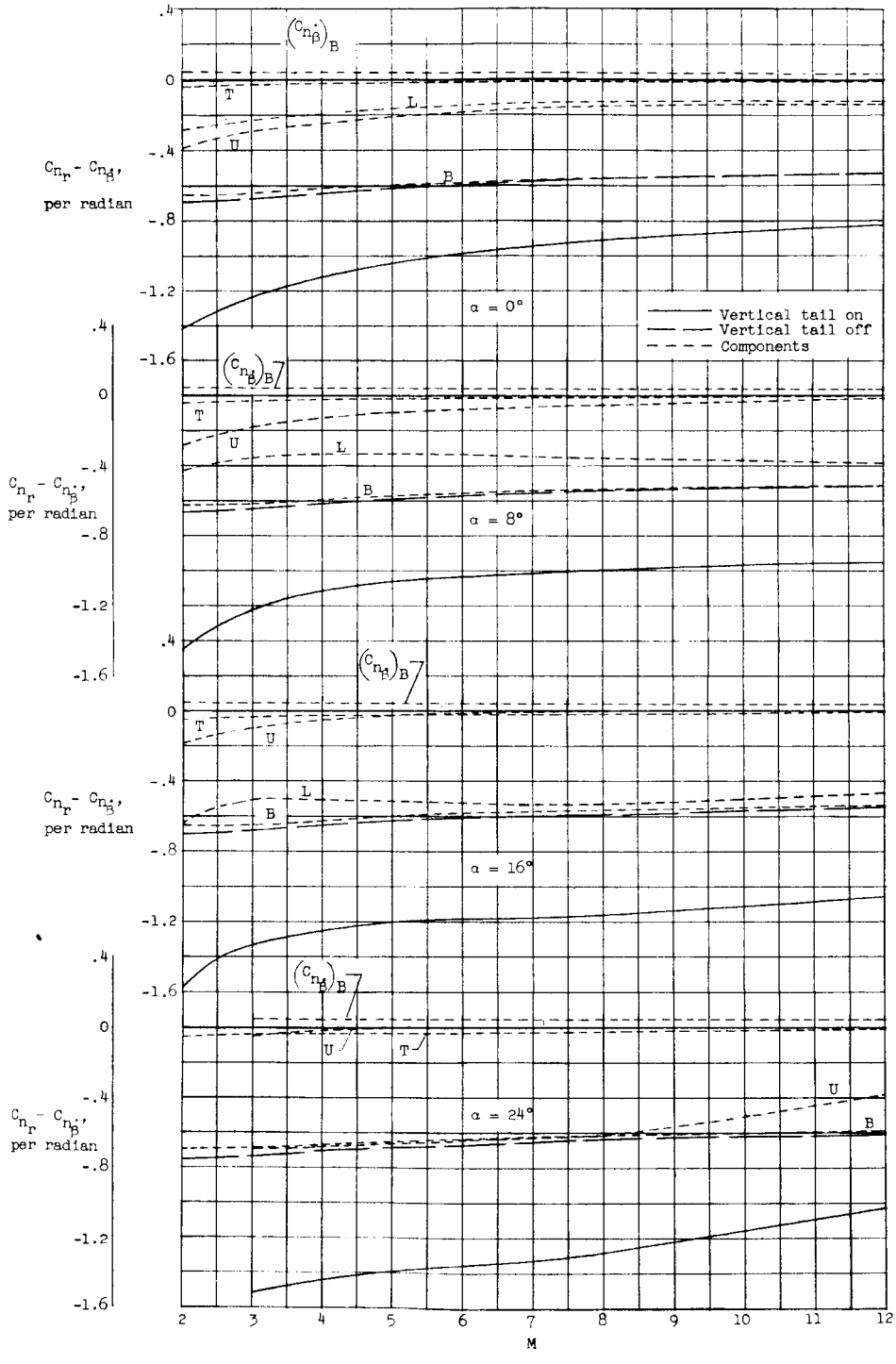

Figure 35.- Buildup of the calculated damping-in-yaw derivative for the X-15 airplane at angles of attack of 0°, 8°, 16°, and 24°. $i_T = 0°$.

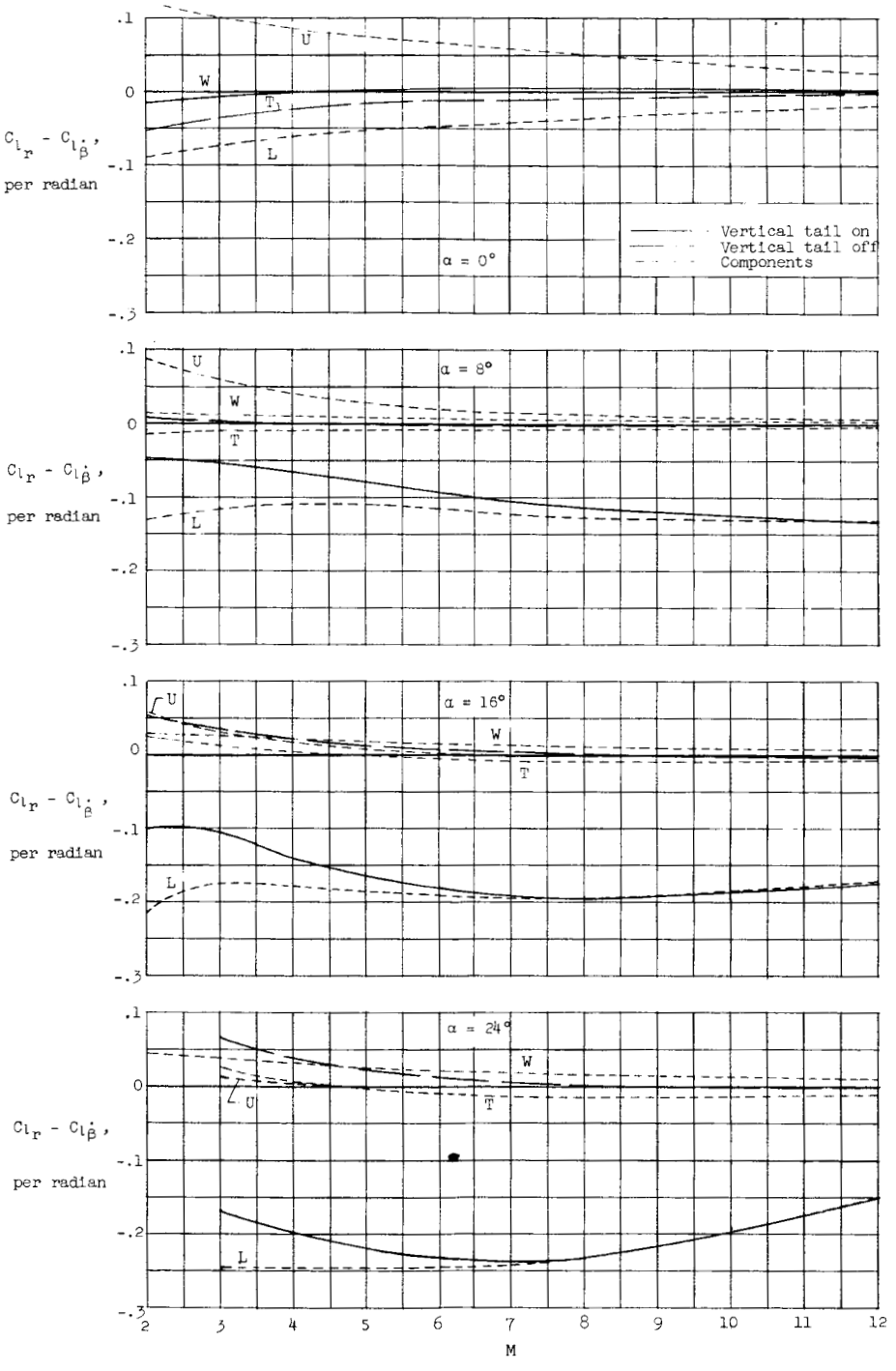

Figure 36.- Buildup of the calculated rolling-moment derivative due to yawing rate for the X-15 airplane. $i_T = 0^o$.

[redacted]

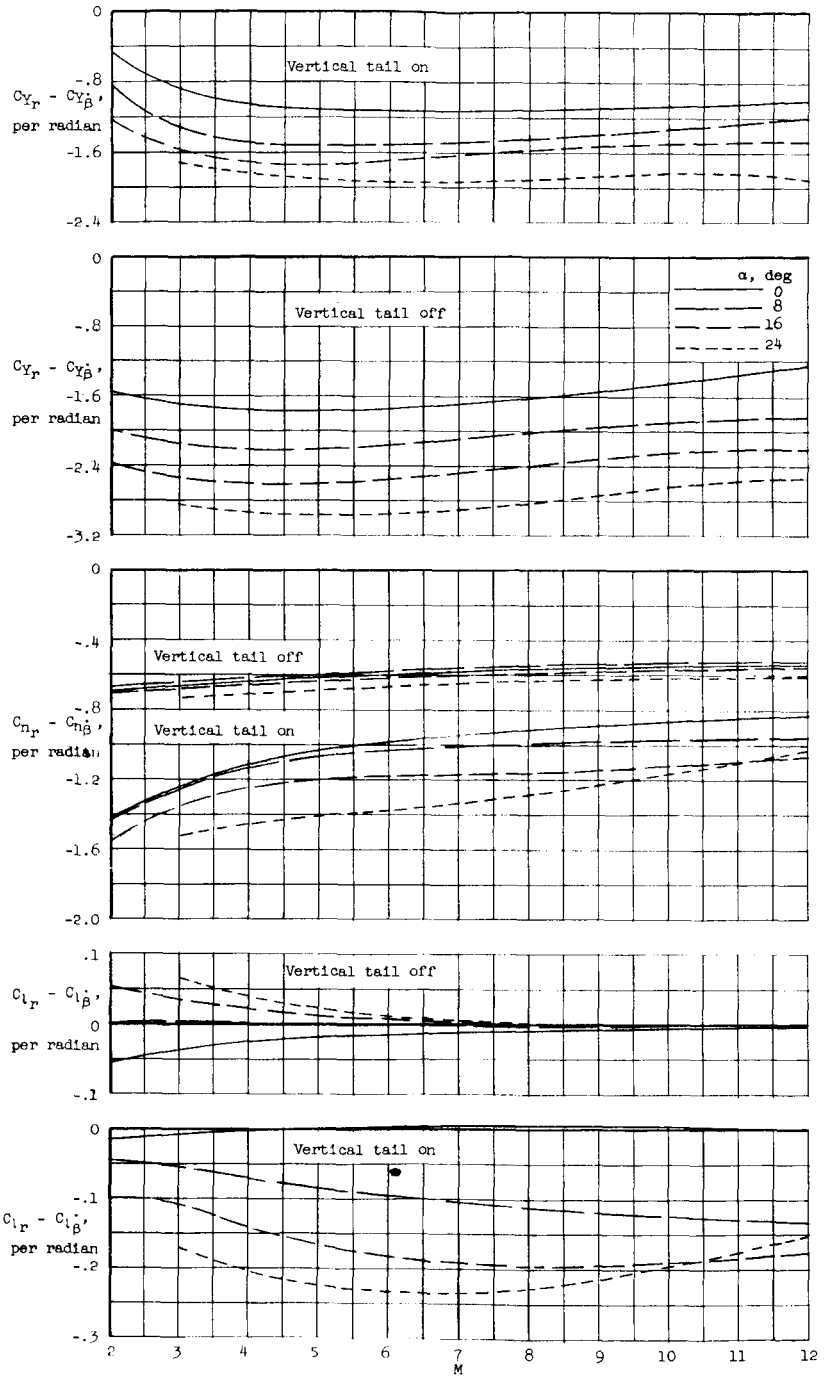

Figure 37.- Summary of the calculated derivatives due to yawing rate for the X-15 airplane with vertical tail on and off at angles of attack of 0°, 8°, 16°, and 24°. $i_T = 0°$.

[redacted]

DECLASSIFIED

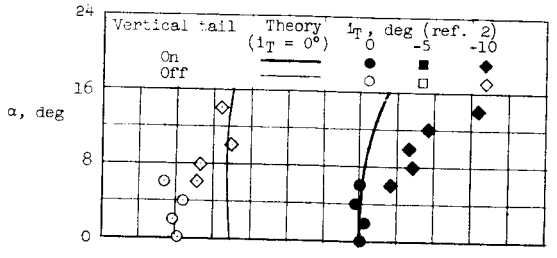

(a) M = 2.0.

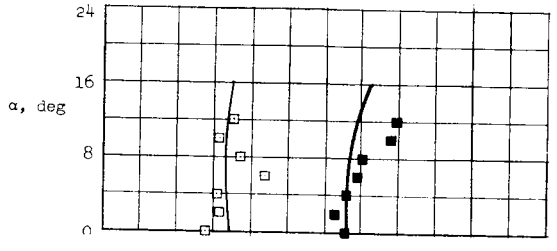

(b) M = 2.5.

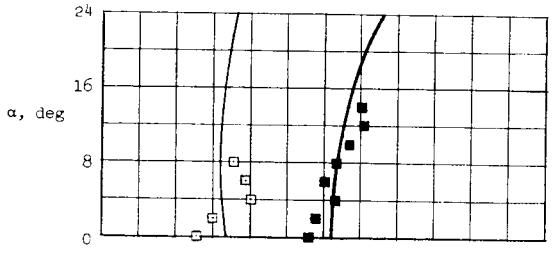

(c) M = 3.0.

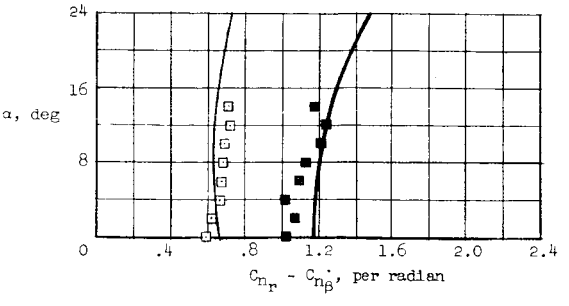

(d) M = 3.5.

Figure 38.- Comparison of the calculated and experimental damping-in-yaw derivative for the X-15 airplane with vertical tail on and off.

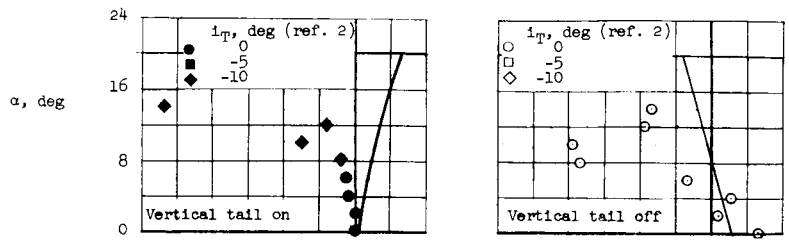

(a) M = 2.0.

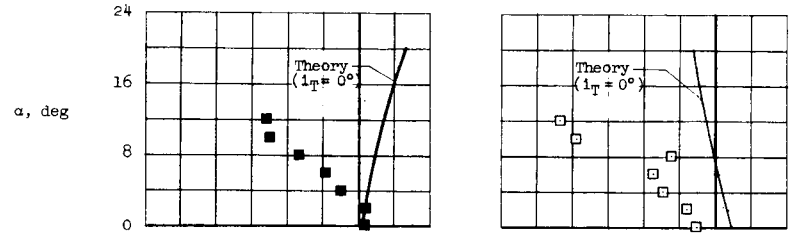

(b) M = 2.5.

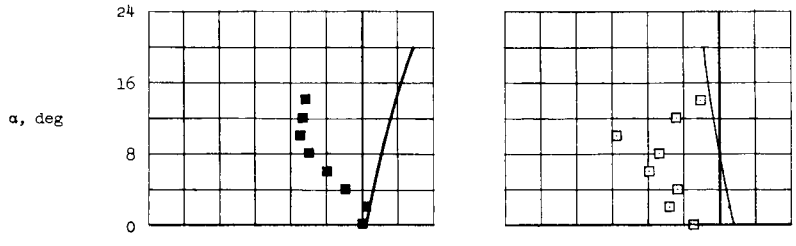

(c) M = 3.0.

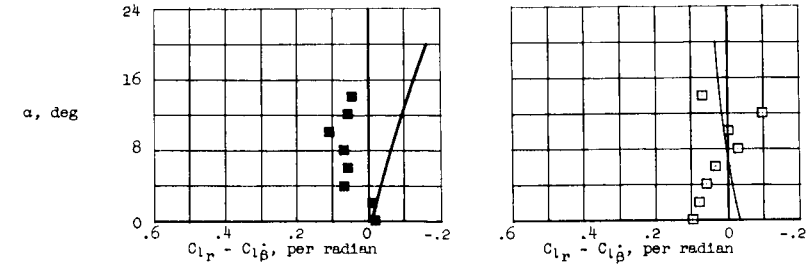

(d) M = 3.5.

Figure 39.- Comparison of calculated and experimental rolling-moment derivative due to yawing rate for the X-15 airplane with vertical tail on and off.

[redacted]SIFIED

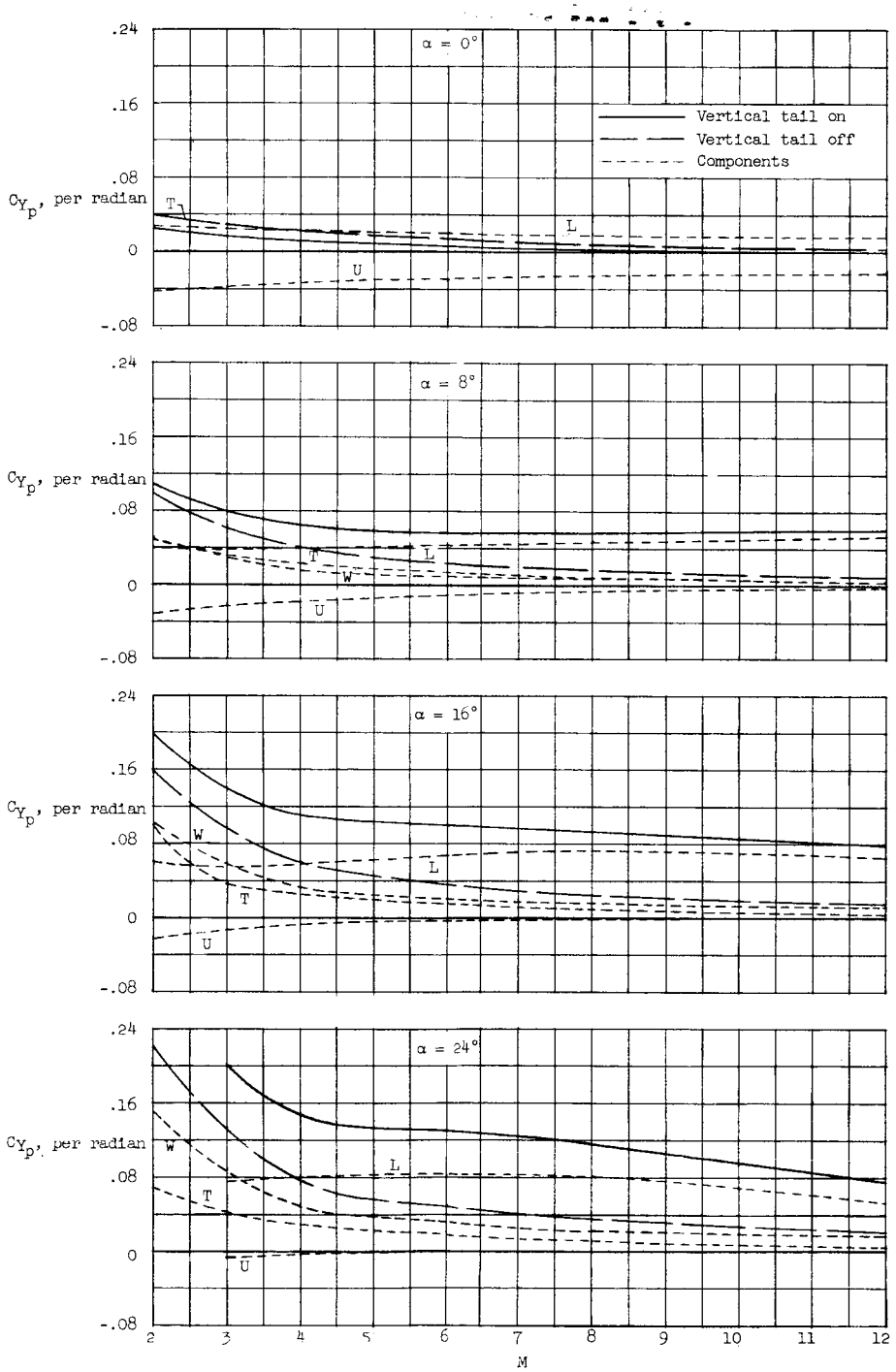

Figure 40.- Buildup of the calculated side-force derivative due to roll rate for the X-15 airplane at angles of attack of 0°, 8°, 16°, and 24°. $i_T = 0°$.

[redacted]

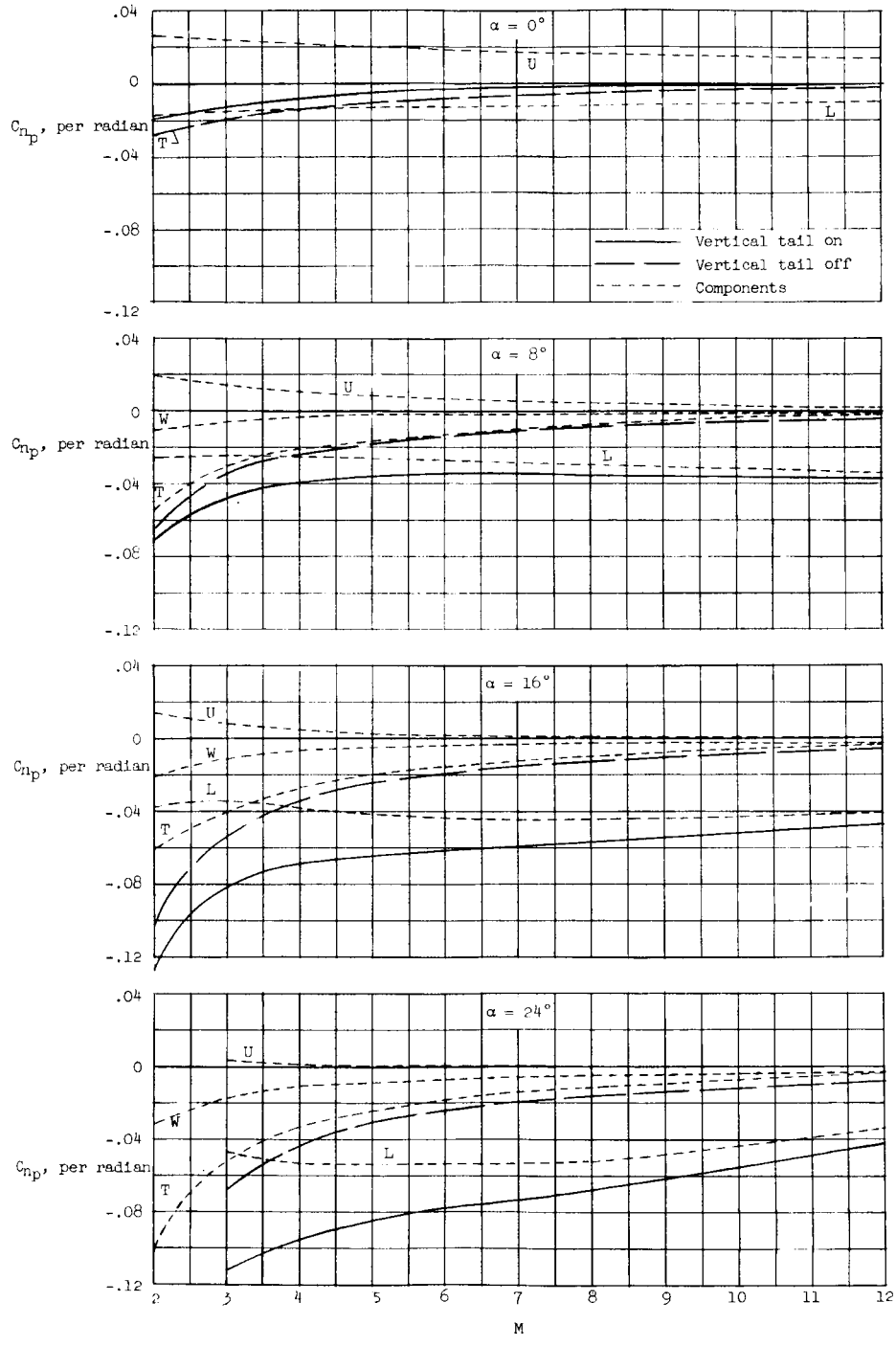

Figure 41.- Buildup of the calculated yawing-moment derivative due to roll rate of the X-15 airplane. $i_T = 0°$.

DECLASSIFIED

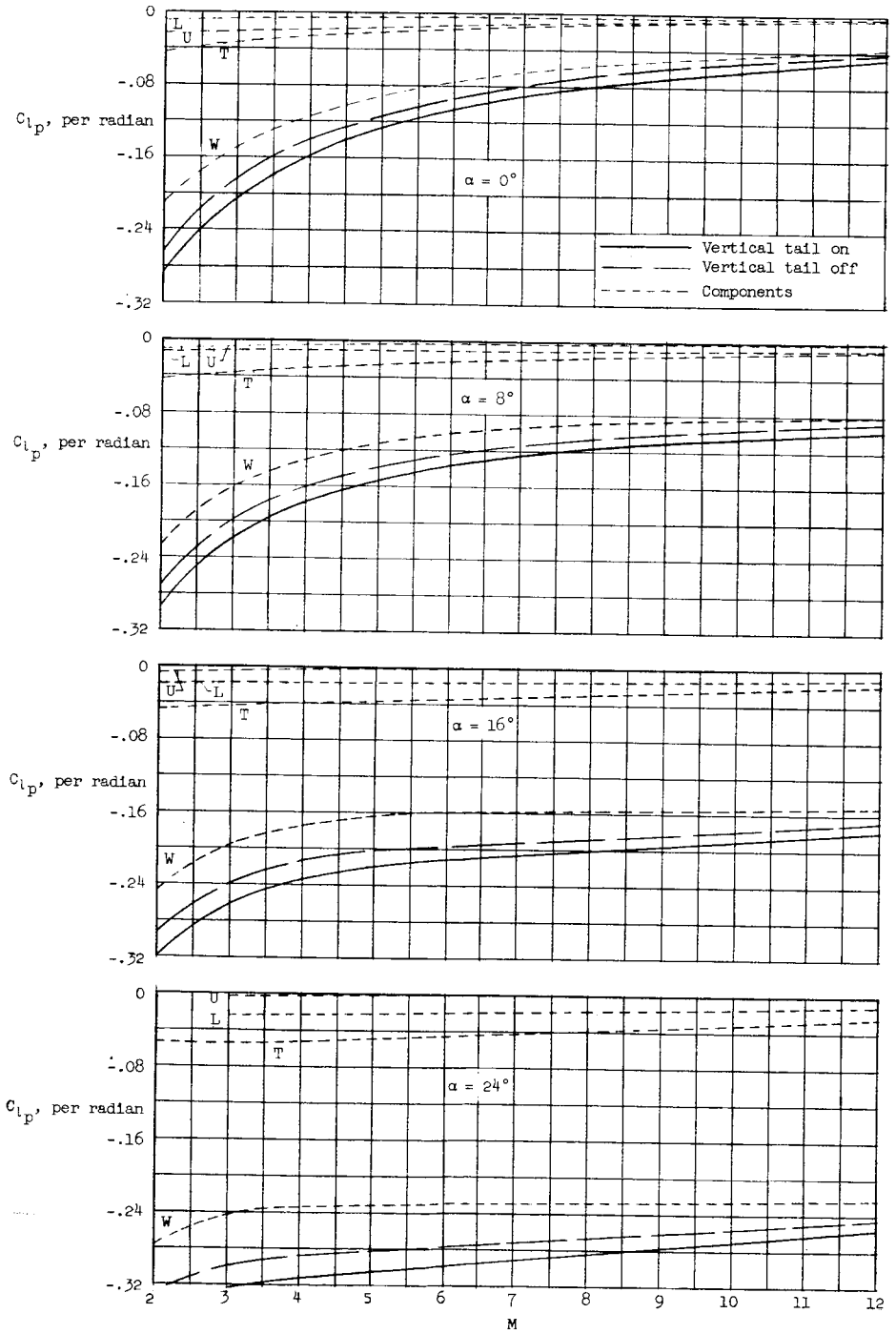

Figure 42.- Buildup of calculated damping-in-roll derivative of airplane at angles of attack of 0°, 8°, 16°, and 24°. $i_T = 0°$.

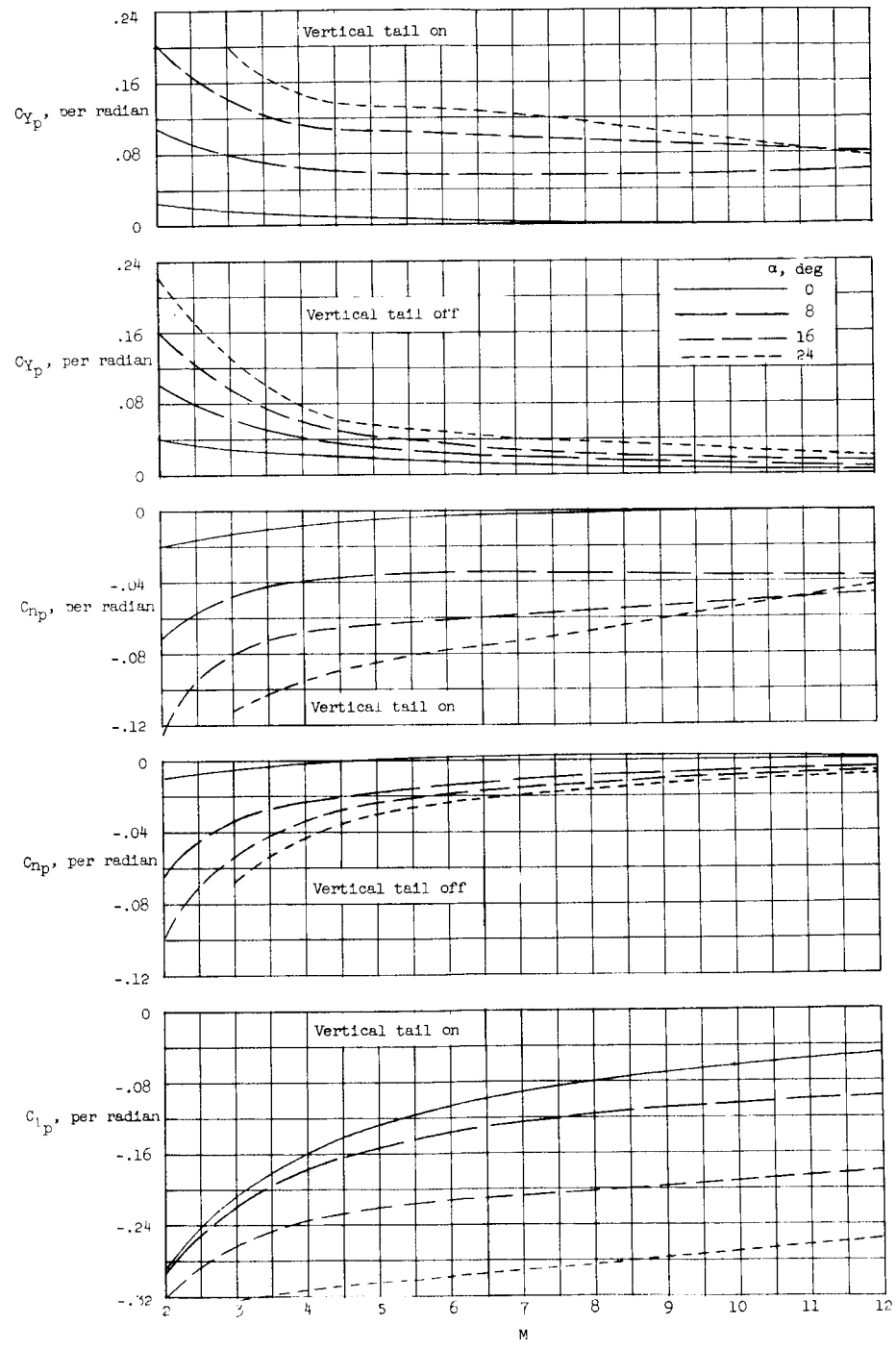

Figure 43.- Summary of the calculated derivatives due to roll rate for the X-15 airplane with vertical tail on and off at angles of attack of 0°, 8°, 16°, and 24°. $i_T = 0°$.

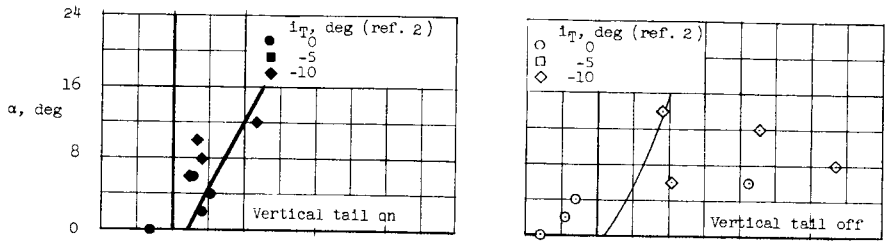

(a) M = 2.0.

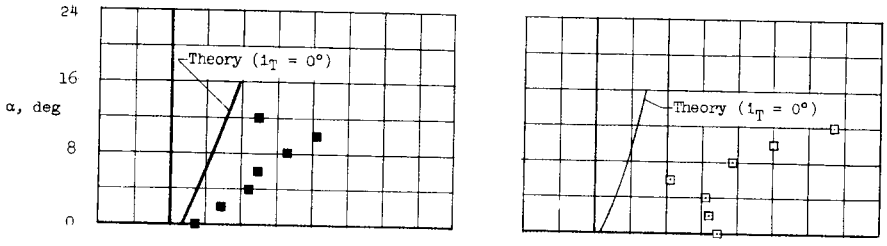

(b) M = 2.5.

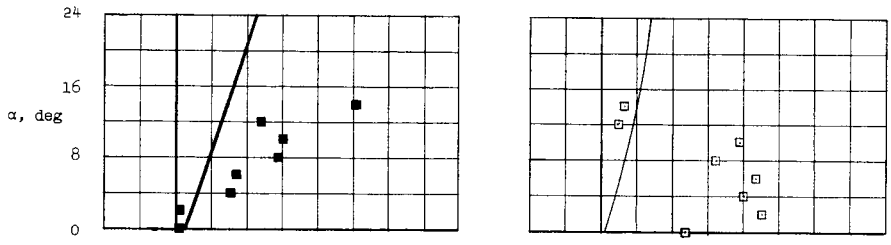

(c) M = 3.0.

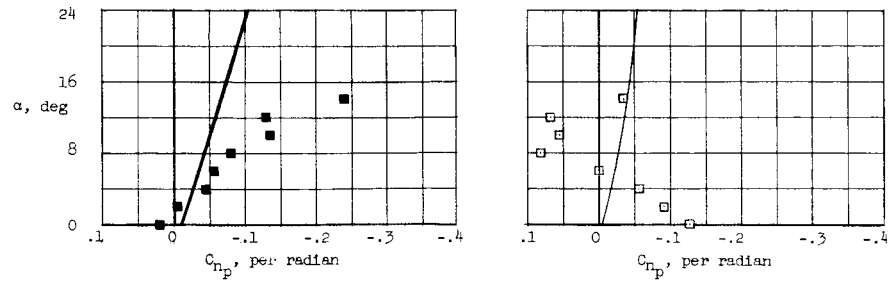

(d) M = 3.5.

Figure 44.- Comparison of the calculated and experimental yawing-moment derivative due to roll rate for the X-15 airplane with vertical tail on and off at several Mach numbers.

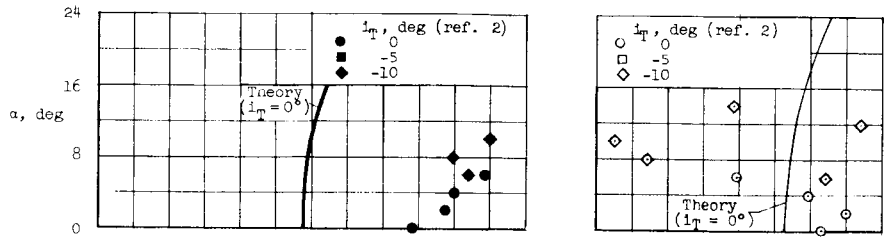

(a) M = 2.0.

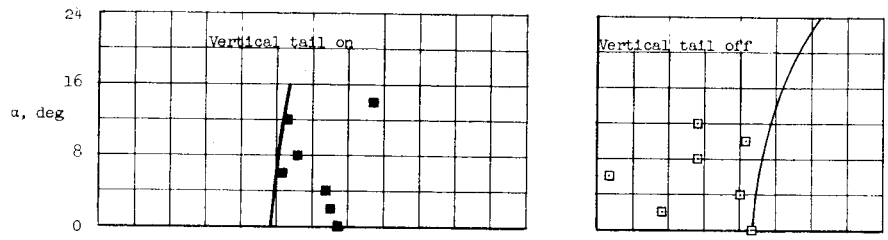

(b) M = 2.5.

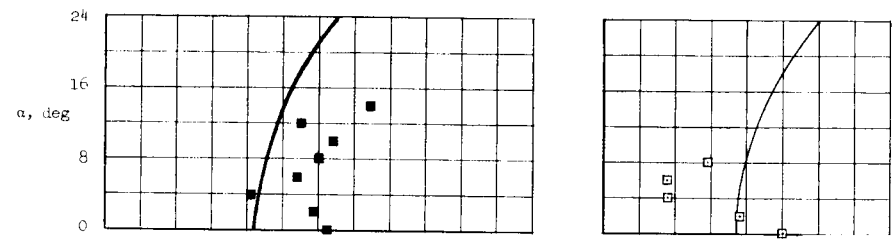

(c) M = 3.0.

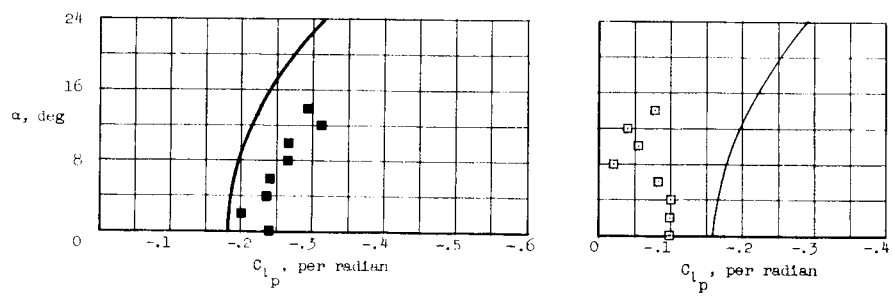

(d) M = 3.5.

Figure 45.- Comparison of the calculated and experimental damping-in-roll derivative for the X-15 airplane with vertical tail on and off at several Mach numbers.

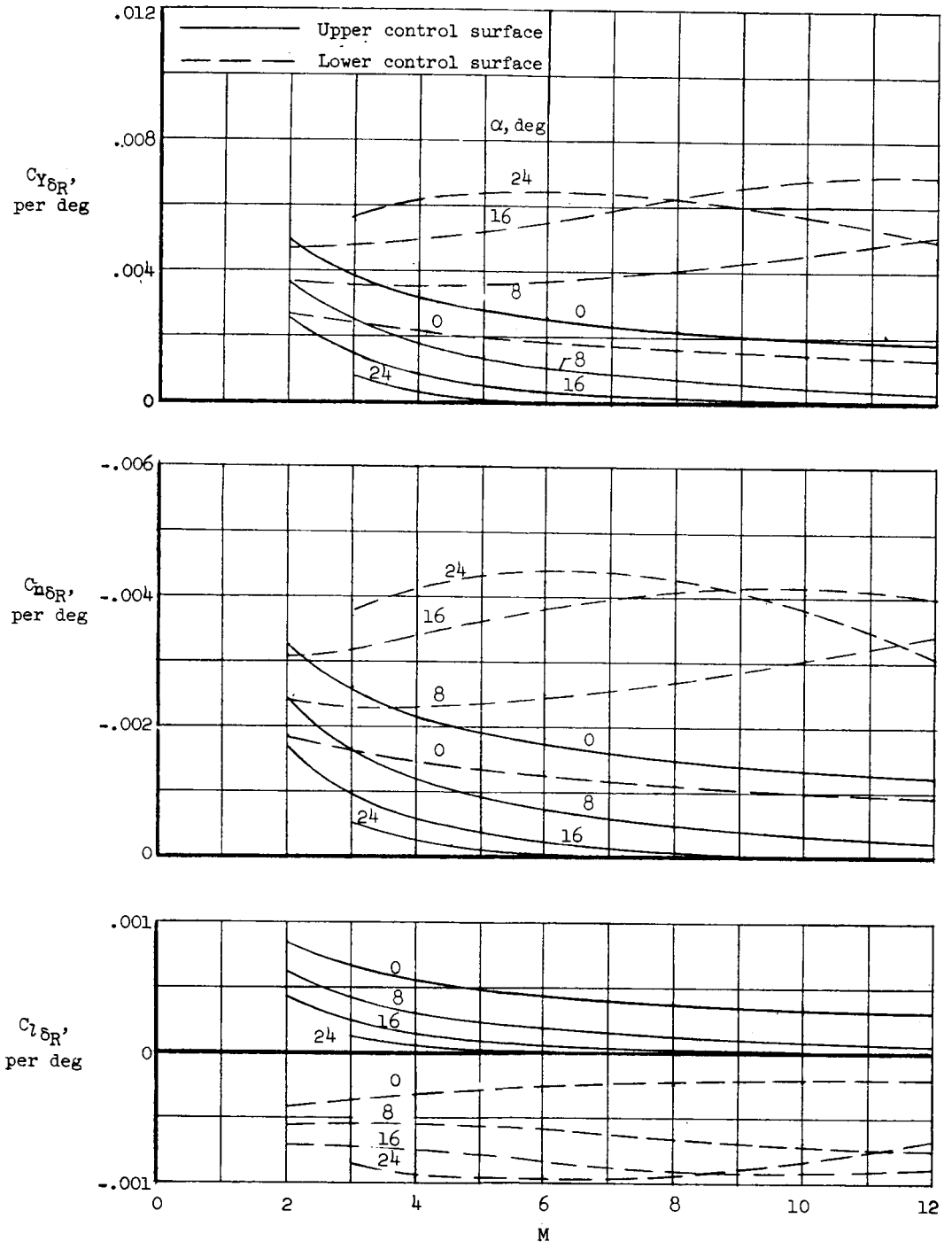

Figure 46.- Calculated side-force, yawing-moment, and rolling-moment derivatives for upper and lower directional-control surfaces of the X-15 airplane.

H-146

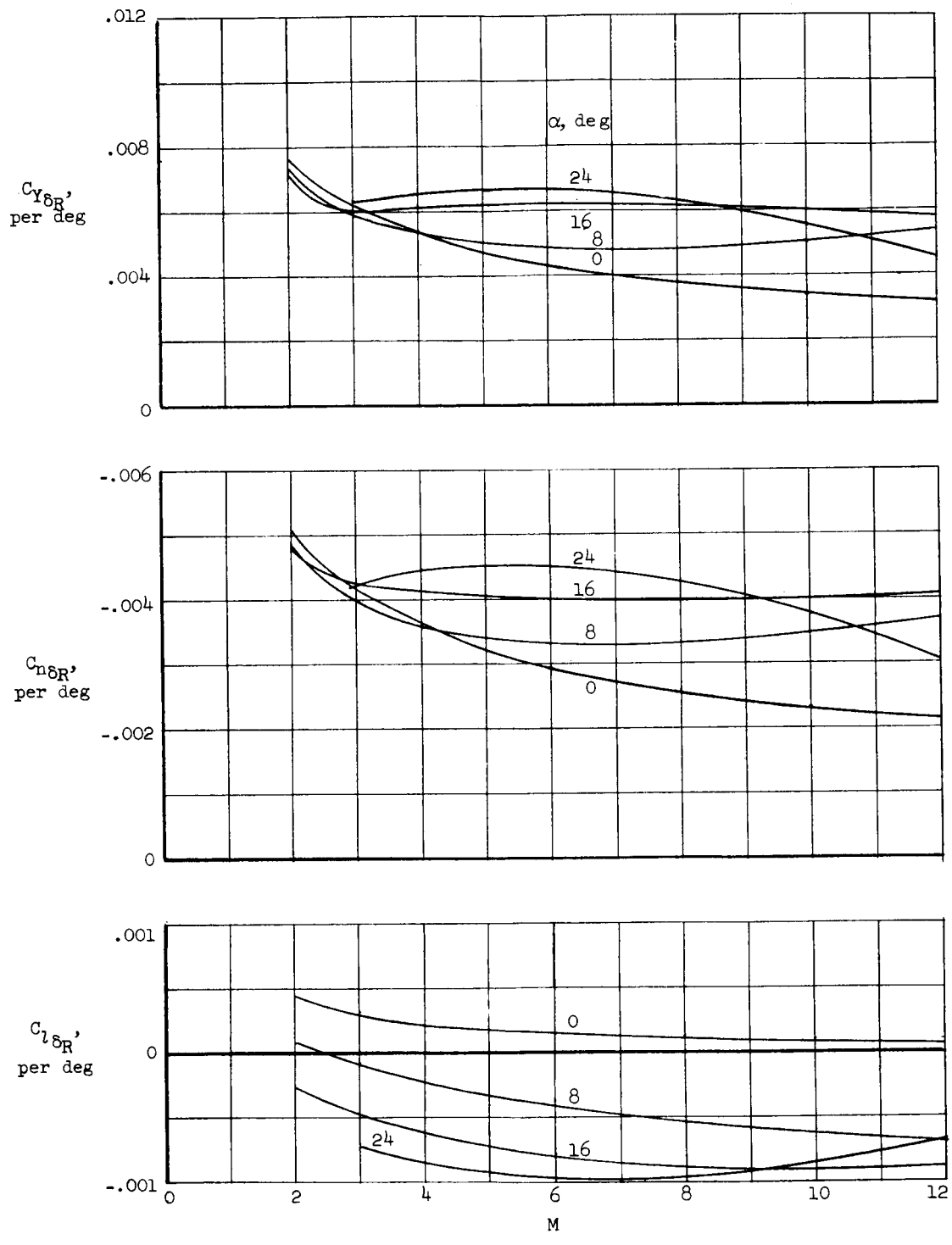

Figure 47.- Calculated directional-control derivatives for the X-15 airplane.

[redacted]

H-146

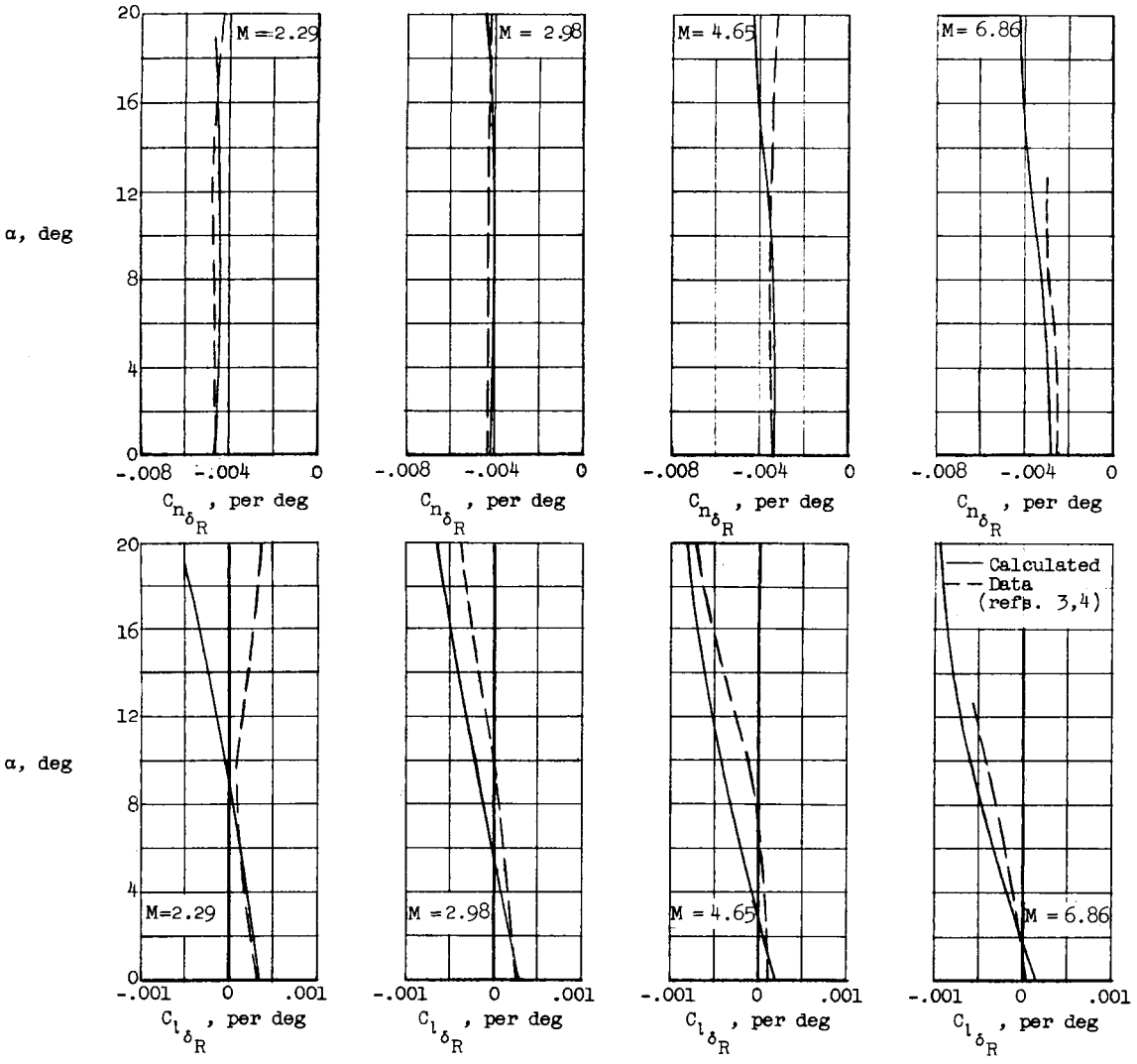

Figure 48.- Comparison of the calculated and experimental directional-control derivatives for the X-15 airplane at several Mach numbers.

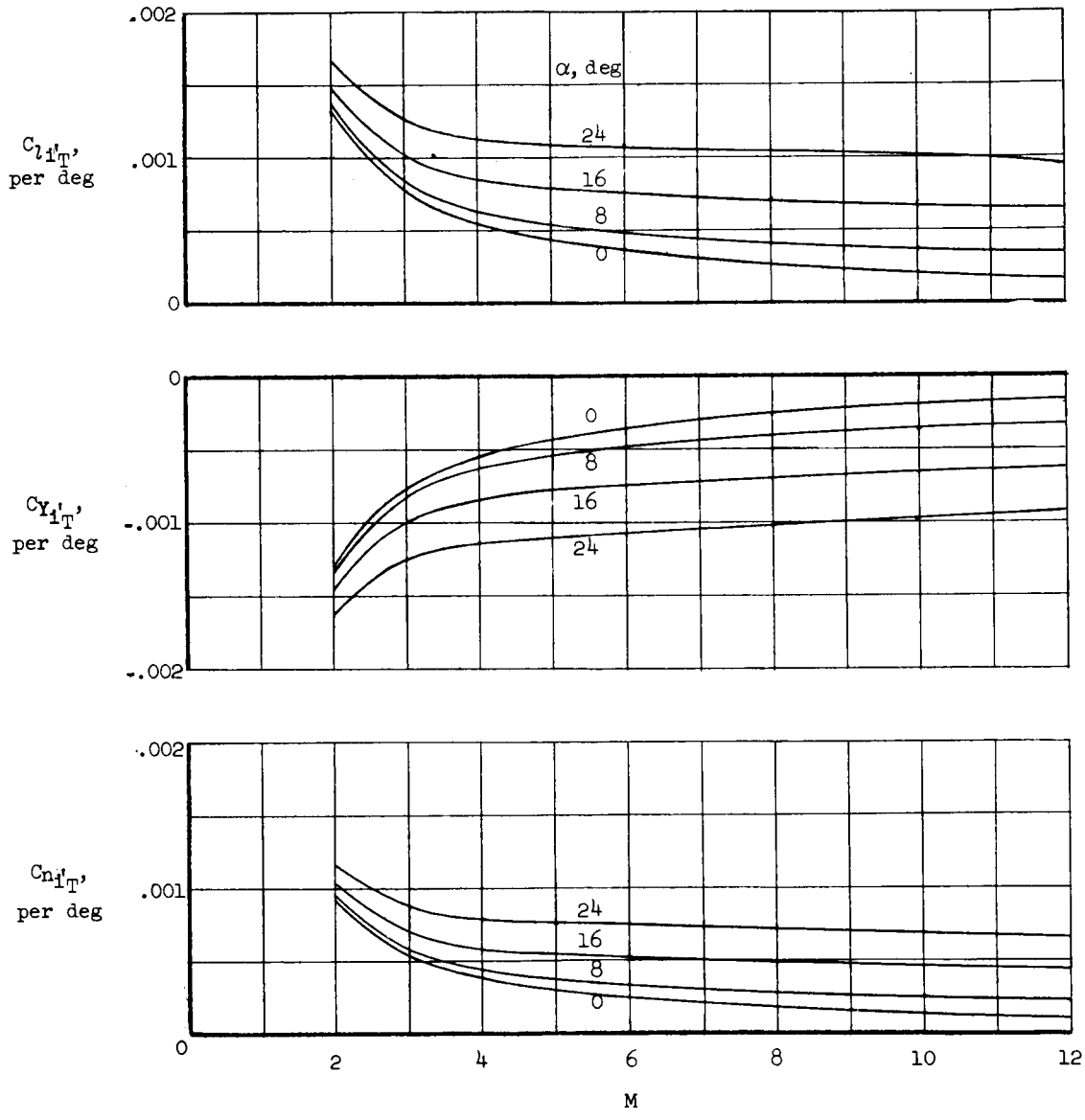

Figure 49.- Calculated lateral-control derivatives for the X-15 airplane.

H-146

NASA - Langley Field, Va.

H-146

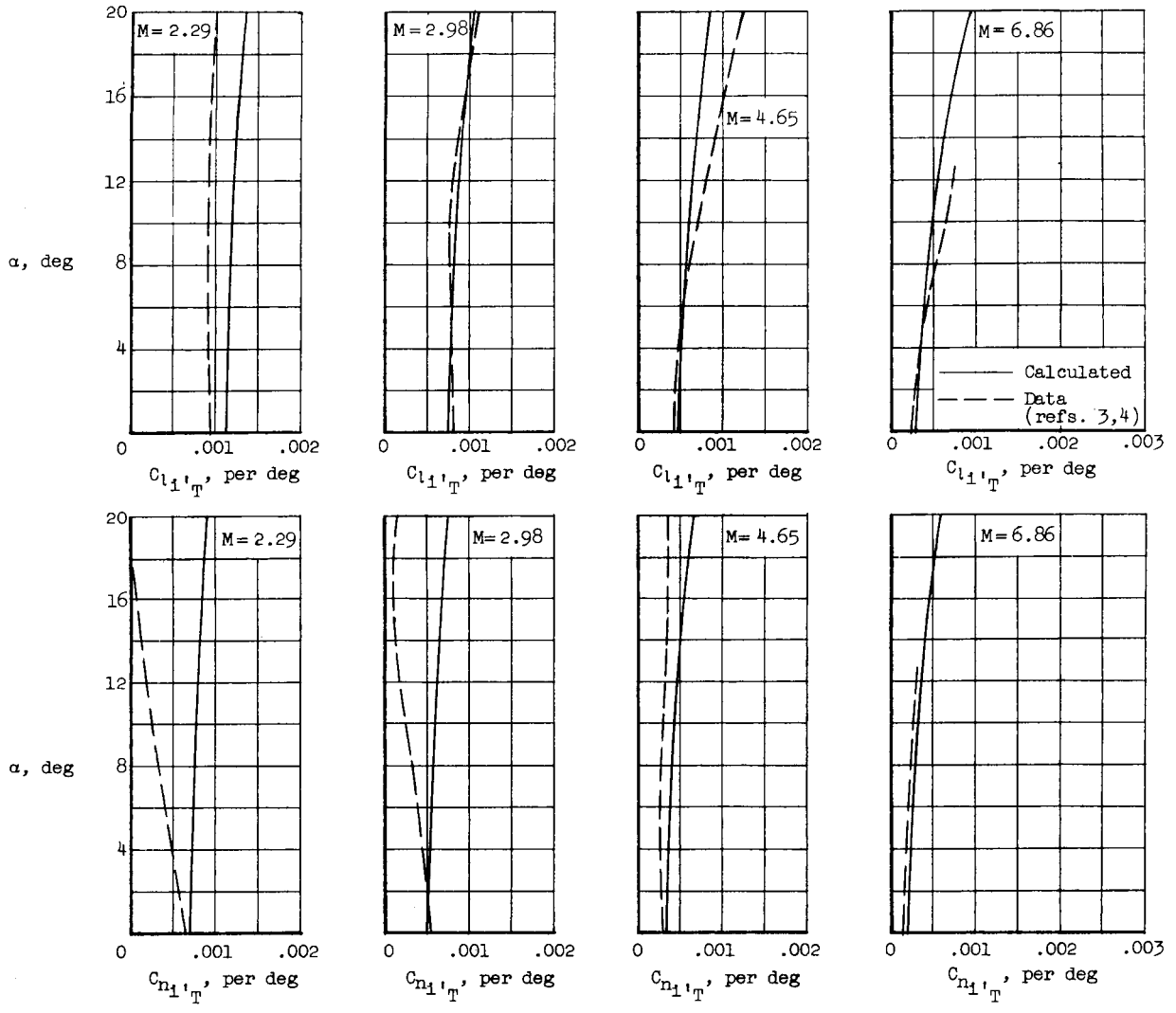

Figure 50.- Comparison of the calculated and experimental lateral-control derivatives for the X-15 airplane at several Mach numbers.